DISSERTATIONES
CHIMICAE
UNIVERSITATIS
TARTUENSIS
189

ESTER TEE

Analysis and development of selective synthesis methods of hierarchical micro- and mesoporous carbons

DISSERTATIONES CHIMICAE UNIVERSITATIS TARTUENSIS
189

DISSERTATIONES CHIMICAE UNIVERSITATIS TARTUENSIS
189

ESTER TEE

Analysis and development of selective synthesis methods of hierarchical micro- and mesoporous carbons

UNIVERSITY OF TARTU
Press

Institute of Chemistry, Faculty of Science and Technology, University of Tartu, Estonia

The dissertation is accepted for the commencement of the degree of Doctor of Philosophy in Chemistry on June 11th, 2019 by the Council of Institute of Chemistry, University of Tartu.

Supervisors:	Prof. Enn Lust University of Tartu, Estonia
	PhD Thomas Thomberg University of Tartu, Estonia
	PhD Indrek Tallo University of Tartu, Estonia
Opponent:	PhD Olivier Crosnier University of Nantes, France
Commencement:	August 30th, 2019 at 12:15 Ravila 14a–1020, Tartu

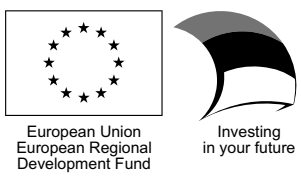

ISSN 1406-0299
ISBN 978-9949-03-112-2 (print)
ISBN 978-9949-03-113-9 (pdf)

University of Tartu Press
www.tyk.ee

TABLE OF CONTENTS

1. LIST OF ORIGINAL PUBLICATIONS

I **E. Tee**, I. Tallo, H. Kurig, T. Thomberg, A. Jänes, E. Lust, Huge enhancement of energy storage capacity and power density of supercapacitors based on the carbon dioxide activated microporous SiC-CDC, Electrochimica Acta 161 (2015) 364–370.

II **E. Tee**, I. Tallo, T. Thomberg, A. Jänes, E. Lust, Supercapacitors Based on Activated Silicon Carbide-Derived Carbon Materials and Ionic Liquid, J. Electrochem. Soc. 163 (7) (2016) A1317–A1325.

III E. Lust, K. Liivand, I. Vaas, T. Thomberg, I. Tallo, H. Kurig, T. Romann, R. Kanarbik, T. Tooming, **E. Tee**, A. Jänes, Separators, electrodes, half-cells and cells of electrical energy storage device, US 14/986, 451 (2017).

IV **E. Tee**, I. Tallo, T. Thomberg, A. Jänes, E. Lust, Steam and Carbon Dioxide Co-Activated Silicon Carbide-Derived Carbons for High Power Density Electrical Double Layer Capacitors, J. Electrochem. Soc. 165 (10) (2018) A2357–A2364.

V **E. Tee**, I. Tallo, T. Thomberg, A. Jänes, E. Lust, Electrical Double Layer Capacitor Characteristics Based on Steam and CO2-Steam Co-Activated Carbon Electrodes and Ionic Liquid Electrolyte, J. Electrochem. Soc. 166 (8) (2019) A1558–A1567.

Author's contribution:

Paper I: Performed all the material synthesis and electrochemical measurements. Collaborated in experimental data interpretation and participated in manuscript preparation.

Paper II: Performed all the electrochemical measurements and analysis of data. Participated in the preparation of the manuscript.

Paper III: The author's share of the patent is 8 %.

Paper IV: Performed all the material synthesis, electrochemical measurements and analysis of data. Responsible for the preparation of manuscript.

Paper V: Performed all the measurements and analysis of data. Responsible for the preparation of manuscript.

2. ABBREVIATIONS AND SYMBOLS

A	cross-section area
ac	alternating current
AN	acetonitrile
BET	Brunauer-Emmett-Teller
C	capacitance
C_{cc}	capacitance calculated from constant current data
C_m	specific gravimetric capacitance
$C_{m;CV}$	gravimetric capacitance calculated from cyclic voltammetry data
C_p	parallel capacitance
C_s	series capacitance
$C'(\lambda)$	wavelength-dependent constant
$C'(\omega)$	real part of complex capacitance
$C''(\omega)$	imaginary part of complex capacitance
CDC	carbide-derived carbon
CC	constant current
CC/CD	constant current charge/discharge
CV	cyclic voltammetry
d	distance
D-R	Dubinin-Radushkevich
E	energy
EDLC	electrical double layer capacitor
EDS/EDX	energy-dispersive X-ray spectroscopy
EELS	electron energy loss spectroscopy
EIS	electrochemical impedance spectroscopy
$EMImBF_4$	1-ethyl-3-methylimidazolium tetrafluoroborate
F-R	Ferrari-Robertson
f	*ac* frequency
f_R	characteristic relaxation frequency
f(W)	pore size distribution
FWHM	full width at half maximum
HRTEM	high-resolution transmission electron microscopy
HS	heterogeneous surface
I	current
I_0	amplitude of current signal
I_D	intensity of the D-peak
I_G	intensity of the G-peak
IUPAC	International Union of Pure and Applied Chemistry
j	current density
L_a	crystallite diameter
L_c	crystallite height
m	mass

$N(p/p_0)$	point in NLDFT adsorption isotherm
$N(p/p_0,W)$	point in NLDFT adsorption isotherm corresponding to the pore with width W
NLDFT	Non-local density functional theory
P	power
p	pressure
p/p_0	relative pressure
PTFE	polytetrafluoroethylene
q	charge
R	resistance of the system
r_p	average pore size
RTIL	room-temperature ionic liquid
S	specific surface area
S_{micro}	micropore surface area
SAIEUS	Solution of Adsorption Integrated Equation Using Splines
SC	supercapacitor
t	time
T	temperature
$TEABF_4$	tetraethylammonium tetrafluoroborate
TEM	transmission electron microscopy
$TEMABF_4$	triethylmethylammonium tetrafluoroborate
TK	Tuinstra and Koenig
V_{ads}	volume of adsorbed gas
V_m	molar volume of adsorbate
V_{micro}	micropore volume
V_{tot}	total pore volume
U	cell potential
U_0	amplitude of potential
w	extent of reaction
W	mass of adsorbed gas
W_m	mass of gas in monolayer
XRD	X-ray diffraction
$Z(\omega)$	impedance
$Z'(\omega)$	real part of impedance
$Z''(\omega)$	imaginary part of impedance
$\|Z(\omega)\|$	impedance modulus
β	full width at half maximum
ε	dielectric constant of the enivronment
ε_0	dielectric permeability of vacuum
λ	wavelength,
ν	potential scan rate
τ_R	characteristic relaxation time constant
φ	phase angle
χ	activation burn off (loss of mass)
ω	angular frequency

3. INTRODUCTION

Activated carbons are widely used materials for various applications due to which their global consumption is increasing every year. This also gives a boost to the relevant scientific research [1–4]. The production methods of activated carbons can be divided into two types, chemical or gas phase (also called physical) activation, but the gas phase activation has become somewhat more favorable. Different biomasses, sugar, carbides, polymers, etc. can be used as precursors.

Most common applications of porous carbons include for example water purification by adsorption and/or filtration, catalyst support and electrode materials in energy storage devices. The structure and porosity characteristics of the activated carbon materials are especially important in terms of suitability for the respective application [1–13].

The interest in supercapacitors is still increasing due to their various applications from portable electronic devices to electric vehicles and also because of their long cycle life, high electrical (energetic) efficiency and high power rates [1, 7, 10–24]. Porous carbons are the most studied electrode materials for supercapacitors. Different activated carbons are used because of their high surface area, low cost and excellent chemical stability [3, 7, 10]. The precursor material, synthesis and activation parameters and conditions have a strong influence on the resulting materials physical properties. This in turn effects the materials suitability for being used as an electrode material in supercapacitors with different electrolyte. Therefore, the influence of production parameters and conditions on the resulting materials properties has to be thoroughly studied and controlled to prepare materials with the exactly right properties for the corresponding application [3, 10, 13–15].

The aim on this study was to analyze and optimize the synthesis steps of activated carbons prepared from silicon carbide. Silicon carbide has been chosen due to its very cheap price compared to other carbides and also to the preferable properties of the carbide derived carbons. Therefore, this work includes the analysis of the influence of the different synthesis and activation parameters on the obtained materials structural and porosity characteristics, which strongly influence the electrochemical properties. The main objective was to evaluate the suitability of the resulting materials as high power density electrode materials for supercapacitors. Physical characterization of the materials was performed using low temperature nitrogen sorption analysis, X-ray diffraction method, Raman spectroscopy and transmission electron microscopy. For the investigation of electrochemical properties cyclic voltammetry, impedance spectroscopy, constant current and constant power discharge methods were used.

4. LITERATURE OVERVIEW

4.1. High surface area carbon materials and their applications

High surface area carbons are materials, which due to their porosity can have a very high surface area (more than 2000 m^2 g^{-1}). The production of commercial carbon is mostly based on cheap biomass, for example different tree barks, fruit shells, wood, charcoal, peat and various carbohydrates (sugar, starch, etc.) have been used [1–9, 25]. In addition to biomass also some synthetic polymers, oil and gas industry wastes are used. The availability, price and critical amount of inorganic impurities are important factors for the choice of the raw material for carbon synthesis [26].

Most porous carbons are produced by pyrolysis from organic materials [1, 27, 28]. The carbonization of the raw material takes place at a high temperature in an inert gas atmosphere, whereby the organic compound decomposes and non-volatile carbon remains [2]. Usually some pre-treatment of the raw materials is required before pyrolysis. The material must be crushed and sieved to obtain the required particle size. Sometimes it is necessary to treat the raw material with water or acid to remove impurities and reduce the content of mineral substances [26]. In case of closed pores activation process is used to open them and also increase the surface area of the material [1, 27, 28].

In addition to organic materials, porous carbons can also be produced from various carbides. These carbons are called carbide-derived carbons (CDC). The main advantages of CDCs over carbons synthesized from organic materials are greater purity, narrower pore size distribution and better conductivity [3, 10, 11, 14, 27, 29–31].

Due to their variable microstructure, high electrical conductivity and various forms (powders, fibers, foams, etc.) [32, 33] porous carbons have a number of potential applications, such as the storage of hydrogen and methane including the separation of certain gases from mixtures. The use of porous carbon materials as a catalyst support, filter material in water and air filters, sorbent for chromatography or as an electrode material in Li-ion batteries and supercapacitors are also common. Depending on the application, mainly micro-, meso- or macroporous carbon is required [1-3, 10, 26–28, 30, 31, 33–37].

4.1.1. Supercapacitors

Supercapacitors (SC) are energy storage devices consisting of two electrodes impregnated with an electrolyte and separated by an ion-permeable separator. In terms of energy and power density, they fill the gap between batteries and conventional dielectric capacitors [13, 23, 26, 29, 34, 38–43, 47]. SCs have many advantages over batteries: fast charging and discharging, long lifetime (up to one million charging cycles), high efficiency. Compared to batteries SCs have a

very high power density (~ 10 kW kg^{-1} vs. battery ~1 kW kg^{-1}), but their energy density is significantly lower (~ 10 kW kg^{-1} vs. battery ~100 kW kg^{-1}). Although SCs have similarities to batteries, their charge storage mechanisms are different [14, 15, 17, 18, 21, 26, 32, 34, 38, 42, 44–47].

Based on the energy storage mechanism the supercapacitors are classified into two types: electrical double layer capacitor (EDLC) and pseudocapacitive (Faradaic) capacitor (pseudocapacitor) [15, 40–43]. In the EDLC energy is stored by the accumulation of charge within the electrical double layer at the electrode|electrolyte interface. When charging, the cations move to the negatively and anions to the positively charged electrode. It is a reversible process based on purely electrostatic interactions and therefore allows very fast energy storage and release (up to a few seconds to minutes). Only the electrolyte-accessible surface contributes to the charge storage, so optimizing the pore size, pore structure and surface properties of the electrode material is extremely important [32, 33, 39, 40, 48–50].

In a pseudocapacitive capacitor the energy storage takes place in addition to the electrical double layer also by redox reactions. The main difference between the EDLC capacitance and pseudocapacitor capacitance lies in faradaic origin of the last – reversible redox reactions occur at the electrode|electrolyte interface, where one of them can be origin of pseudocapacitance. Due to the increased Faradaic capacitance the pseudocapacitors have a somewhat higher energy density than EDLCs. Conversely, their power density is lower because of the slower Faradaic reactions [38, 39, 45, 48, 49].

In addition to the pseudocapacitor and EDLC, there are also hybrid capacitors, in which one electrode behaves according to the electrical double layer or pseudocapacitive mechanism and the other electrode is a battery-type electrode that stores energy through Faradaic processes. With this design it is possible to take advantage of both electrode materials, hence increase the potential range, but also energy and power densities. Although the different energy storage mechanisms in the hybrid capacitor take place at the same time, mostly one of them is more dominant [39, 40, 49–51].

Most important parameters to compare in different SC applications are the capacitance, energy and power densities. The capacitance C of one electrode can be found by the following equation:

$$C = \frac{\varepsilon \varepsilon_0 A}{d}, \tag{1}$$

where ε is the dielectric constant of the environment, ε_0 the dielectric permeability of vacuum, A the area of the boundary and d is the distance between the plates. The capacitance of a two-electrode SC is equal to the sum of the capacitances of two capacitors connected in series:

$$\frac{1}{C}=\frac{1}{C_1}+\frac{1}{C_2}, \tag{2}$$

where C is the capacitance of the cell, C_1 and C_2 are the capacitances of the positive and negative electrode, respectively.

The stored energy E is represented by the equation:

$$E=\frac{1}{2}CU^2, \tag{3}$$

where C is the capacitance and U the cell potential of the two electrode cell. The maximum power P also depends on the cell potential U applied and can be found according to the equation:

$$P=\frac{U^2}{4R}, \tag{4}$$

where R is the internal resistance of the system. The dependency of energy density and power density is presented as a graph called Ragone plot [3, 33, 43, 46, 52, 53].

The main contribution to the systems internal resistance comes from: the resistance of the electrode material, contact resistance between particles, the resistance between the electrode and current collector, the resistance of the electrolyte, the resistance of the mass transport of ions to the micropores of the carbon material and porous separator [19, 20]. The high internal resistance limits the capacitor capacitance, power density and ultimately its applicability [38, 41–43, 46].

The performance of an EDLC depends mainly on two factors. The choice of electrode material has a significant effect on capacitance and the electrolyte used primarily determines the cells potential range [13, 16–18, 21, 34, 42, 43, 46].

For EDLCs mostly carbon materials are used as electrode material, whereas for pseudo-capacitive capacitors conductive polymers, transition metal oxides/ hydroxides or carbons modified with heteroatoms (e.g. oxygen or nitrogen) are used. Several different types of carbons can be used for EDLC electrodes, including high specific surface area activated carbons, carbon aerogels, carbon nanotubes, activated carbon fibers, graphene etc. The capacitance of the electrode depends to a large extent on the material used, particularly its specific surface area, pore size distribution, electrical conductivity and surface wettability [12, 15]. Theoretically the increase in specific surface area should also increase capacitance, but in reality the dependence between them is not linear, but logarithmic [3]. The ideal electrode material must include micropores, which

are important for the adsorption of ions, as well as mesopores, which are necessary for the rapid transport of ions within the material [3].

The capacitance of the carbon electrodes can be significantly increased by modifying the surface with heteroatoms (e.g. O, N, S, P, B), which generate additional pseudo-capacitance on the surface of the carbon and improve surface wettability, but noticeably reduce the lifetime of the system. The main advantages of carbon materials are: availability, fairly cheap price, good electrical conductivity, high surface area, easy processing, chemical stability in various solutions and thermal stability over a wide range of temperatures [26, 32–34, 38–41, 43, 44, 46–49, 53].

In commercial EDLCs mostly used electrode materials are activated carbons produced from organic raw materials, characterized by irregular and wide pore size distribution. They are supplemented with an electrically conductive compound, mostly a more graphitic carbon material with better conductivity, e.g. carbon black is added into electrode matrix. Advantages of conductive polymers with capacitive behavior due to rapid Faradaic processes are low cost, good conductivity in doped state and high porosity. The main problem is long-term stability as they degrade quickly by cycling. In case of transition metal oxides or hydroxides electrodes the energy density is higher than that of carbon materials, but nevertheless they are so far not used in commercial SCs as they have: 1) lower conductivity, which increases the resistance and decreases the power density; 2) lower electrochemical stability while cycling; 3) complex optimization of surface area, pore size distribution and porosity is needed; 4) high cost [26, 32, 34, 38–41, 43, 44, 46–49, 53].

Choosing the SC electrolyte two main factors have to be considered: the electrochemical stability, which determines the applicable potential range, thus the energy and power densities (Eqs. 3 and 4), and the conductivity, which also has a significant effect on the power density (Eq. 4). The electrolytes in SCs are divided into three groups: 1) electrolytes based on aqueous solutions; 2) electrolytes based on organic solvents (acetonitrile, propylene carbonate, etc.); 3) ionic liquids and mixtures of ionic liquids. The advantages of aqueous solutions (e.g. H_2SO_4, KOH, Li_2SO_4, Na_2SO_4) over other electrolytes are higher capacitance and conductivity and lower cost, but their main drawback is the very limited applicable potential range (up to ~ 1 V). Most common organic solvents used are propylene carbonate and acetonitrile in which quaternary ammonium salts are dissolved (e.g. tetraethylammonium tetrafluoroborate, $TEABF_4$). These electrolytes can operate at higher potentials (generally up to ~ 2.7 V, but in very clean conditions even up to 3.2 V) [10, 13, 14, 17] and therefore allow higher energy and power densities (Eqs. 3 and 4). Compared to aqueous solutions they provide lower capacitances and electrical conductivity. Ionic liquids are salts in liquid phase at room temperature, due to which solvents are not required. Therefore the vapor pressure of such electrolyte is very low, which increases safety and reduces harmful effects on the environment. SCs operating with ionic liquid electrolyte allow for higher potential range (up to ~ 3.7 V) and good cyclability, but due to their high viscosity and lower

conductivity their resistance at room temperature is significantly higher than for other organic and H_2O based electrolytes [13, 22–24, 38, 41, 43–46, 52, 53].

A very important role in achieving high power in SCs has also the choice of separator [19, 20]. The separator used must be electrochemically stable, highly porous, thermally and chemically inert and wet well with the electrolyte used. The separator is not an active material in the SC, so it must be as thin as possible to reduce the internal resistance of the system. However, the thickness must be sufficient to maintain the mechanical strength of the separator and to avoid direct electrical contact between the electrodes. For example, cellulose and glass fibers can be used, but different synthetic polymers are more common [19, 20, 42, 48].

SCs are suitable for applications that require powerful energy pulses in a short time. They allow to reduce the size of the main energy source and increase the efficiency of the system. SCs are added to various electronic devices as a backup power source, for example in cameras, computers and mobile phones. Due to fast charging and discharging, long lifetime and high electrical efficiency (over 95%), SCs are also suitable for the recovery of so-called kinetic energy, i.e. in applications, where kinetic energy is converted into electrical energy. In this way, SCs are used in means of transport, where energy is stored during braking and released during acceleration. A similar method can be found for cranes and elevators. Additionally, SCs can be used as an alternative source of energy, when during daytime solar panels generate energy and at night the necessary energy comes from the fully charged SCs. Fast charging and discharging also allows them to be used in military and aerospace industries, because batteries are too slow for some applications and dielectric capacitors are too large and low in energy [13, 23–38].

In hybrid energy systems, SCs are combined with batteries or fuel cells to improve the systems energy density, lifetime and efficiency. In addition to high energy and power densities, SCs have some significant advantages in employing them – they are safe, maintenance-free, long lifetime, working at lower temperatures and wider working temperature range, no moving parts in the system and generally do not need a cooling system [23–38].

4.1.2. Electrical double layer theory

There are several theories about the electrical double layer structure, first of which was created by Helmholtz in 1853. The term “double layer” derives from Helmholtz model, which represents the electrode|electrolyte boundary as two parallel charged layers, which are of opposite signs and whose distance is equal to the diameter of the solvent molecule. Based on this theory, an electrical double layer can be observed as a conventional flat capacitor, which capacitance C can be found as follows:

$$C = \frac{\varepsilon\varepsilon_0}{d}, \tag{5}$$

where ε is the dielectric constant of the environment, ε_0 the dielectric permeability of vacuum and d is the distance between the plates.

Although the Helmholtz model is fairly in accordance with experimental data, this model has several drawbacks as it does not take into account the capacitance dependence on the electrolyte concentration, electrode potential, system temperature, etc [38, 42, 45–48, 54].

At the same time Gouy and Chapman independently of each other developed the next electrical double layer model, which also takes into account the applicable electrode potential, electrolyte concentration and the effect of ions heat motion on the system capacitance. In this model it was assumed that the ions are point charges, which distribution is subordinated to the Boltzmann equation. Based on the Gouy-Chapman theory, the electrode does not form a compact layer such as Helmholtz described, because the ions are in constant heat motion. Therefore, in the Gouy-Chapman model a double layer is called a diffuse layer. This theory is consistent with experimental results only for solutions with a very low concentration, because the dimensions of the ions are not taken into account [42, 45, 46, 48, 54].

Stern combined Helmholtz and Gouy-Chapman models, taking into account the true size of the ions and the possibility of specific adsorption. This model combines both Helmholtz's compact layer and Gouy-Chapman theory's diffuse layer formed by the ions heat motion. The total capacitance of the system can be found from the capacitance of capacitors connected in series. The Stern model provides a much better prediction of electrode capacitance than previous theories [38, 42, 45, 46, 48, 54].

The Stern model was greatly enhanced by Grahame, eliminating several drawbacks of previous models. He pointed out that the electrostatic and specific adsorption of ions are of a different nature. In the first case, the effective forces are weak, ions do not deform during adsorption, they continue to participate in the heat motion and their closest distance from the electrode is equal to the so-called outer Helmholtz layer distance. In the second case, stronger chemical forces occur, ions deform, the solvate layer decomposes and ions lose their mobility. These specifically adsorbed ions form the inner Helmholtz layer. Thus, based on this theory there are three layers: 1) inner Helmholtz layer located at a distance, which plane passes through the centers of specifically adsorbed ions (ions are not fully solvated); 2) outer Helmholtz layer, which passes through the centers of solvated and non-specifically adsorbed ions (ions drawn toward the electrode with the coulombic forces); 3) diffuse layer, formed of ions in heat motion outside the outer Helmholtz layer. The inner and outer Helmholtz layer form a compact layer. The total charge of the compact and diffuse layer completely compensates the electrode charge [45, 48, 54, 55].

In addition to these four most well-known electrical double layer theories, many more sophisticated models were developed, such as the Bockris, Devanathan and Müller models [38, 42, 43].

The final capacitance of the electrical double layer is influenced by a number of parameters: electrode material, electrode area, accessibility to electrode surface, electric field strength through the electrode and electrolyte/solvent properties [38].

4.2. Carbide-derived carbon (CDC)

Carbide-derived carbons are synthesized from carbides using different methods [10, 11, 18, 34–36]. The structure of CDCs can be both disordered or highly ordered. This depends mainly on the synthesis method and the initial carbide used, whereby generally the original shape and size of the particles in maintained. Thus, by varying the processing conditions, it is possible to obtain materials with different surface area and pore size distributions [3, 10, 11, 34–36].

In this study the widespread "initial carbide-CDC" terminology is used, as it clearly indicates which carbide has been used. Other variants of the literature may be found, wherein the carbon synthesized from SiC is SiC-CDC, SiC-DC, Si-CDC or SiCDC. The latter two do not reflect the various stoichiometric coefficients of the initial carbide are not applicable to carbons synthesized from carbonitrides and other complex compounds, and therefore are not recommended [35].

4.2.1. CDC synthesis methods

There are three main methods to synthesize carbon materials from carbides: halogenation, hydrothermal method and thermal decomposition.

Halogenation, in particular chlorination, has become one of the most applied methods for producing CDC [10, 11, 35]. Carbon material is formed by selective removal of metal atoms from the crystal structure of the carbide, resulting in a carbon skeleton [10, 11, 35, 56–58].

Chlorination of SiC was initially used to produce silicon tetrachloride ($SiCl_4$). When gaseous chlorine and SiC react, $SiCl_4$ and carbon are formed and this reaction is described in simplified terms by:

$$SiC_{(s)} + 2\ Cl_{2(g)} \rightarrow SiCl_{4(g)} + C_{(s)}. \quad (6)$$

Carbon was considered an unwanted by-product and only later the great value of porous CDC was recognized. A variety of binary and ternary carbides can be used for CDC synthesis: Al_4C_3, BaC_2, CaC_2, Cr_3C_2, Fe_3C, Mo_2C, Nb_2C, SiC, ZrC, Ta_2C, TaC, Ti_2AlC, Ti_3AlC_2, TiC, Ti_3SiC_2, VC, W_2C, WC, etc [3, 10, 11, 34–36, 58].

During chlorination the initial shape and size of carbide particles are maintained in the CDC formation process [10, 34–36, 57, 58]. In some cases there is a partial collapse of the carbon structure due to very high porosity and lattice parameters of the initial carbide [35]. The structure, pore size distribution and specific surface area of the CDC depends on the initial carbide and the halogenation temperature [31, 34–36, 57, 58]. As the temperature increases, the disordered amorphous carbon gradually becomes more ordered and graphitic. In CDCs some other structures can also be found: bulbous structures, nanotubes, fullerene-like structures, etc [35, 36, 57].

Reaction products left in the pores, such as metal chlorides, can be removed by post-synthesis treatment, the most common of which are treatment with argon, hydrogen or nitrogen at high temperature. Compared to argon, hydrogen is more effective for removing chlorine because it is capable to react with chlorine to form hydrochloride (HCl) that can be easily removed from the pores due to the smaller molecule diameter. The final properties of the resulting carbon also depend on the post-treatment process parameters in addition to the initial carbide and the synthesis temperature [3, 35].

In addition to chlorination, CDCs can be produced by hydrothermal degradation. This method is based on the decomposition of carbides in supercritical water under the influence of high pressure and temperature. In addition to carbon, metal oxides (MO_x), methane (CH_4), carbon monoxide (CO) and hydrogen (H_2) [34–36, 59] are formed during the process. Synthesis is mainly affected by the temperature, pressure and mass ratio of water:carbide [34–36]. With the hydrothermal method it is possible to obtain both amorphous, graphitic and variable structure carbons [35].

SiC and several other carbides decompose at high temperatures. Such thermal decomposition under vacuum or in an inert gas environment results in carbon formation and evaporation of the carbide-forming metal [34–36]. In case of SiC, the process proceeds following: silicon from the outer layer of the carbide evaporates and the microporous layer of carbon remains, the silicon diffuses from the inner layer to the outer surface and evaporates. The movement of silicon atoms from the inner layers to the outer surface also contributes to some extent to the reorganization of carbon atoms, i.e. porous structure development [34]. Structural reorganization is more easily carried out at higher temperatures, since then the mobility of the carbon atoms is higher. For synthesis of carbon by thermal decomposition, the minimum temperature is considered to be 800 °C, where a reduced pressure is also required. Due to SiC anisotropy, various carbon nanostructures [35] can be obtained, such as nanotubes, graphite like, turbostratic and onion-like carbon particles [34–36].

4.3. Activated carbons

During the synthesis, closed pores can be retained within the porous carbon, for which activation is used to open them and also expand the surface area.

Activation processes are often in literature divided into two groups: gas phase and chemical activation [1–3, 5]. Gas phase activation methods are based on high temperature treatment of carbon materials with different gases. In case of chemical activation, the initial carbon material is mixed with a solid or liquid chemical (i.e. reagent) and heated [1, 2, 60]. There are two phases of activated carbon production: carbon synthesis of initial carbide material and activation of the resulting product [1, 3, 46]. The properties of the resulting carbon material largely depend on the activation process. Even small changes in reaction parameters (temperature, time) can significantly alter the pore structure, surface chemistry and morphology [37, 60, 62].

The applications of activated carbons are significantly affected by chemical composition of the surface. Depending on the activation method, different functional groups are formed on the surface of the carbon materials, most common of which are oxygen-containing functional groups. Molecular oxygen can dissociate into atoms that chemically react with carbon to form surface compounds. In addition to oxygen compounds, further nitrogen or hydrogen compounds with carbon can be found. Surface functional groups have a significant effect on how different adsorbates interact with carbon electrodes [3, 9, 26, 62].

4.3.1. Gas phase activation

During gas phase activation, the carbon material is usually oxidized with H_2O-steam, oxygen or carbon dioxide [1, 2, 13, 26, 37, 62–64]. Selective removal of carbon atoms occurs: the oxidizing gas reacts with carbon atoms, which results in formation of CO and increased porosity of the material [2, 3, 56, 63].

Gas phase activation is simple, inexpensive, environmentally friendly and unlike chemical activation, where metal ions can remain in the carbon material, it does not produce impurities in the material [1, 5, 9, 37, 44]. The speed of activation increases with increasing temperature. If the activation is too extensive, the carbon structure will collapse and the specific surface area will begin to decrease again [5].

CO_2 is a fairly moderate oxidant compared to O_2 and allows better control over the microporous structure during activation [37, 64]. Activation with O_2 requires lower temperatures compared to CO_2 or water vapor activation due to increased reactivity, due to which the process is more difficult to control. For both O_2 and CO_2 activations, the micropore volume is usually the highest at short activation times and decreases with time. Initially, micropores are formed, which over time expand into mesopores. The low activation temperature is favorable for micropores formation. At higher temperatures and shorter activation times, the volume of mesopores generated is higher and micropores formation is unfavorable. The increase of porosity can take place in two steps: 1) formation of new micropores, 2) expansion of existing pores into larger pores over longer periods of activation, increasing the total pore volume [37, 44, 56, 64].

CO_2 and steam are the most widespread activating agents due to the endothermic nature of their reactions with carbon, which facilitates process control. In the initial stages of activation, CO_2 favors microporosity formation, whereas steam activation favors microporosity widening, and thus activated carbon prepared by steam activation exhibit a lower micropore volume at the expense of larger meso and macropore volumes. Therefore, both CO_2 and steam can be suitable activating agents, depending on the choice of precursor material and process conditions [1, 9, 47, 64]

4.3.2. Chemical activation

In addition to gas phase activation, chemical activation with different solutions or solids is often used [13, 26]. The initial material is impregnated or mixed with the reagent and then heated. The resulting product should be thoroughly washed to remove reagent residues. The selection of the activation temperature and time depends on the reagent used [26]. The most commonly used reagents for chemical activation are NaOH, KOH, HNO_3, H_2SO_4 and H_3PO_4 [13, 37]. Chemical activation with KOH was introduced at the end of 1970s and the corresponding activated carbons have been available since 1980 [61].

Chemical activation has several advantages over gas phase activation. From the point of view of conducting the activation, lower activation temperature and shorter reaction time is needed. Also higher yields and porosity of material can be achieved. However, significant disadvantages are expensive and corrosive reagents (compared to water vapor and CO_2) and further on, the washing of the resulting product is required, which results in wastewater production [5, 8, 25, 65]. Chemical activation can give a material with larger specific surface area and more uniform pores, but metal ions can stay in the carbon material, which are difficult to remove afterwards [44]. The specific surface area is significantly influenced by the mass ratio of carbon to reagent, activation temperature and to some extent on the activation time [8]. By increasing the activation temperature, mesoporosity, micropore volume and the total pore volume of the resulting material increase. Porosity may increase due to existing pore expansion and formation of new pores [61].

4.4. Characterization methods of carbon materials

4.4.1. Gas sorption

4.4.1.1. Surface area and porosity

Carbon materials with large specific surface area have a complex pore network consisting of pores of different sizes. According to the IUPAC classification, the pores are divided as follows:

- Micropores (nanopores): diameter below 2 nm;

- Mesopores: diameter 2 – 50 nm;
- Macropores: diameter above 50 nm [26, 66, 67].

Micropores may in turn be further divided into supermicropores (0.7 – 2 nm) and ultramicropores (< 0.7 nm). Pores can be both open and closed. Closed pores have no contact with the outside environment, which means that no substances from the surrounding environment can get into the closed pores.

Physical sorption of different gases is used to characterize the pore structure of the carbon material. Low-temperature (T = 77 K) liquid nitrogen sorption is the most commonly used analysis method [26].

4.4.1.2. Adsorption/desorption isotherms

Adsorption isotherm is a dependence between the amount of adsorbed gas (adsorbate) and the partial pressure at a constant temperature [66, 67]. When measuring the isotherm, the partial pressure of the adsorbate is first gradually increased and the gas molecules adsorb onto the adsorbent surface. Subsequently, the partial pressure of the adsorbate is reduced and the gas molecules are desorbed from the material surface. The shape of the resulting isotherm depends on the porosity of the material and on the shape of the pores. According to the IUPAC distribution, there are six different isotherm types according to their shape:

- Type I isotherm is characteristic of microporous materials. At lower relative pressures, the isotherm is convex with respect to the x-axis and at higher relative partial pressures approaches to the limit value. There may also be a hysteresis.
- Type II isotherm is characteristic of macroporous or non-porous materials. In the $p/p_0 > 0.1$ region, the isotherm turns, the amount of gas adsorbed at high relative pressures $p/p_0 > 0.9$ increases sharply. The adsorption and desorption branches coincide and there is no hysteresis. The turning point describes a step in which the adsorbate forms a completely filled monolayer on the adsorbent surface. At higher relative pressures, the adsorbate forms a multilayer.
- Type III isotherm is concave with respect to the x-axis, since the adsorbates own molecular attraction is stronger than the adsorbate-adsorbent interactions. The adsorption and desorption branches coincide and there is no hysteresis. The corresponding isotherm is rare, an example can be water adsorption to porous hydrophobic materials.
- Type IV is characteristic of mesoporous materials that undergo capillary condensation, usually referred to by the presence of hysteresis.
- Type V isotherm occurs with mesoporous materials with low adsorption energy. Hysteresis also occurs due to condensation.
- Type VI isotherms are rare. The corresponding isotherm describes layer-layer adsorption process and occurs on a very homogeneous and/or non-porous surface [2, 66, 67].

If the adsorption and desorption branches of the isotherm do not overlap, there is an area between these branches called the hysteresis loop. The shape of the hysteresis loop provides information on the shape of the pores. According to IUPAC, there are four types of hysteresis loops [26, 66, 67]:

- H1 type hysteresis loops have parallel and almost vertical branches. This type of hysteresis is characterized by cylindrical pores, that are well interrelated and the pore size distribution is very uniform.
- H2 type hysteresis has a triangular shape with a sharp desorption branch. It is characterized by a material with a narrow pore size distribution, predominantly in the form of bottle neck pores.
- H3 type hysteresis is characterized by slit-shaped pores.
- H4 type hysteresis loop has parallel and almost horizontal branches. This type characterizes narrow slits-shaped pores [26, 66, 67].

Quantitative interpretation of isotherms is required to compare different materials. For this purpose, several methods are used, the most common of which are the models of Brunauer-Emmett-Teller (BET), Dubinin-Radushkevich (D-R), Langmuir and non-local density functional theory (NLDFT) [8, 66].

4.4.1.3. Brunauer-Emmett-Teller theory

The Brunauer-Emmett-Teller (BET) theory is one of the most usable methods for calculating the specific surface area of porous materials based on the determination of the monolayer capacity (number of adsorbed molecules in monolayer on the surface of the material). The BET equation is as follows:

$$\frac{1}{W(p/p_0 - 1)} = \frac{1}{W_m C} + \frac{C-1}{W_m C}\frac{p}{p_0}, \tag{7}$$

where W is the mass of the adsorbed gas at relative pressure p/p_0 and W_m is the mass of the adsorbate in the monolayer. C is the constant of the BET equation associated with adsorption energy of the first adsorbed layer [2, 26, 66, 67].

The following assumptions have been made for the BET equation: the surface is smooth, all the adsorption centers have equal energy levels, there are no lateral interactions between the adsorbed molecules, adsorption energy for all molecules is equal to the liquefying energy, except for the first layer molecules and the adsorbate can form infinite number of layers. In case of activated carbons all these assumptions do not apply. For example, the surfaces are geometrically and energetically not homogeneous and there are lateral interactions between the adsorbed molecules. Despite these problems, the BET theory has become the standard approximation for finding the specific surface area of microporous materials [26].

4.4.1.4. Calculation of total pore volume

To find the total pore volume V_{tot}, the relative pressure must be as close as possible to the saturation pressure, since in this case it can be assumed that all pores are filled with liquid adsorbate. The amount of liquid nitrogen adsorbed into the pores can be found by the following equation:

$$V_{tot} = \frac{pV_{ads}V_m}{RT}, \tag{8}$$

where p is the pressure, V_{ads} is the adsorbed volume of nitrogen, V_m is the molar volume of nitrogen, R is the universal gas constant and T is the temperature.

In case of cylindrical pores, the average pore size r_p can be estimated by the total pore volume V_{tot} of the equation:

$$r_p = \frac{2V_{tot}}{S_{BET}}, \tag{9}$$

where S_{BET} is the specific surface area of the material, found on the basis of BET theory [66].

4.4.1.5. The *t*-plot method

The *t*-plot graph depicts the relationship between the volume of adsorbed gas and the statistical thickness of the adsorbed layer. The thickness of the adsorbed layer t at each point in the isotherm can be found by the equation:

$$t = 3{,}54\frac{V_{ads}}{V_m}, \tag{10}$$

where 3.54 is the thickness of the monolayer of nitrogen (Å) and V_{ads}/V_m is the ratio of the adsorbed nitrogen and the monolayer nitrogen volumes at the same relative pressure on the non-porous surface.

There are several different equations for evaluating the thickness of the adsorbed layer, but the most commonly used are Harkins and Jura and Broekhoff-de Boer [66–68]. The work of Harkins and Jura deals primarily with the method of finding the surface area of a solid, where unlike the BET theory the molecular surface σ is not used. They show that the graph:

$$\log\left(\frac{p}{p_0}\right) = B - \frac{A}{V_a^2}, \tag{11}$$

reaches a linear area, where the layer is condensed (A and B are Harkins-Jura isotherm constants). The adsorbed amount is related to the statistical thickness of the adsorbed layer and is described by the de Boer equation [26, 66–68]:

$$t(\text{Å}) = \left[\frac{13{,}99}{\log(\frac{p}{p_0}) + 0{,}034} \right]^{\frac{1}{2}} \tag{12}$$

4.4.1.6. Non-local density functional theory and pore size distribution

The non-local density functional theory (NLDFT) is well suited for micro- and mesopore size analysis, enabling the calculation of the materials pore size distribution from the adsorption isotherm data. The pore size distribution is the pore volume or area distribution according to the pore size. Whenever possible, the adsorption part of the isotherm is used to determine the pore size distribution, since in this case the filling of pores is independent from the size and filling of surrounding pores. This model objectively describes local fluid structure near curved solid surfaces. The shape of the adsorption isotherm is determined by the liquid-liquid and liquid-solid intermolecular interactions. The relationship between molecular forces and the shape of adsorption isotherms can be described by the generalized adsorption isotherm (GAI) equation:

$$N(\frac{p}{p_0}) = \int_{W_{\min}}^{W_{\max}} N(\frac{p}{p_0}, W) f(W) \mathrm{d}W, \tag{13}$$

where $N(p/p_0)$ is a point on the adsorption isotherm, W is the pore width, $N(p/p_0,W)$ is the point with corresponding pore width W and $f(W)$ pore size distribution. This equation assumes that the entire isotherm consists of several individual “single pore” isotherms multiplied by their relative distribution $f(W)$ over the total pore size distribution. The $N(p/p_0,W)$ isotherms are obtained from a DFT method using a computer program and the pore size distribution is used to solve the GAI equation [66, 67].

In this study the SAIEUS (Solution of Adsorption Integrated Equation Using Splines, Micromeritics) program is used to find pore size distribution data, which unlike the classic NLDFT model also takes into account the energetic heterogeneity of the carbon surface [69–71].

4.4.2. X-ray diffraction

X-ray diffraction (XRD) analysis is a widely used method for studying and quantitative analysis of crystalline structures [72].

Diffractograms of carbon materials synthesized from powdered carbides typically have four to five diffraction peaks: 002 (2θ~26°) and 004 (2θ~54°) correspond to parallel-oriented graphite layers and 100/101 (2θ~43°) and 110 (2θ~78°) characterize the size of the graphite layer.

To characterize the structure, the distance between the layers d, crystal height L_c and crystallite diameter L_a are determined. The diameter and height of the crystal can be found using the Scherrer equation:

$$L_{a,c} = \frac{K\lambda}{\beta \cos\theta}, \tag{14}$$

where λ is the wavelength of X-ray beam, β is the width of the corresponding peak at half maximum in radians in the 2θ scale, θ is the position of the peak in radians and K is the constant, which depends on the reflection plane (0.91 and 1.84 respectively for L_c and L_a). The L_a value is calculated using the peak value of 100 and the value of 002 or 004 for L_c. For the characterization of CDC, XRD is also used to determine the approximate proportion of amorphous (without long-range crystalline order) carbon in the material. Degree of graphitization can be found using the equation:

$$G = \frac{\frac{I_{002}}{I_{100}}}{C_{emp}} 100\%, \tag{15}$$

where I_{002} and I_{100} are the integrated intensities of the respective peaks and C_{emp} is the empirical constant [73–75].

4.4.3. Raman spectroscopy

Raman spectroscopy is a standard non-destructive analysis method, which is common to characterize crystalline and amorphous carbon [73, 76–78]. In near-infrared region, the Raman spectra of carbon materials have two peaks called D (disordered) and G (graphitic) peaks. The shape of both peaks depend mainly on the regularity of sp^2 bonds and indirect also of sp^3 bonds. The following data (peak positions) apply in case of Ar laser with excitation wavelength λ = 514 nm. Regularly oriented pyrolytic graphite exhibits only the G peaks at ~ 1580 cm^{-1} [77, 79]. The G peak is derived from planar carbon-carbon sp^2 valence oscillations and has E_{2g} symmetry. This oscillation occurs for all sp^2 bonds and thus

the presence of a 6-fold aromatic ring is not required to generate the G peak [73, 77, 78, 80]. The height of the G peak may characterize the order of the graphene layers. The expansion of the peak indicates an increase in the irregularity of the inter-bond angles [77]. The D peak is located at ~ 1350 cm^{-1} and does not appear in the ideal graphite. Since the D peak occurs only in the presence of irregularity, the intensity of the given peak is used to characterize the order of the amorphous material. The D peak results from sp^2 oscillations of 6-membered aromatic carbon rings and has A_{1g} symmetry [73, 77, 78, 80]. In addition, a second order D peak, called 2D peak, may occur at ~ 2700 cm^{-1}. This peak characterizes the two-dimensional regularity of graphene layers [81].

The presence and position of the D and G peaks, their intensity ratios (I_D/I_G) and the full width at half maximum (FWHM) value provide information about the material structure. The ratio of D and G peaks intensities (I_D/I_G) characterizes the degree of graphitization of the material [77, 78]. In the case of Tuinstra and Koenig equation, the following principle applies: the smaller the I_D/I_G ratio, the more graphitic is the carbon material and the larger the crystal diameter. The average diameter of the crystallite L_a can be found using the Tuinstra and Koenig (TK) equation:

$$L_a = \frac{C(\lambda)}{I_D / I_G}, \tag{16}$$

where I_D and I_G are D and G peak areas (or intensities), respectively. The parameter C depends on the wavelength and is described by following equation:

$$C \approx C_0 + \lambda C_1, \tag{17}$$

where C_0 = -12.6 nm and C_1 = 0.033. This equation assumes that the crystallites are larger than 2 nm and all C-C bonds are in the sp^2 hybridization. For more amorphous materials, the Ferrari-Robertson (F-R) equation is used, which is applicable in case of crystals smaller than 2 nm:

$$I_D / I_G = C'(\lambda) L_a^2, \tag{18}$$

where $C'(\lambda = 514\ nm) = 4.362$, which is a wavelength-dependent constant. In this equation, the following principle applies: the smaller the I_D/I_G ratio, the more amorphous the carbon and the smaller the crystallite diameter. The higher the synthesize temperature of the carbon material, the narrower the D and G peaks, the lower the FWHM values and the higher the I_D/I_G ratios are as the ordering increases [77–80].

4.4.4. Transmission electron microscopy

Transmission electron microscopy (TEM) is one of the most powerful tools for visual examination of materials in micro and nanoscale. This method allows to achieve atomic resolution and to study the structural properties of thin objects [82–86]. High-resolution transmission electron microscopy (HRTEM) makes it possible to see individual atoms and defects, making it a valuable tool for studying the properties of crystalline materials at nanoscale [84–86].

The two main requirements to work with TEM is the working environment and the thickness of the object. TEM works in vacuum, because even in thinned gases the dispersion of electrons is too high. The object must be thin enough (usually 10 nm to 1 μm) to allow the electrons to pass through without energy losses [84–86]. The resolution of TEM depends mainly on the aberrations of the lenses and images with magnification of 10^3 to 10^6 times can be captured [84].

The electron acceleration voltage is usually in the range of 100–300 kV, but in some cases it can be up to 3 MV [84–86]. When accelerated electrons enter the sample, electrons are scattered. In the interaction between the incoming accelerated electron and the atomic nucleus, elastic scattering occurs, in which case the electron changes its direction, but the energy is not lost. In case of interaction between the accelerated electrons and the electrons at atom, non-elastic scattering occurs and the electron loses its energy significantly. Electrons from elastic scattering are used to produce TEM images and non-elastic scattering is used in electron energy loss spectroscopy (EELS). Energy-dispersive X-ray spectroscopy (EDS/EDX) for energy scattering is used for quantitative analysis [84].

In the TEM images of porous carbon material, the gaps are pores and appear bright because the electron beam passes through them and the atoms are dark, as there is the dispersion of electrons [26].

4.5. Electrochemical measurement techniques

4.5.1. Cyclic voltammetry

Cyclic voltammetry (CV) technique is based on changing the cell potential (U) at a constant scan rate and measure the corresponding current density (j) going through the system [3, 45, 48]. The system is cyclically charged-discharged. The resulting j vs. U plot is called a cyclic voltammogram. In case of an ideal EDLC, the plot has a rectangular shape and a mirror image symmetry of the current responses about the zero current line. In real systems, the porous electrodes have an obstruction of mass transfer and therefore the voltammogram begin to deform, which is particularly evident at higher scan rates. In case of reversible Faradaic reactions there are peaks present in the CV plot, due to which this method is also suitable for studying chemical processes taking place with electrochemically active compounds [42, 45, 54, 55, 89].

The total capacitance C of the electrochemical system can be found according to the equation:

$$C = I(dU / dt)^{-1}, \tag{19}$$

where I is the current flow through the system, $v = \mathrm{d}U/\mathrm{d}t$ is the potential scan rate, U is the cell potential and t is time. If the system consists of two symmetrical electrodes, it is possible to find the specific capacitance C_m (F g^{-1}) of one electrode as follows:

$$C_\mathrm{m} = \frac{2C}{m}, \tag{20}$$

where m is the mass of the active carbon material in one electrode. This equation assumes that the capacitances of the positive and negative electrodes are equal [42, 45, 54, 55, 88, 89].

4.5.2. Constant current charge/discharge measurements

With the constant current (CC) method, a constant current density is applied to the system and the dependence of the potential going through the system over time is measured. This method allows evaluation of several parameters: capacitance, resistance, charge, cyclability/lifetime. The stored charge q is found according to the equation:

$$q = \int_0^t I\mathrm{d}t \tag{21}$$

The internal resistance R of the system can be calculated from the potential drop U_drop that occurs when the current polarity is changed:

$$R = \frac{U_\mathrm{drop}}{\Delta I}. \tag{22}$$

For EDLC, the potential-time graph is usually linear for smaller current densities. In this case, the capacitance can be found from slope of the discharge curve by the following equation:

$$C = I\frac{\mathrm{d}t}{\mathrm{d}U}. \tag{23}$$

For a non-linear curve, the average integral capacitance is found:

$$C = \frac{\int_{\Delta U_1}^{\Delta U_2} j\mathrm{d}t}{\mathrm{d}(\Delta U)} \tag{24}$$

where I is the charge or discharge current, Δt is the discharge or charge time and ΔU is the potential range, where the dependency is linear.

For evaluating the EDLC efficiency, the ratio of charge released and stored is calculated [42, 45, 87].

4.5.3. Electrochemical impedance spectroscopy

To perform electrochemical impedance spectroscopy (EIS) measurement, a sinusoidal potential signal is applied to the system:

$$U(t) = U_0 \sin(\omega t) \tag{25}$$

and the resulting current signal is measured:

$$I(t) = I_0 \sin(\omega t + \varphi), \tag{26}$$

where U_0 and I_0 are the amplitudes of the potential and current signal respectively, $\omega = 2\pi f$ is the angular frequency, t is the time and φ the phase angle.

Usually real electrochemical systems have both a resistive and capacitive component, therefore impedance is defined as:

$$Z(\omega) = Z'(\omega) + jZ''(\omega), \tag{27}$$

where $Z'(\omega)$ and $Z''(\omega)$ are the real and imaginary part of impedance, respectively. In case of the resistive component, the real part of impedance is independent of frequency:

$$Z'(\omega) = R \tag{28}$$

and phase angle $\varphi = 0°$. Capacitive component has frequency-dependent impedance imaginary part:

$$Z''(\omega) = -\frac{1}{\omega C} \tag{29}$$

and phase angle $\varphi = –90°$.

EIS data are usually presented in three different ways: 1) $Z''(\omega)$ vs. $Z'(\omega)$, called Nyquist plot; 2) $|Z(\omega)|$ vs *ac* frequency, called Bode plot; 3) phase angle vs *ac* frequency. In case of an ideal EDLC, only the vertical line, i.e. capacitance, of the $Z''(\omega)$ vs. $Z'(\omega)$ curve is constant over the entire frequency range. For real systems this is not valid, because there is also the mass transfer resistance component. In this case, the graph has a linear region at medium frequency range with a slope value of –45° (so-called Warburg) range, which at lower frequencies turns to a nearly vertical $Z''(\omega)$ vs. $Z'(\omega)$ dependence [3, 42, 43, 48, 50, 54, 88–90].

The capacitance of a real EDLC can be calculated from the EIS data using the following equation:

$$C_s(\omega) = -\frac{1}{\omega Z''(\omega)}. \tag{30}$$

The capacitance can in turn be expressed as a combination of the real and imaginary components:

$$C(\omega) = C'(\omega) - jC''(\omega), \tag{31}$$

where the real component $C'(\omega)$ can be calculated as:

$$C'(\omega) = \frac{-Z''(\omega)}{\omega|Z(\omega)|^2} \tag{32}$$

and imaginary component $C''(\omega)$ is:

$$C''(\omega) = \frac{Z'(\omega)}{\omega|Z(\omega)|^2} \tag{33}$$

The low frequency $C'(\omega)$ value is equal to the capacitance of the EDLC, which can be calculated from the CC charging-discharging methods data and $C''(\omega)$ corresponds to the dissipation of energy during non-reversible Faradaic charge transfer process. $C''(\omega)$ vs. frequency graph shows a maximum at relaxation frequency f_R, which determines the systems time constant τ_R. This is found by the equation:

$$\tau_R = \frac{1}{2\pi f_R}. \tag{34}$$

The time constant τ_R shows how much time it takes to release half of the stored energy [3, 42, 43, 48, 50, 54, 88–90].

4.5.4. Constant power measurements

The constant power method is used to estimate the power and energy densities of the EDLC and is particularly applicable to commercial systems. In this method, the current is changed so that the power is constant over a given range of potentials. This dependency is given by the equation:

$$P = IU = const, \tag{35}$$

where P is the power, I is the current and U is the cell potential.

The time-dependent current I is expressed as:

$$I = C\mathrm{d}U/\mathrm{d}t. \tag{36}$$

Thus, when discharging the EDLC the cell potential decreases, so the current must increase for the power to remain constant. Using the constant power method, it is possible to find the energy vs. power density dependences, the so-called Ragone curves [45].

5. EXPERIMENTAL

In this work silicon carbide derived carbons (SiC-CDC) were synthesized at two different temperatures (1000 °C and 1100 °C), which were subsequently activated with CO_2, steam or with CO_2-steam mixture at different temperatures and times. The effect of activation on porosity and structure of the resulting materials has been studied.

Low-temperature nitrogen sorption measurements data were used to calculate the specific surface area, pore size distribution and porosity of the carbon materials synthesized. X-ray diffraction, Raman spectroscopy and transmission electron microscopy techniques were used to perform structural analysis.

For electrochemical analysis cyclic voltammetry, constant current charging-discharging, electrochemical impedance spectroscopy and constant power methods were used.

5.1. Synthesis and activation of the carbide derived carbons

The following chemicals were used for carbon synthesis and activation:

- α-silicon carbide (Alfa Aesar, 98.5%, 32.5–36.0 μm, main additives Si < 0.6%, SiO_2 < 0.7%, C < 0.4%)
- α-silicon carbide (Alfa Aesar, 99.8%, 2 μm, main additives O_2 0.7%, Al 0.02%, Fe 0.03%, Ca < 0.002%)
- Chlorine Cl_2 (AGA gas, 99.99%)
- Argon Ar (AGA gas, 99.999%)
- Hydrogen H_2 (Linde hydrogen generator NMH2-500, 99.9999%)
- Carbon Dioxide CO_2 (AGA gas, 99.99%)
- Saturated potassium hydroxide solution KOH

The synthesis of silicon carbide derived carbon is described in a simplified manner by the following equation:

$$SiC_{(s)} + 2Cl_{2(g)} \rightarrow SiCl_{4(g)} + C_{(s)}. \quad (37)$$

Silicon carbide was placed in a horizontal tube furnace in a quartz vessel and the system was flushed with argon (flow rate 1000 ml min^{-1}) to remove air. The system has then heated up to the synthesis temperature (1000 °C or 1100 °C) in argon flow, after which gaseous chlorine (100 ml min^{-1}) was directed to the system. Silicon tetrachloride and chlorine residues were led into a neutralizer, which first part contained distilled water and the second KOH solution. After chlorination, the system was cooled down to room temperature under argon flow. The chlorination time applied depended on the selected synthesis temperature, as the reaction proceeds faster at higher temperatures. The completion of

the reaction was evaluated based on the extent of reaction w, which was calculated according to equation:

$$w = \frac{m_{MC} - m}{m_{MC} - m_C}, \tag{38}$$

where m_{MC} is the mass of the initial carbide, m_C the theoretical mass of carbon obtained and m is the actual mass of the carbon prepared. After chlorination, the resulting SiC-CDC was treated with hydrogen at 900 °C for 2 hours to remove $SiCl_4$ and chlorine residues from the carbon material [78].

For CO_2 activation process the resulting SiC-CDC 1000 or 1100 (synthesized from SiC 98.5%, 320 grit) was placed again in a horizontal tube furnace in a quartz vessel. The system was flushed with argon to remove air and then heated up to the activation temperature under argon flow. Upon reaching the appropriate temperature, CO_2 was directed to the system (50 ml min^{-1}). After the activation process, the system was allowed to cool down to room temperature under argon flow. All gases leaving the system were passed through a water trap. After activation the material was treated with H_2 at 900 °C for 1 hour [93, 94].

The steam activation process was carried out in a similar way. The SiC-CDC 1100 (synthesized from SiC 99.8%, 2 μm) carbon materials were activated at fixed temperatures (900 °C and 1000 °C) for 2 hours. The saturated steam content in the carrier gas (Ar or CO_2 for CO_2-steam co-activation) was 47% and the carrier gas flow rate was 50 ml min^{-1}. After activation half of each material was treated with H_2 at 900 °C for 1 hour to remove oxygen-containing functional groups from the surface of the porous carbon material. The other half of the carbon powder was not treated further. This enables the comparison of H_2-treated and non-H_2 treated materials [95, 96].

The loss of mass during activation (activation burn-off) was estimated by equation:

$$x = \frac{m_C - m_{act}}{m_C} * 100\%, \tag{39}$$

where m_C is the initial mass of carbon and m_{act} the mass of carbon after activation.

5.2. Physical characterization

Low-temperature nitrogen sorption measurements were performed using the 3Flex system (Micromeritics). In addition to nitrogen, sorption measurements were also performed with argon and carbon dioxide to establish whether any functional groups on the surface are interacting differently with different gases

(N_2 or Ar) and to get a better estimation of smaller pores with CO_2 testing gas. The sorption measurements with Ar (at –185.15 °C) and CO_2 (at 9.85 °C) were performed using the ASAP 2020 system (Micromeritics). Before measurements, the samples were heated at 350 °C for 12 hours under vacuum. The specific surface area (S_{BET}) and parameters for porous CDC carbon materials were calculated according to BET theory. The total volume of pores (V_{tot}) was obtained at the conditions near to saturation pressure $p/p_0 = 0.97$. The micropore surface area (S_{micro}) and micropore volume (V_{micro}) were calculated using the *t*-plot method. The pore size distributions have been calculated applying non-local density functional theory (NLDFT) to nitrogen adsorption isotherms within relative pressure range from 10^{-7} to 0.95 with new program Solution of Adsoprtion Integral Equation Using Splies (SAIEUS, Micromeritics). Compared to previously introduced modifications of NLDFT, the current application provides smoother and more realistic shape of pore size distribution for different amorphous carbon materials successfully taking into account the surface heterogeneity of amorphous carbons [69–71, 93–96].

XRD analysis were carried out at room temperature, using CuKα radiation (45 kV, 35 mA, $\lambda = 0.154056$ nm) with a step size 0.01° of glancing angle θ and with the holding time of 2 s at fixed θ on Bruker D8 Advance diffractometer and position-sensitive LynxEye detector (Bruker Corporation). The samples were pounded before measurements, because the synthesized materials were not sufficiently homogeneous and contained larger sheets of graphite or flakes. Topaz 4.0 software was used to model the crystalline and amorphous phase content in the carbon material, where the phase ratio was calculated using the Rietveld method. The integral intensity (area) of amorphous carbon peaks was compared to the graphite phase for the estimation of the degree of graphitization of the carbon materials, provided that the first is proportional to the amorphous carbon content. Since both are carbons, it can be assumed that the ratio of integral intensities also corresponds to the ratio of the contents of the amorphous and graphite phase.

The Raman spectra were recorded using a Renishaw inVia micro-Raman spectrometer using Ar laser excitation ($\lambda = 514$ nm). Gauss and Lorentz's combined function was used to model the D- ja G-peaks. Based on the obtained data, the ratio of the intensities of D- and G-peaks of the first order spectrum of Raman was obtained. Using the Ferrari-Robertson equation (18) the crystal size L_a was also calculated.

TEM measurements were performed at acceleration voltage 120 kV with Tecani 12 measuring system in Aalto University. To perform the measurements, a suspension of carbon material was prepared in ethanol, which was applied to copper grid base.

5.3. Electrochemical characterization

The EDLC electrodes comprised of 96 wt% carbon active material and 4 wt% binder (PTFE, Sigma Aldrich, 60% dispersion in H_2O). This mixture

(carbon and binder) was laminated and roll–pressed (HS–160N, Hohsen Corporation, Japan) together to form a 100 ± 5 μm flexible layer of the carbon electrode. After drying under vacuum (10^{-8} mbar), the electrodes were covered from one side with pure Al layer (2 μm) by the magnetron sputtering method.

For the measurements two different electrolytes were used. The organic solvent based electrolyte was prepared from pure acetonitrile (AN, Sigma Aldrich, H_2O < 20 ppm) and from dry $(C_2H_5)_3CH_3NBF_4$ (Stella Chemifa). The room-temperature ionic liquid (RTIL) used was $EMImBF_4$ (Fluka Analytical, for electrochemistry, ≥ 99.0%, H_2O < 200 ppm). The 25 μm thick TF4425 (Nippon Kodoshi) separator sheet was used for mechanical separation of the working electrodes. The two–electrode standard Al test cell (HS Test Cell, Hohsen Corporation) with two identical electrodes (geometric area of about 2.0 cm^2) was completed inside an Ar filled glove box (Labmaster sp, MBraun; O_2 and H_2O concentrations lower than 0.1 ppm) and all electrochemical experiments were carried out at temperature T = 20 °C [93–96].

In case of the RTIL electrolyte, after assembly the cells were left to stand for 24 hours to allow the electrodes to wet with the electrolyte. In addition, before the actual measurement the EDLCs were cycled up to 2.5 V until a stable CV curve was achieved, to ensure that the whole system has been wetted by the ionic liquid. Also, it has to be noted, that the electrolyte was added in small excess to ensure the complete filling of the pores [94, 96].

For electrochemical analysis the following methods were used: cyclic voltammetry (CV), constant current charge/discharge (CC/CD) and the electrochemical impedance spectroscopy (EIS) methods, using a SI1287 Solartron potentiostat and 1252 A frequency response analyzer over *ac* frequency (*f*) range from 1 mHz to 300 kHz at 5 mV modulation. The constant power method (using a BT2000 testing system, Arbin Instruments, USA) has been used for obtaining the experimental Ragone (energy density vs. power density) plots. For data analysis CorrView, Zview and MS Excel softwares were used [93–96].

6. RESULTS

6.1. Effect of chlorination and activation parameters

In this study, it was found that the carbon synthesis temperature has a significant influence on the reaction time and rate. Higher chlorination temperature lead to faster carbon synthesis. Depending on the synthesis temperature and the amount of initial carbide, the minimum reaction time applied was 8 hours and maximum 16 hours. The synthesis resulted in an average of 10 grams of carbon (with a reaction yield ~30%, relative to the initial carbide mass). According to the data of extent of reaction calculations (Eq. 38), the reactions were fully completed at both temperatures (1000 °C and 1100 °C), at lower temperatures the chlorination reaction did not proceed completely to end within a reasonable time and unreacted carbide particles remained in the CDC.

Activation of SiC-CDC with CO_2 also proceeded more rapidly at a higher temperature. Table 1 shows the burn-off values resulting from SiC-CDC activations at different temperatures and activation times. The highest burn-off value was obtained with activation at 950 °C for 16 hours and the lowest at 900 °C. At lower temperatures the reaction slowed down considerably and achieving higher burn-off values took much more time. At higher temperatures the good burn-off values could be achieved in a significantly shorter periods of time. However, the characterization of the carbon materials revealed that it was not important at what temperature or time the burn-off was achieved, but the burn-off amount itself was decisive.

Table 1. Synthesis parameters of CO_2-activated SiC-CDC materials.

Abbreviation	Synthesis temperature (°C)	CO_2 activation temperature (°C)	Activation time (h)	Activation burn-off (%)
SiC-CDC 1000	1000	-	-	-
SiC-CDC 1000 A1	1000	900	6	15
SiC-CDC 1000 A2	1000	950	3	30
SiC-CDC 1000 A3	1000	950	8	48
SiC-CDC 1100	1100	-	-	-
SiC-CDC 1100 A1	1100	900	6	19
SiC-CDC 1100 A2	1100	950	3	29
SiC-CDC 1100 A3	1100	950	16	68

The results for steam and CO_2-steam co-activation were similar, especially regarding the final activation burn-off percentage (Table 2). Main difference is that the steam activation reaction proceeds more rapidly, so similar results can be achieved in a much shorter reaction time. Also the steam activation processes had better repeatability, compared to CO_2 activation. Activations carried out

below 900 °C resulted in a burn-off about 2 to 8%, which is not sufficient. Also the saturated steam content in the carrier gas gave a smaller effect on the activation, when the values were lower than 47%, whereas at higher contents the steam began to condense, due to which 47% was observed to be the optimum value. Using Ar as the carrier gas for steam activation, the achieved burn-off values were slightly lower than for steam-CO_2 co-activation, where CO_2 was used as the carrier gas. Therefore the carrier gas has some influence on the parameters of the resulting activated carbon material.

Table 2. Synthesis parameters of steam and CO_2-steam co-activated SiC-CDC materials.

Abbreviation	H_2O (%)	Activation time (h)	Carrier gas	Activation temperature (ºC)	Activation burn-off (%)	H_2 treated
St-900	47	2	Ar	900	15	No
St-900-H2						Yes
St-1000			Ar	1000	50	No
St-1000-H2						Yes
St-CO2-900			CO_2	900	19	No
St-CO2-900-H2						Yes
St-CO2-1000			CO_2	1000	60	No
St-CO2-1000-H2						Yes

Since the SiC-CDC 1100 chlorination process proceeds faster than SiC-CDC 1000 reaction and all different analysis results showed for SiC-CDC 1000 based materials very similar or slightly lower values, then this study focuses on the SiC-CDC 1100 based activated materials.

6.2. Physical characterization

6.2.1. X-ray diffraction analysis

The XRD patterns of SiC-CDC CO_2 activated materials (Fig. 1a) show in all diffractograms two (002) ($2\theta \sim 26°$) peaks, where the first is a flat and the other is a narrow peak. This is caused by the non-homogeneity of the materials. As the activation burn-off increases, the intensity of the flat (002) peak somewhat decreases and the intensity of the narrow sharp peak increases. The narrow peak characterizes the graphite phase and the flat diffuse (002) peak is resulting from amorphous carbon. Thus, it can be concluded that during the activation process,

CO_2 reacted preferably with the amorphous part of the carbon material and the graphite phase content slightly increases due to the high temperature treatment. In addition to the double (002) peak, the (004) ($2\theta \sim 54°$) peak is also present in the diffractogram, both of which characterize the parallel graphene layers, and the (100/101) ($2\theta \sim 43°$) peak, which can be associated with the 2D in-plane symmetry along the graphene layer. Nevertheless, the intensities of the (004) and (100/101) peaks are small and do not change significantly.

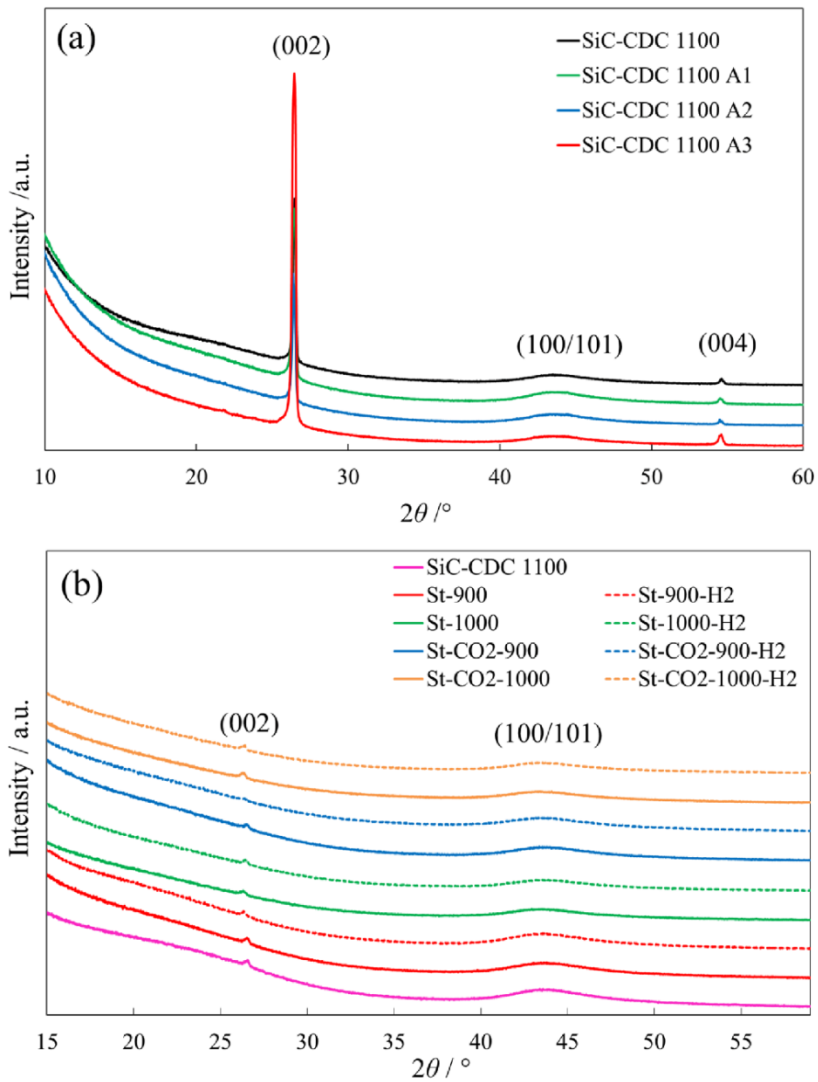

Figure 1. XRD spectra of SiC-CDC CO_2 activated materials (a) and steam activated materials (b).

The XRD patterns for steam and CO_2-steam co-activated materials (Fig. 1b) are all almost identical. The patterns show low intensity reflections at $2\theta \sim 26°$ (002) peak and at $2\theta \sim 43°$ (100/101) peak, which refer to small graphitic areas but there is no significant long-range ordering of material. Therefore these results show that no structural changes take place during the steam activation process. It also has to be noted that the steam activation reaction time was only 2 hours, which is considerably shorter time compared to CO_2 activation processes conducted. Due to this, CO_2-activated materials which had a long high temperature treatment, have resulted in a higher graphite phase content. Also, the non-homogeneity of the materials and different particle size have somewhat influence on difference of the spectras.

The graphite and amorphous phase content in the carbon materials were calculated using the Rietveld method. The results showed the graphite phase content 0.8 to 1.5% and amorphous phase 98.5 to 99.2% for all the materials studied. However, taking into account the uncertainty of the calculation method used, no clear correlations of the influence of activation on the structure of the resulting carbon material can be established.

From the XRD data analysis it can be concluded that all the SiC-CDC materials resulting from both activation methods are all mainly amorphous with a small graphite phase content and no remarkable structural changes take place during the activation processes [93, 95]

6.2.2. Raman spectroscopy data

The Raman spectra for CO_2 activated materials (Fig. 2a) and steam activated materials (Fig. 2b) look very similar and same tendencies can be observed for both material groups. The spectra are characteristic of disordered amorphous carbon and show three peaks: the disorder-induced D-peak at ~ 1350 cm^{-1}, the so-called graphite G-peak at ~ 1580 cm^{-1} and the second-order peak of D-band 2D-peak at ~ 2700 cm^{-1}. The spectra of all the activated materials coincide very well, due to which it can be concluded that the carbon structure and morphology did not change significantly during the activation processes. Although the structural changes are minimal, it can be identified, that with the increase of burn-off during activation, the peaks become a bit narrower. This refers to the increase in the structural order, which is also consistent with the XRD analysis results. Based on the results of Raman spectroscopy, the average diameter of crystallite L_a was calculated, applying the Ferrari-Robertson formula (Eq. 19), using the peak areas in the calculations. This formula is more suitable than Tuinstra-Koenig's, as the crystallites are smaller than 2 nm. The results of the L_a calculations were very similar for all the studied materials, having L_a values in the range of 0.77 to 0.79 nm. Although the average diameter of the crystallite does not change significantly, there is a slight increase in the I_D/I_G ratio, correspondingly to the activation burn-off increase, indicating an increase in the structural order. This also confirms the previous conclusion that with high

temperature activation the order in the carbon material increases and the burn-off takes place rather from the amorphous material phase regions [93, 95].

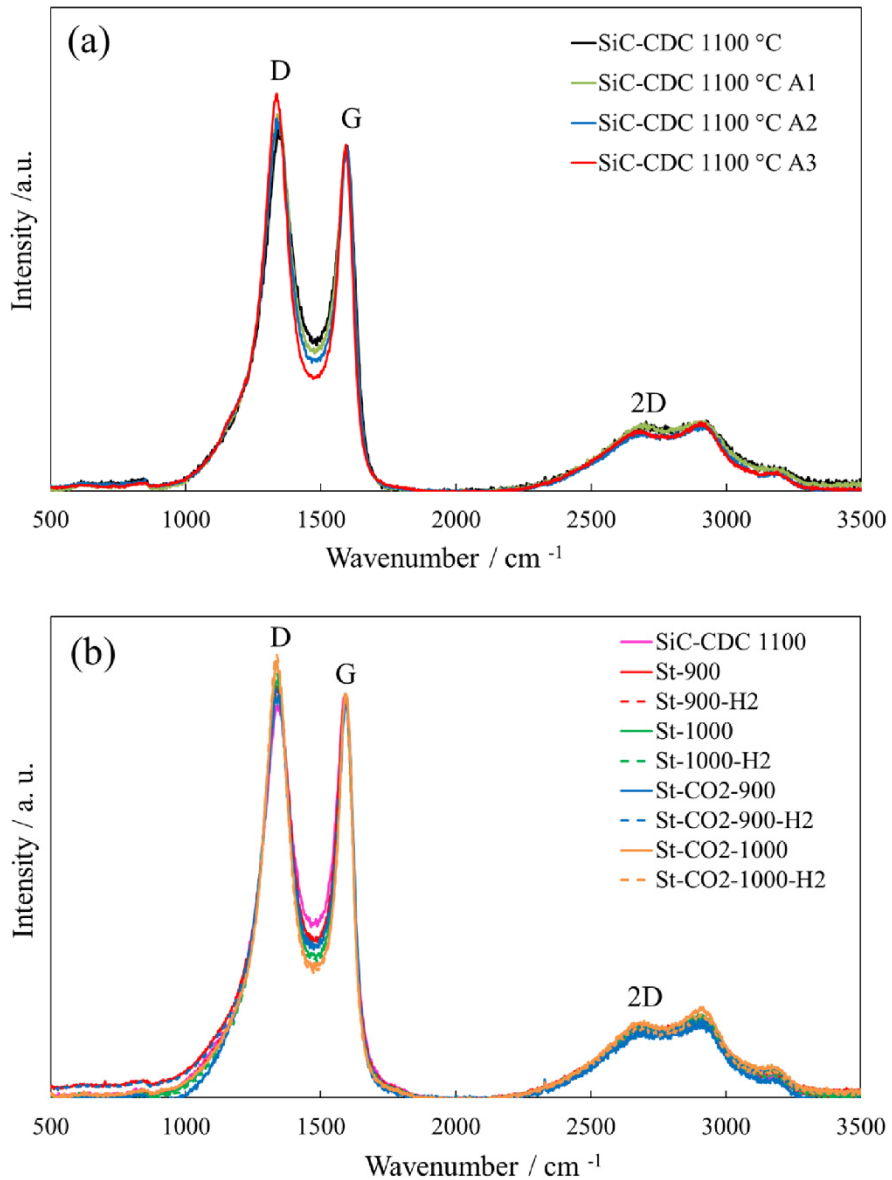

Figure 2. Raman spectra of SiC-CDC CO_2 activated materials (a) and steam activated materials (b).

6.2.3. HRTEM analysis

HRTEM studies of the CDC materials revealed the microstructure at the atomic scale. The images show that structure is similar in the initial SiC-CDC 1100 material (Figs. 3a–b) as well as in the activated SiC-CDC 1100 A2 material (Figs. 3c–d). For both it can be seen that the materials contain in addition to the mainly amorphous carbon also some graphitic layers, which are mostly located in outer areas.

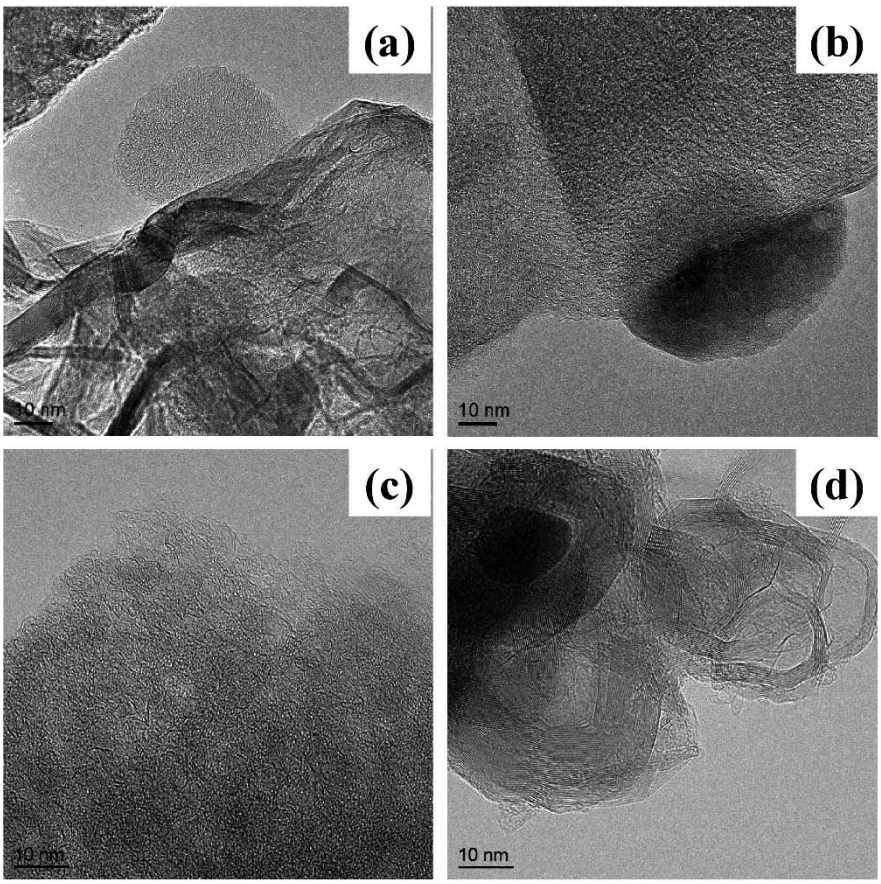

Figure 3. HRTEM images for SiC-CDC 1100 (a, b) and SiC-CDC 1100 A2 (c, d).

The examination of the HRTEM images showed that the materials contain some impurities (Fig. 4). EDS analysis was used to determine this more exactly and it was identified that the materials contain aluminum oxide particles, which is likely originating from the initial carbide.

Overall the information obtained from the TEM images is consistent with the results of other analysis methods, which suggest that the material is mostly amorphous with some smaller more graphitic areas [93].

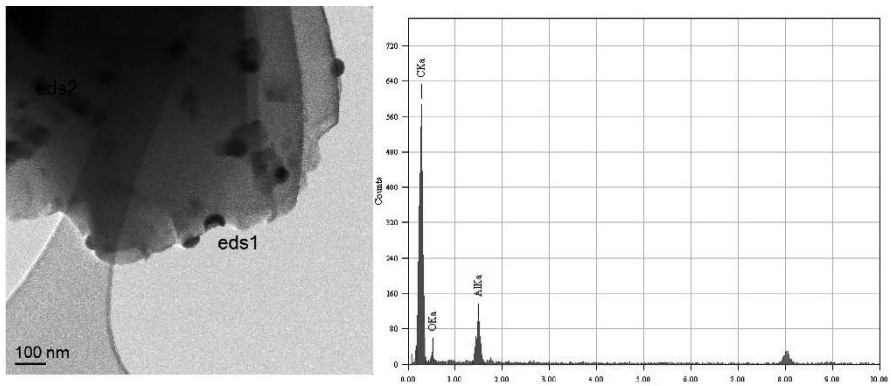

Figure 4. EDS analysis

6.2.4. Porosity characteristics

Characteristics calculated from the results of low-temperature N_2 sorption measurements are shown in Table 3. A clear correlation between the sorption characteristics and activation burn-off value was found – as the burn-off increases, the values of S_{BET}, V_{tot} and average pore size increase. The corresponding values are the highest for the steam-CO_2 co-activated material St-CO2-1000, which also had the second higher burn-off percentage (60%). Although the materials are still mainly microporous, there is some increase in the mesoporosity as the burn-off increases. Figure 5 shows that overall with similar burn off percentages, steam activation results in materials with higher S_{BET} and V_{tot} values.

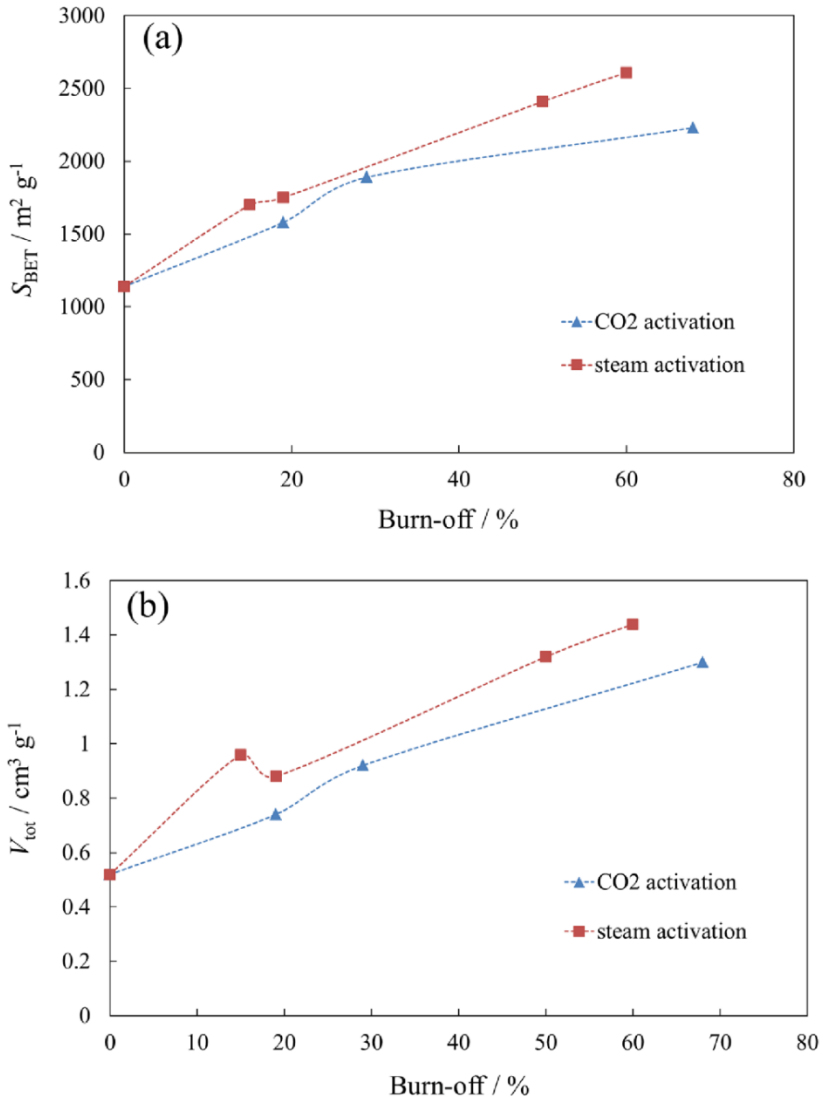

Figure 5. Burn-off vs. specific surface area (a) and burn-off vs. total pore volume (b) dependencies for CO_2 and steam activation methods.

Table 3. Results of the sorption measurements for initial SiC-CDC 1100 and corresponding CO_2 activated and steam activated materials.

Abbreviation	S_{BET} ($m^2 g^{-1}$)	S_{micro} ($m^2 g^{-1}$)	V_{micro} ($cm^3 g^{-1}$)	V_{tot} ($cm^3 g^{-1}$)
SiC-CDC 1100	1140	1135	0.51	0.52
SiC-CDC 1100 A1	1580	1575	0.71	0.74
SiC-CDC 1100 A2	1960	1948	0.88	0.92
SiC-CDC 1100 A3	2230	2192	1.22	1.30
St-900	1700	1570	0.77	0.96
St-900-H2	1720	1620	0.73	0.87
St-1000	2410	2260	1.09	1.32
St-1000-H2	2290	2180	1.00	1.35
St-CO2-900	1670	1600	0.72	0.82
St-CO2-900-H2	1750	1660	0.74	0.88
St-CO2-1000	2610	2470	1.22	1.44
St-CO2-1000-H2	2400	2270	1.20	1.32

The adsorption/desorption isotherm (Figs. 6a-b) for the initial SiC-CDC 1100 can be classified as type I isotherm, according to IUPAC classification, which is characteristic for microporous materials. For all the SiC-CDC activated materials the isotherms are either type I or type IV. Type I isotherms can be observed for the activated materials that had smaller activation burn-off values, so they were still mainly microporous and similar to the initial SiC-CDC. Type IV isotherms were established for the materials with higher activation burn-off values, which suggest that the mesoporosity of these materials has been increased. In some cases also small hysteresis can be seen in the isotherms, which suggests that capillary condensation of the adsorbate takes place in the mesopores developed during activation.

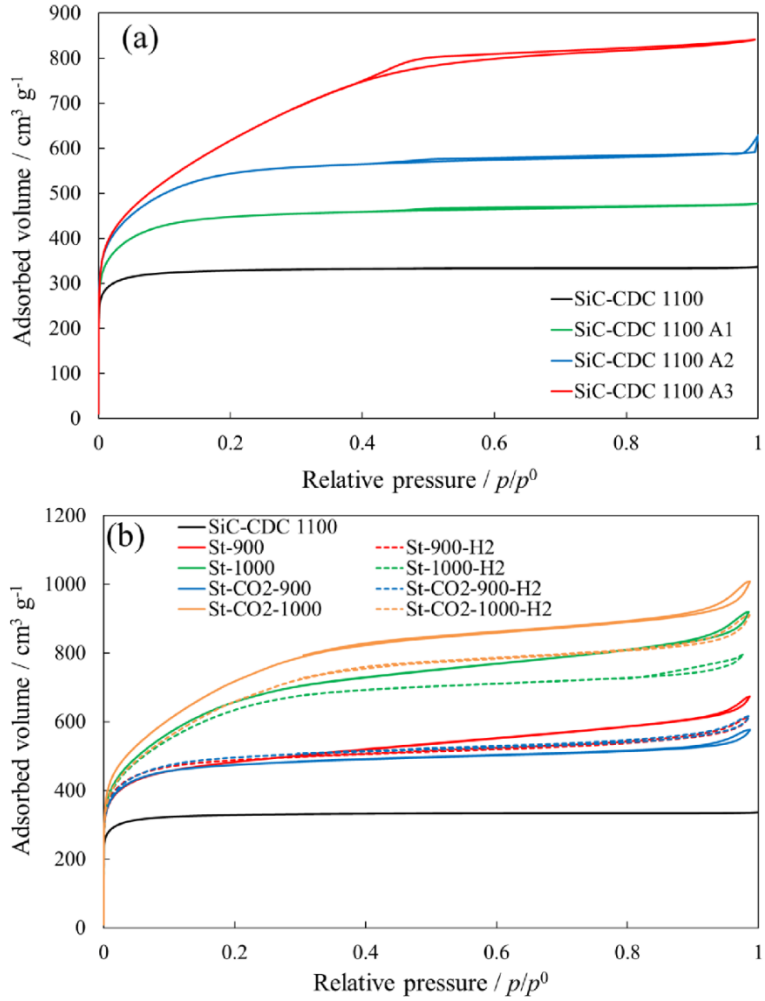

Figure 6. Low-temperature N_2 adsorption/desorption isotherms for SiC-CDC CO_2 activated materials (a) and steam activated materials (b).

The pore size distributions plots calculated by the SAIEUS method (2D-NLDFT-HS) are given in Figure 7. The initial SiC-CDC 1100 is microporous, but both activation methods increase noticeably the mesoporosity of the CDC materials. Higher activation temperatures lead to higher activation burn-off values, which in turn lead to increased mesoporosity. The comparison between the steam activated SiC-CDCs materials with additional H_2-treatment and non-treated powders (Fig. 7b) show that the H_2-treatment has a minimal effect on the porosity characteristics. Some differences may result also from measurement and modeling accuracy. Overall, it can be observed that both CO_2 and steam activations have a significant effect on widening of the pores [93–95].

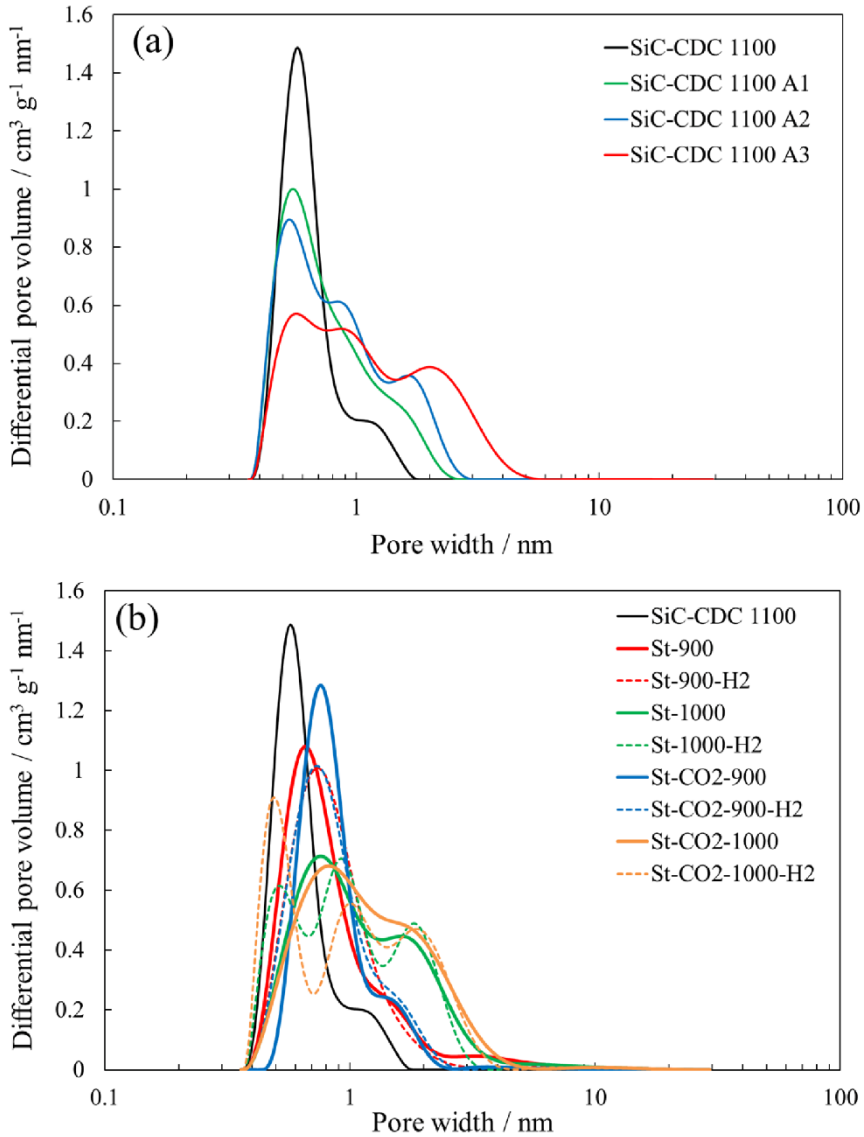

Figure 7. Pore size distributions of SiC-CDC CO_2 activated materials (a) and steam activated materials (b).

For the SiC-CDC steam activated materials, additionally H_2-treated and non-treated samples, sorption measurements were also performed with Ar and CO_2, in addition to N_2, to determine if there are any functional groups on the carbon surface interacting differently with different gases (Ar or N_2) and also using CO_2 to get better estimation of smaller micropores. The results for St-1000 and St-1000-H2 using different gases are shown in Figure 8, but these tendencies

were similar for all the measured materials. As expected, the data for CO_2 measurement shows a bigger peak below 1 nm, i.e. for the smallest pores, whereas Ar and N_2 show more peaks within a bit wider range. Also there is small dependence of the peak position on the gas used, which indicates that there might be specific adsorption interactions between the used gas and the carbon surface. However, the pore size distribution plots shape depends on the model used for fitting the adsorption data. Nevertheless, the comparison of Ar and CO_2 adsorption confirms that the difference between H_2 treated and H_2-untreated materials is negligible. However N_2 adsorption data shows some influence of the H_2 treatment step on the shape of pore size distribution [95, 96].

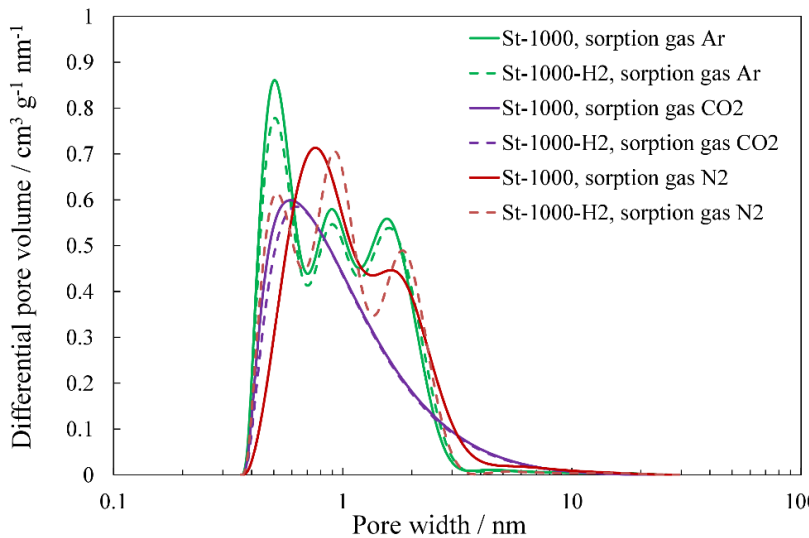

Figure 8. Pore size distribution plot for different gases (N_2, CO_2, Ar), obtained using SAIEUS method.

6.3. Electrochemical characterization

6.3.1. Cyclic voltammetry data

6.3.1.1. CV data for EDLCs in 1M $TEMABF_4$+AN

In this study all the CV curves are expressed as specific gravimetric capacitance ($C_{m;CV}$) vs. cell potential (U). The CVs were measured within various electrode potential regions at potential scan rates (v) from 1 to 500 mV s^{-1}. The SiC-CDC CO_2-activated materials (Fig. 9) and steam activated materials (Fig. 10) both show very similar behavior, having a nearly mirror image symmetry of the current response about the zero current line, obtained at $U \leq 3.0$ V and $v \leq 200$ mV s^{-1}. All the materials even continued showing quite good capacitive

behavior up to 3.4 V. On the contrary for the non-activated initial SiC-CDC 1100 poor capacitive behavior was observed, even at low cell potentials and low scan rates. Although the materials had different activation and treatment parameters and as a result of that they also differed by their porosity parameters, all CV curves are quite similar and also the differences in capacitance are not remarkable. Therefore the $S_{BET,}$ V_{tot} and other porosity parameters have only a moderate influence on the EDLCs electrochemical parameters.

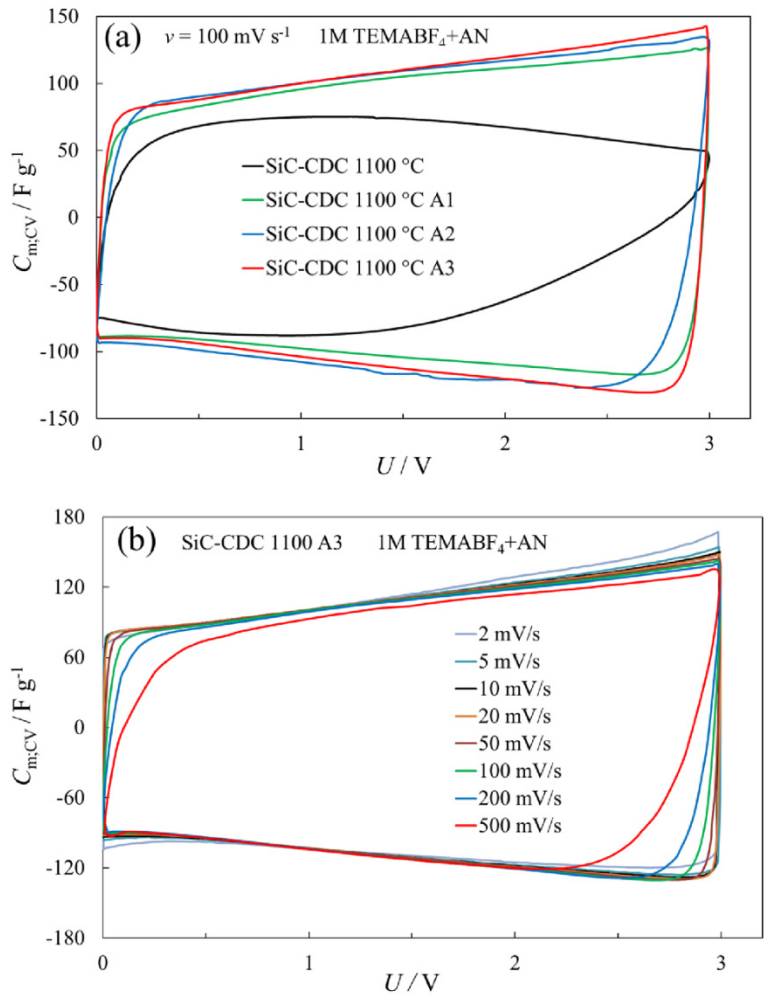

Figure 9. Cyclic voltammograms for CO_2 activated materials at potential scan rate 100 mV s^{-1} (a) and SiC-CDC 1100 A3 material at different potential scan rates (b).

The specific gravimetric capacitance $C_{m;CV}$ values were calculated (Eqs. 19, 20) from the linear region of the CV curves after changing the direction of the potential scan rate at U = 3.0 V and are shown in Table 4. The capacitance values increased up to 2.5 times compared to the initial SiC-CDC 1100 (56 F g^{-1}). The highest capacitance value obtained for the CO_2-activated materials was 125 F g^{-1} and for the steam activated materials 142 F g^{-1}. Thus, the EDLCs based on steam activated materials demonstrated a bit higher capacitance values compared to CO_2-activated systems [93, 95].

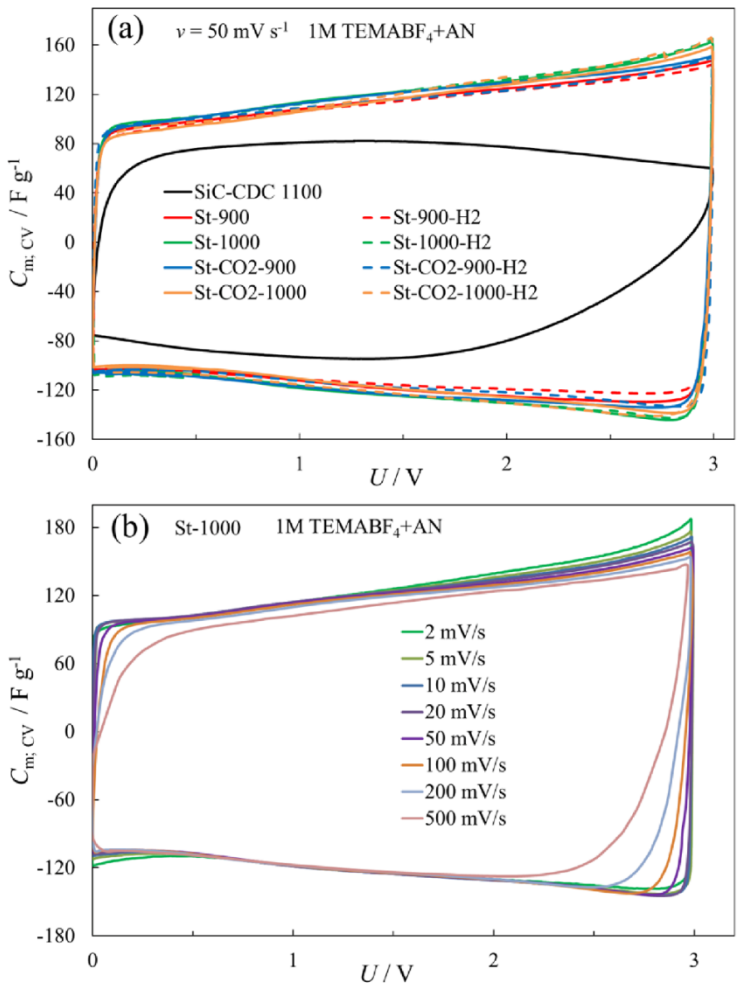

Figure 10. Cyclic voltammograms for steam activated materials at potential scan rate 50 mV s^{-1} (a) and St-1000 material at different potential scan rates (b).

Table 4. Calculated specific capacitance values from cyclic voltammetry (U = 2.7 V; v = 100 mV s^{-1} discharge capacitance), constant current (U = 2.7 V; j = 5 mA cm^{-2}) and impedance spectroscopy measurements (U = 3.0 V; f = 1 mHz) data.

Abbreviation	Cyclic voltammetry (F g^{-1})	Constant current (F g^{-1})	Impedance spectroscopy (F g^{-1})
SiC-CDC 1100	56	43	40
SiC-CDC 1100 A1	113	91	108
SiC-CDC 1100 A2	121	109	125
SiC-CDC 1100 A3	125	101	122

Calculated specific capacitance values from cyclic voltammetry (U = 3.0 V; v = 5 mV s^{-1}), constant current (U = 3.0 V; j = 1 A g^{-1}) and impedance spectroscopy measurements (U = 3.0 V; f = 1 mHz) data.

St-900	134	116	132
St-900-H2	126	112	123
St-1000	142	118	141
St-1000-H2	138	118	134
St-CO2-900	125	117	135
St-CO2-900-H2	132	113	132
St-CO2-1000	124	115	135
St-CO2-1000-H2	130	115	136

6.3.1.2. CV data for EDLCs in $EMImBF_4$

The EDLCs based on different SiC-CDC activated materials as electrode materials and $EMImBF_4$ as an electrolyte were studied by using the CV method. The CV curves were measured at different potential scan rates from 1 to 500 mV s^{-1} and in a very wide cell potential range up to 3.8 V (sometimes up to 4.0 V), to obtain the region of ideal polarizability.

Figure 11a clearly shows that the SiC-CDC 1100 material has very limited capacitance values, this is due to the too narrow pore sizes, which are inaccessible for $EMImBF_4$ electrolyte ions. The CV curves for CO_2 activated materials (Fig. 11a) indicate influence of the activation parameters on the resulting EDLC capacitive behavior. The CO_2 activated SiC-CDC materials based EDLCs demonstrate in $EMImBF_4$ nearly ideal capacitive behavior at scan rates $v \leq 20$ mV s^{-1} and up to $U \leq 3.6$ V (Fig. 11b, Fig. 13a). At cell potentials $U \geq 3.6$ V the $C_{m;CV}$ values start increasing exponentially, which is caused by the decomposition of an insignificant amount of residual water in $EMImBF_4$, due to which electrochemical reduction of O_2 and H_2O traces takes place. At potential scan rates over 20 mV s^{-1} the CV curves become distorted in the region of potential switchover due to the slow mass-transfer step in the porous CDC matrix because of the high viscosity of $EMImBF_4$.

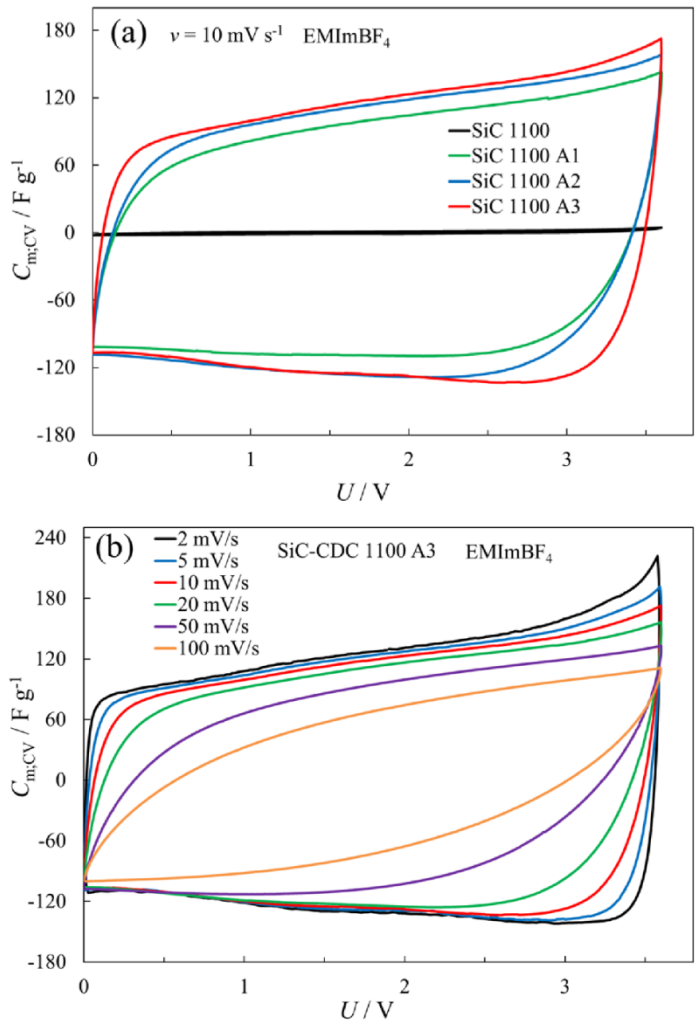

Figure 11. Cyclic voltammograms for CO_2 activated materials at potential scan rate 10 mV s^{-1} (a) and SiC-CDC 1100 A3 material at different potential scan rates (b).

The SiC-CDC steam activated materials based EDLCs demonstrate nearly ideal capacitive behavior at $v \leq 50$ mV s^{-1} and up to $U \leq 3.6$ V (Figs. 12a-b, Fig. 13b). Even at $U \leq 3.8$ V there are only small deviations from ideal capacitive behavior. At lower v values some increase of faradaic capacitance can be observed, explained by the slow mass transfer process of electrochemically active residual component (H_2O) from $EMImBF_4$ to the electrode surface. At moderate potential scan rates $20 < v < 200$ mV s^{-1} small deviations from the ideal capacitive behavior CV shape are caused by very low concentration of residuals in the systems under study. Figure 12a shows that St-CO2-900 based EDLC falls out from the others and has smaller capacitance value. This is due to

the smallest S_{BET}, V_{micro} and V_{tot} values (Table 3) and narrowest pore size distribution (Fig. 7), being more similar to the CO_2 activated materials. For all the other steam activated materials very similar electrochemical behavior is observed.

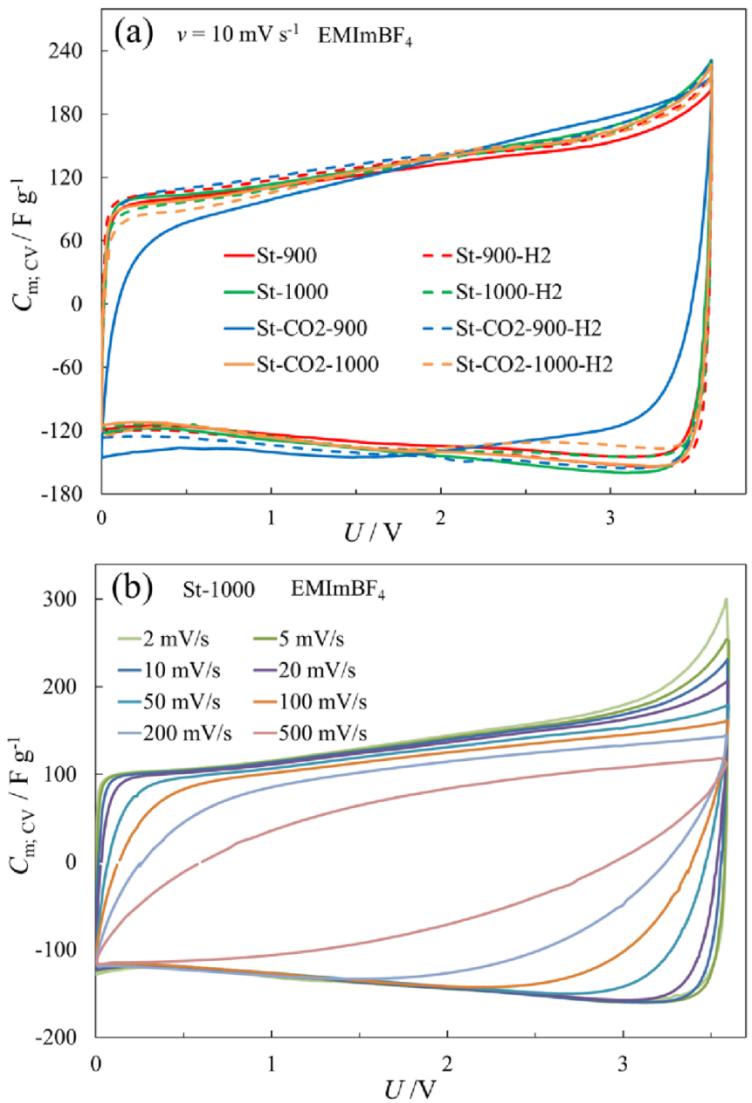

Figure 12. Cyclic voltammograms for steam activated materials at potential scan rate 10 mV s^{-1} (a) and St-1000 material at different potential scan rates (b).

Comparing the CO_2 and steam activated materials we can see that steam activated materials based EDLCs allow using a bit higher potential scan rates and have a lower influence of IR-drop on the shape of CV curves, where the capacitive behavior remains nearly ideal. This is mainly due to the more expressed amount of bigger micropores and mesopores at the steam activated materials surface, which decreases the mass-transfer resistance of electrolyte in the mesoporous matrix.

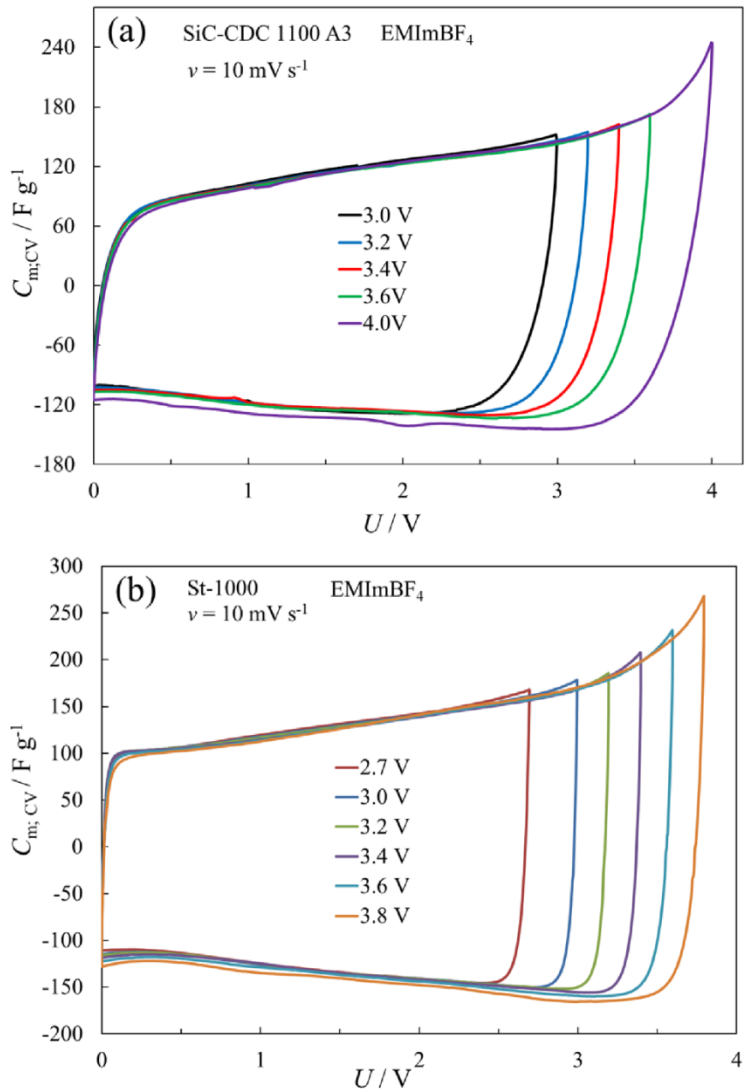

Figure 13. Cyclic voltammograms at different cell potentials for CO_2 activated SiC-CDC 1100 A3 material (a) and steam activated St-1000 material (b).

The $C_{m;CV}$ values calculated (Eqs. 19–20) for both CO_2 and steam activated materials based EDLCs are given in Table 5. For the SiC-CDC 1100 material the $C_{m;CV}$ value is only 5 F g^{-1}, but the CO_2 activated materials obtained capacitance up to 129 F g^{-1} and steam activated materials up to 145 F g^{-1}. Therefore, here the huge influence of activation conditions on the SiC-CDC materials is clearly proven.

As the CV data showed, the activated SiC-CDC materials differed only a little in their electrochemical behavior, although their activation and treatment parameters as well as their specific surface areas and pore volumes were different. This confirms again the previously observed correlation – micro-porous region characteristics determine the nearly linear correlation between specific surface area and capacitance values, visible up to $S_{DFT} \sim 1000$ m^2 g^{-1} [94, 96].

Table 5. Calculated specific capacitance values from cyclic voltammetry (U = 3.6 V; v = 1 mV s^{-1} discharge capacitance), constant current charge (discharge) (U = 3.0 V; j = 0.1 A g^{-1}) and impedance spectroscopy measurements (U = 3.6 V; f = 1 mHz) data.

Abbreviation	Cyclic voltammetry (F g^{-1})	Constant current (F g^{-1})	Impedance spectroscopy (F g^{-1})
SiC-CDC 1100	3	0.15	NA
SiC-CDC 1100 A1	118	84	136
SiC-CDC 1100 A2	124	130	155
SiC-CDC 1100 A3	129	138	170

Calculated specific capacitance values from cyclic voltammetry (U = 3.6 V; v = 10 mV s^{-1}), constant current (U = 3.0 V; j = 1 A g^{-1}) and impedance spectroscopy measurements (U = 3.6 V; f = 1 mHz) data.

St-900	132	120	148
St-900-H2	140	124	157
St-1000	145	125	162
St-1000-H2	138	120	165
St-CO2-900	131	130	142
St-CO2-900-H2	143	125	157
St-CO2-1000	138	121	154
St-CO2-1000-H2	133	117	148

6.3.2. Constant current charge/discharge measurements results

6.3.2.1. CC data for EDLCs in 1M $TEMABF_4$+AN

The EDLCs based on SiC-CDC CO_2-activated materials and 1M $TEMABF_4$+AN were tested at constant current charge/discharge regimes from 1 to 50 mA cm^{-2} at cell potentials from 0 to 2.7 V. The EDLCs based on SiC-CDC steam activated materials were tested similarly, from 0.05 to 1 A g^{-1} at cell potentials from 0 to 3.0 V. This *U* region correlates to the maximum limit of commercially available EDLCs. The discharge and charge capacitances C_{cc} were calculated from the data of the third cycle. Since the CC/CD plots are not ideally linear, the integration of CC and CD has been conducted and integral capacitance values have been calculated according to Eq. 24. The calculated C_{cc} values for all the studied systems are shown in Table 4. The slightly lower C_{cc} values compared to capacitance values obtained by the CV method can be explained by the physical differences in the CV and CC/CD methods and also the adsorption equilibrium of ions in the micro-mesoporous surfaces might not be entirely established. Nevertheless, the values obtained are consistent with each other and the same tendencies occur. In Figure 14 it is clearly visible, that the curve for the SiC-CDC 1100 is non-linear and non-symmetrical and also the capacitance is quite low. Figure 14 and 15 show that for both types of the activated materials the curves are nearly linear and quite symmetrical and the IR-drop is negligible, even at higher current densities applied. Therefore, CO_2-activated and steam activated SiC-CDC materials based EDLCs with TEMABF4+AN as the electrolyte show nearly ideal capacitive behavior. The coulombic efficiency has been calculated as a ratio of charge released and accumulated during discharging and charging of EDLCs. For all the CO_2-activated systems the efficiency values remained within the range of 98 to 99% and for the steam activated systems within the range of 99 to 100%. Therefore the SiC-CDC activated materials show a great potential for different energy storage applications [93, 95].

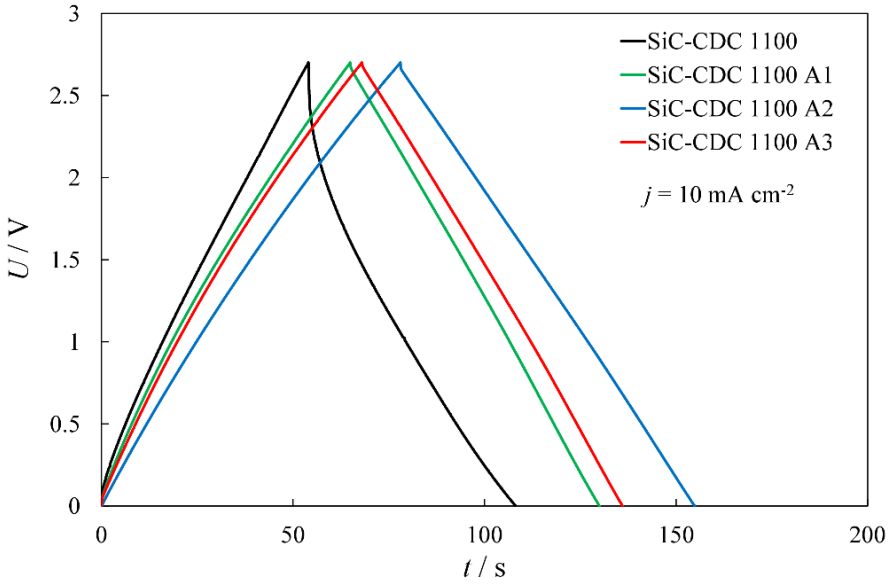

Figure 14. Constant current charge/discharge data at j = 10 mA cm^{-2} for the CO_2 activated materials.

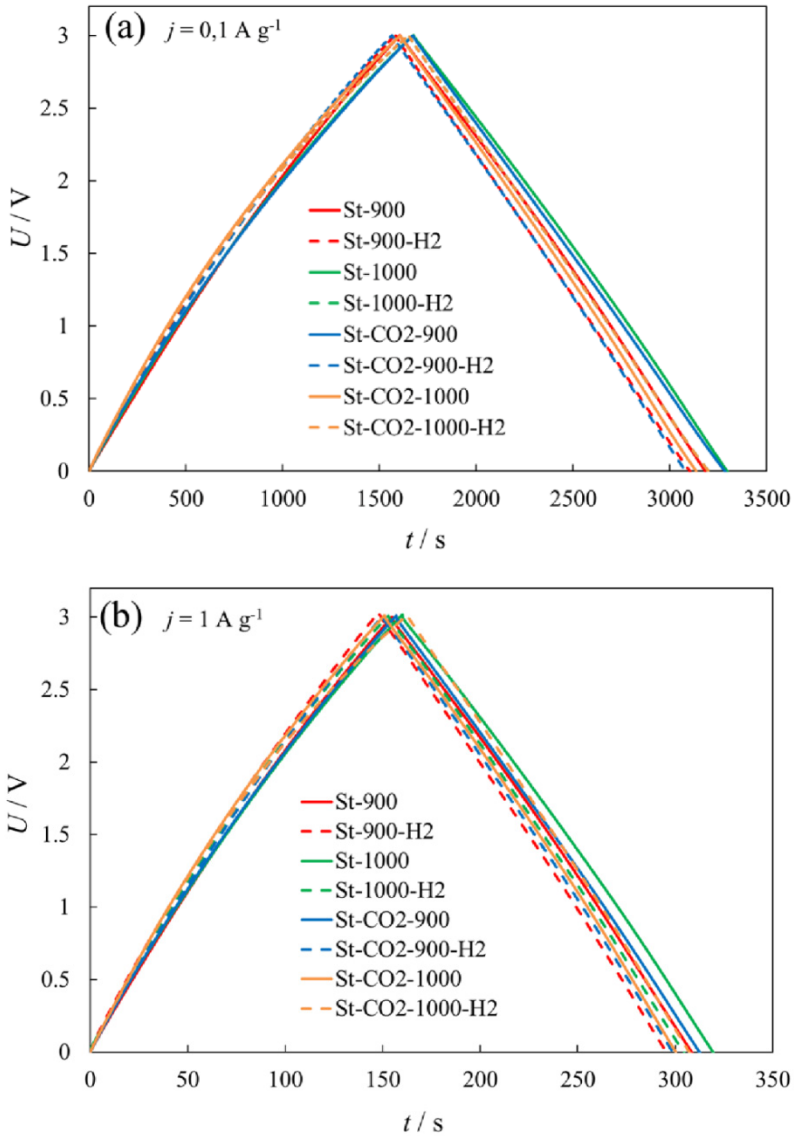

Figure 15. Constant current charge/discharge data for steam activated materials at j = 0.1 A g^{-1} (a) and j = 1 A g^{-1} (b).

6.3.2.2. CC data for EDLCs in $EMImBF_4$

The CO_2 and steam activated materials and $EMImBF_4$ ionic liquid based EDLCs were both tested at different fixed constant current regimes from 0.01 to 5 A g^{-1} applying charging-discharging steps within the cell potentials from 0 to 3.0 V (Figs. 16 and 17). The calculated C_{cc} values are shown in Table 5.

The CC/CD curves for CO_2 activated materials are almost symmetrical and linear at j = 0.1 A g^{-1} (Fig. 16a), but at higher current densities j = 1 A g^{-1} (Fig. 16b) the curves are distorted to a higher extent. It is visible that the IR-drop increases significantly, which is caused by the slow mass-transfer process. The SiC-CDC 1100 A1 data differs noticeably from the other CO_2 activated materials characteristics due to its smallest S_{BET}, V_{micro}, V_{tot} and the narrowest pore size distribution, which are not sufficient enough when using $EMImBF_4$ as the electrolyte.

The CC/CD curves for steam activated materials are nearly linear and symmetrical at smaller current densities (Fig. 17a). At higher current densities (Fig. 17b) there is only a weak deviation from the linear shape and a small IR-drop can be observed. Therefore, these completed EDLCs demonstrate excellent electrochemical reversibility. The St-CO2-900 is here again the exception, which behaves more like the CO_2 activated material due to its low porosity and pore size characteristics.

The coulombic efficiencies were for both activated materials in the range of 97 to 99% at j = 0.1 A g^{-1} and 99 to 100% at j = 1 A g^{-1} [94, 96].

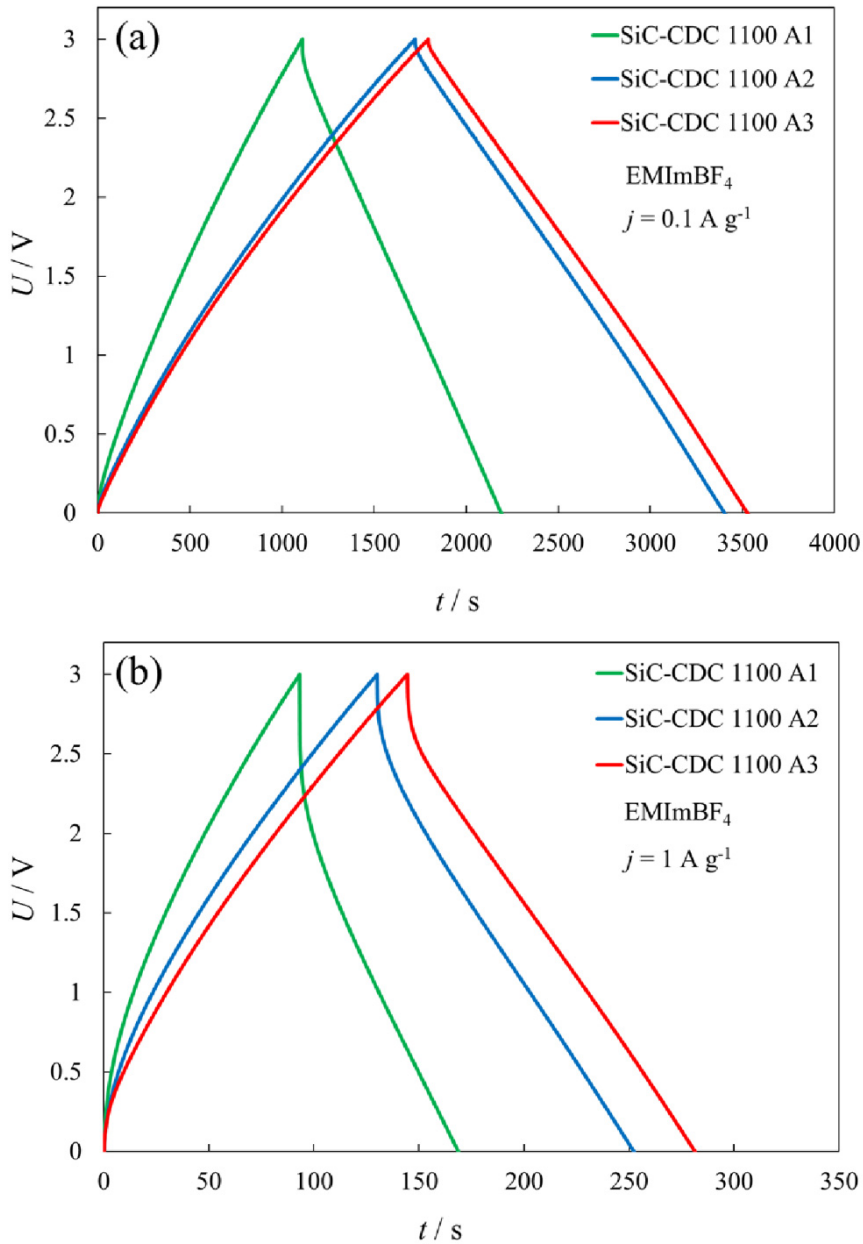

Figure 16. Constant current charge/discharge data for CO_2 activated materials at j = 0.1 A g^{-1} (a) and j = 1 A g^{-1} (b).

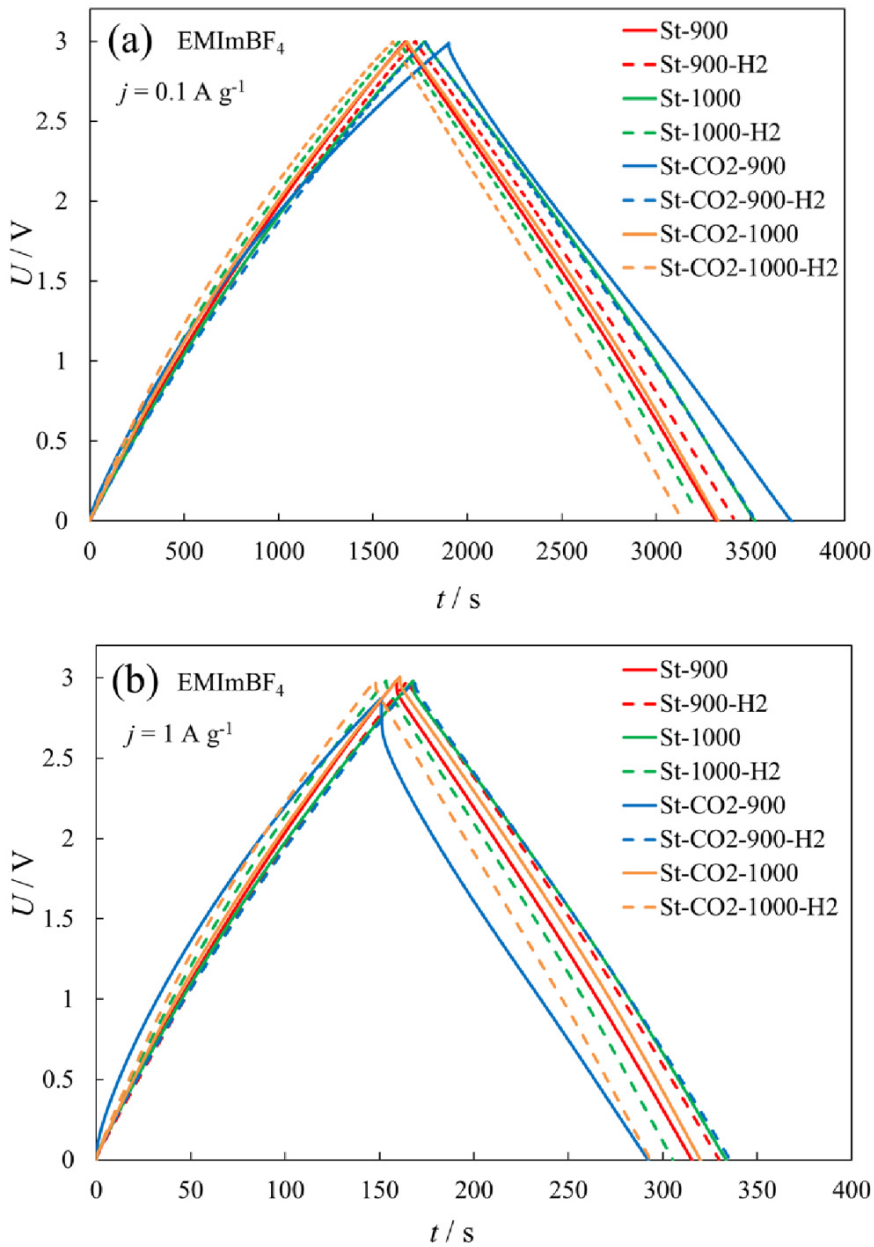

Figure 17. Constant current charge/discharge data for steam activated materials at j = 0.1 A g^{-1} (a) and j = 1 A g^{-1} (b).

6.3.3. Impedance spectroscopy data

6.3.3.1. EIS data for EDLCs in 1M $TEMABF_4$+AN

The impedance complex plane plots, i.e. Nyquist plots, for all the activated materials and 1M $TEMABF_4$+AN based EDLCs have been measured within the *ac* frequency range from 1 mHz to 300 kHz at fixed cell potentials from 0 to 3.4 V (Figs. 18 and 19). Figure 18a and Figure 19b indicate, that the Nyquist plot shape is nearly independent of the U applied, if $U \leq 3.2$ V. At higher cell potential values the low frequency part slowly starts to drift away from the ideal –90 degree slope. The Nyquist plot shows again the significant difference of the activated materials compared to the initial SiC-CDC 1100 (Fig. 18b). For all the CO_2 and steam activated SiC-CDC materials nearly ideal capacitive behavior can be observed. In the Nyquist plots mainly two different regions can be identified: 1) in the *ac* frequency range of from 300 Hz to 1 Hz with the nearly –45° slope is the so-called porous region, which is characteristic of the mass transfer limited process (with adsorption boundary conditions) in the micro/ mesoporous carbon electrode matrix; 2) at $f < 1$ Hz, the low frequency double-layer capacitance region with a slope of nearly –90° has been observed, which is caused by the finite length absorption effect. In case of more microporous materials, also a third region, expressed as a small semicircle, which can be observed at higher *ac* frequencies $f > 300$ Hz. This region is influenced by the adsorption kinetics of ions at the mesoporous areas of carbon electrode, on the series resistance of the materials and mass transfer resistance inside the porous carbon structure. In Figure 19b it can be seen that for the H_2-treated materials based EDLCs slightly lower high frequencies series resistance is obtained, which confirms the positive effect of the finishing H_2-treatment onto the ideal double layer formation kinetics.

The specific series capacitance values, C_m, calculated from the Nyquist plots at $U = 3.0$ V and $f = 1$ mHz, are shown in Table 4. The C_m values for the CO_2 activated materials were in the range of 108 to 125 F g^{-1} and for the steam activated materials from 123 to 141 F g^{-1}, whereas the initial SiC-CDC 1100 demonstrated only 40 F g^{-1}. Therefore, it can be concluded that the activation processes have increased the series capacitance to a great extent.

Figure 20 shows the phase angle φ vs. *ac* frequency dependencies. The phase angle values for both CO_2 (Fig. 20a) and steam activated materials (Fig. 20b) are in a similar range from –84° to –87°. A small drop in the phase angle values can be observed at low *ac* frequencies. This is probably caused by a small quantity of water residues and other electrochemically active components in the system.

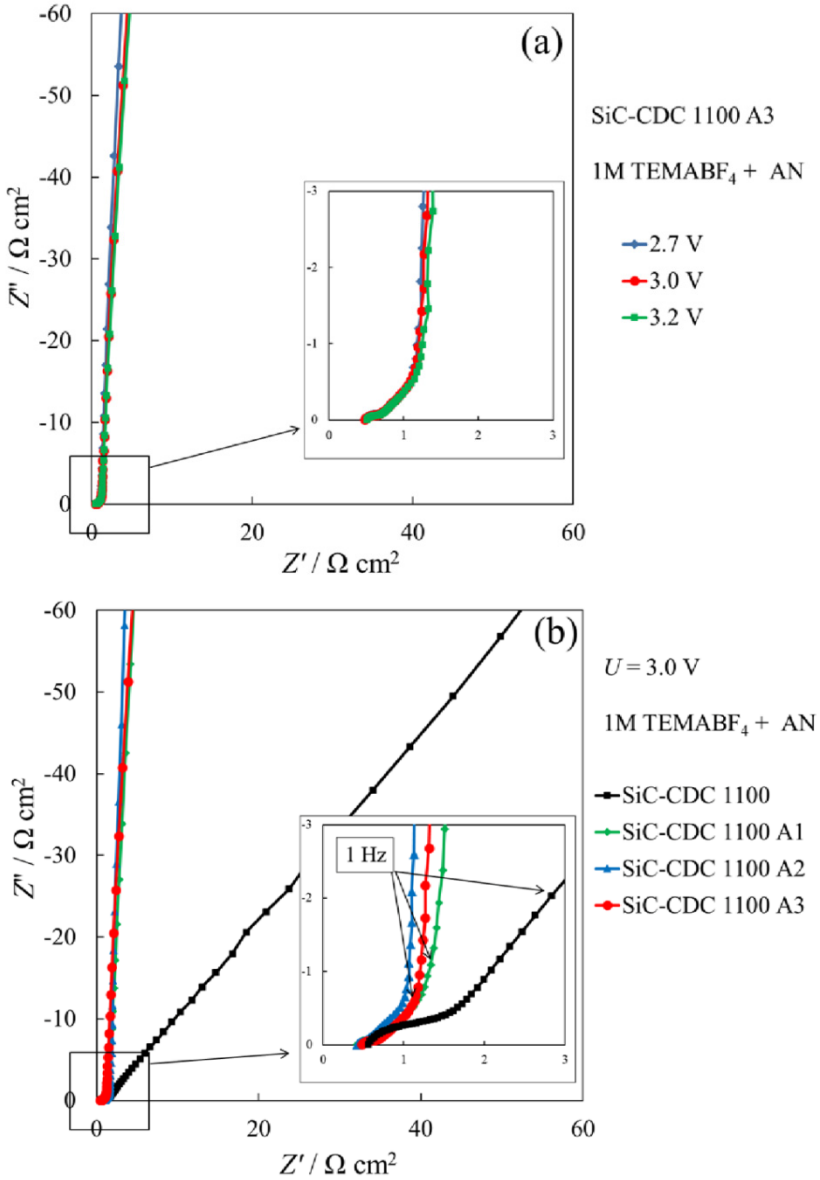

Figure 18. Nyquist plots of SiC-CDC 1100 A3 material at different cell potentials (a) and for the CO_2 activated materials at $U = 3.0$ V (b).

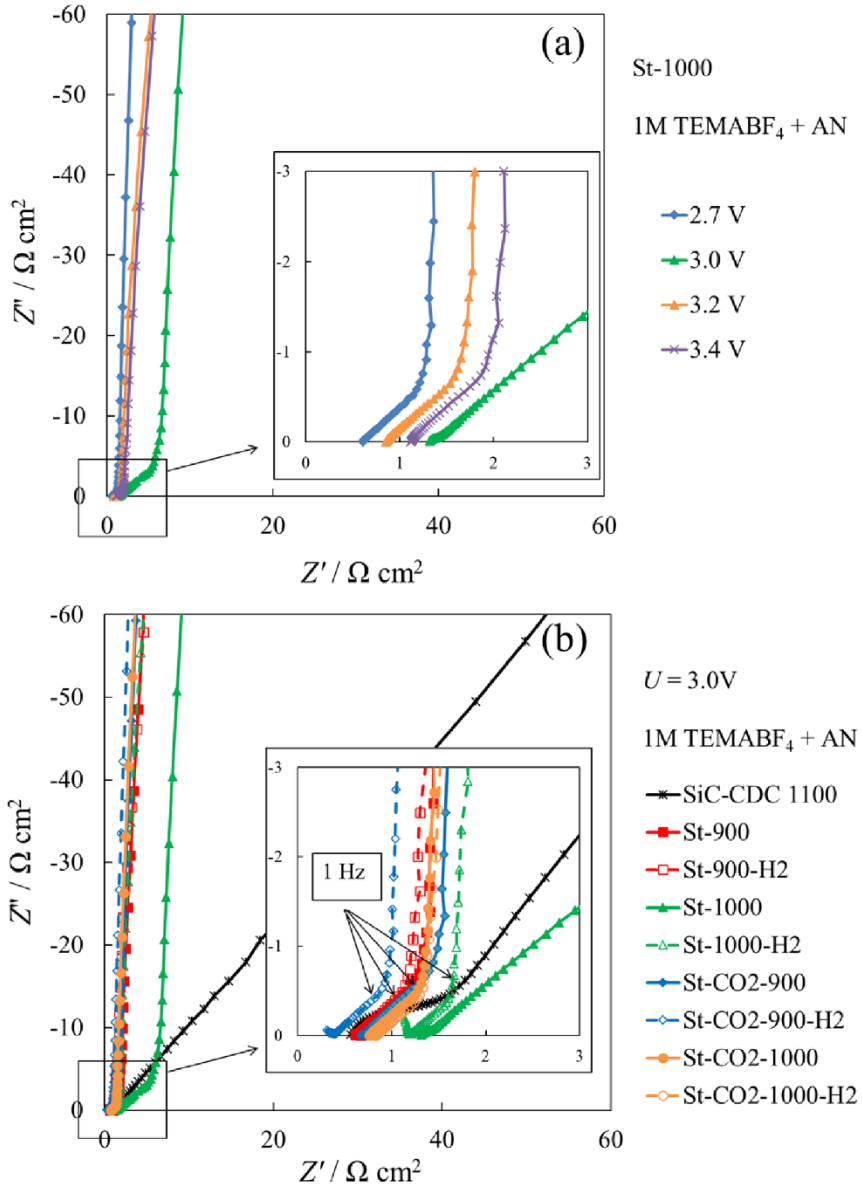

Figure 19. Nyquist plots of St-1000 material at different cell potentials (a) and for the steam activated materials at $U = 3.0$ V (b).

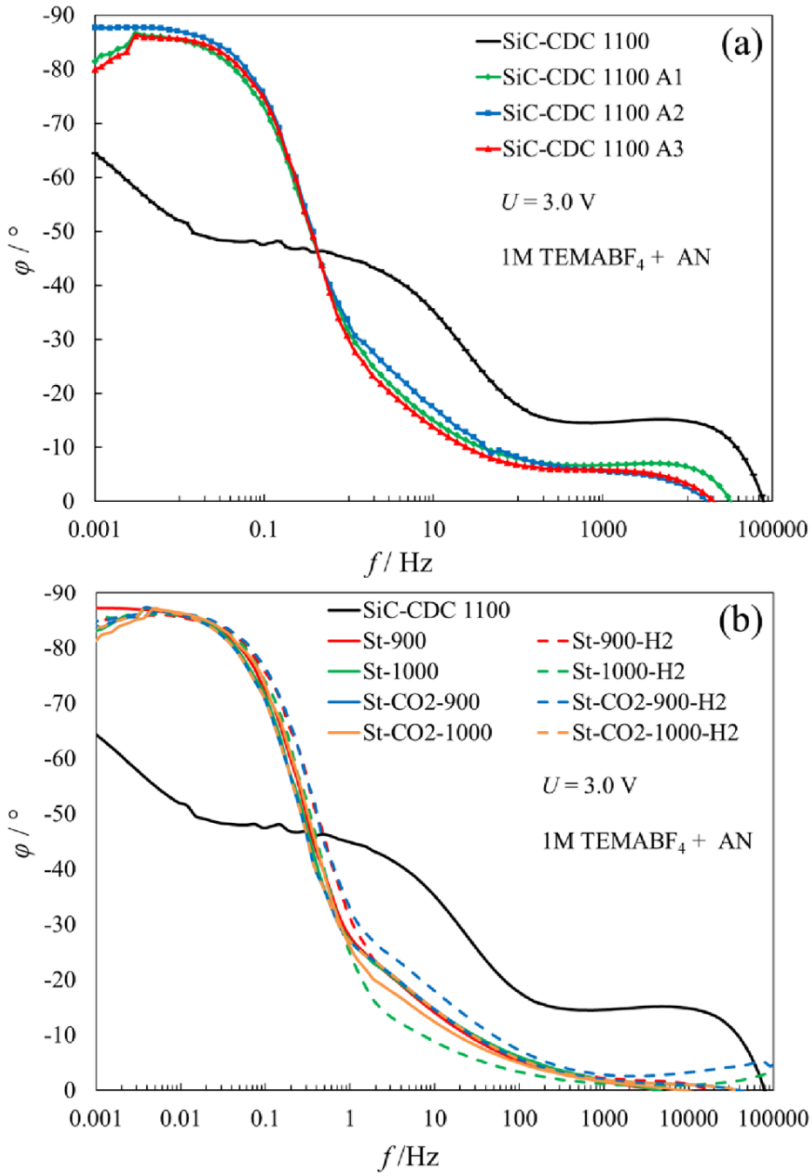

Figure 20. Phase angle vs. *ac* frequency dependencies for CO_2 activated material (a) and steam activated materials (b).

In an ideally polarizable system the ratio of $C_{m;p}/C_{m;s}$ should be 1. In Figure 21 it can be seen that in our experimental conditions all the activated materials demonstrated a long plateau and the $C_{m;p}/C_{m;s}$ ratio approaches 1. For all steam activated materials based EDLCs a bit more expressed deviation has been observed for than CO_2 activated materials.

The EDLC systems time constants τ_R were calculated according to Eq. 34 and are shown in Table 6. For $TEMABF_4$+AN based EDLCs the τ_R values for CO_2 activated materials were in the range from 0.53 to 0.59 s and for the steam activated materials based EDLCs from 0.37 to 0.53 s. Thus, very quick charging/discharging processes have been taken place.

Overall, it can be concluded, that in $TEMABF_4$+AN based EDLCs both CO_2 and steam activated SiC-CDC materials are suitable as electrode materials and there is only weak dependence of τ_R on materials characteristics (i.e. on activation conditions used).

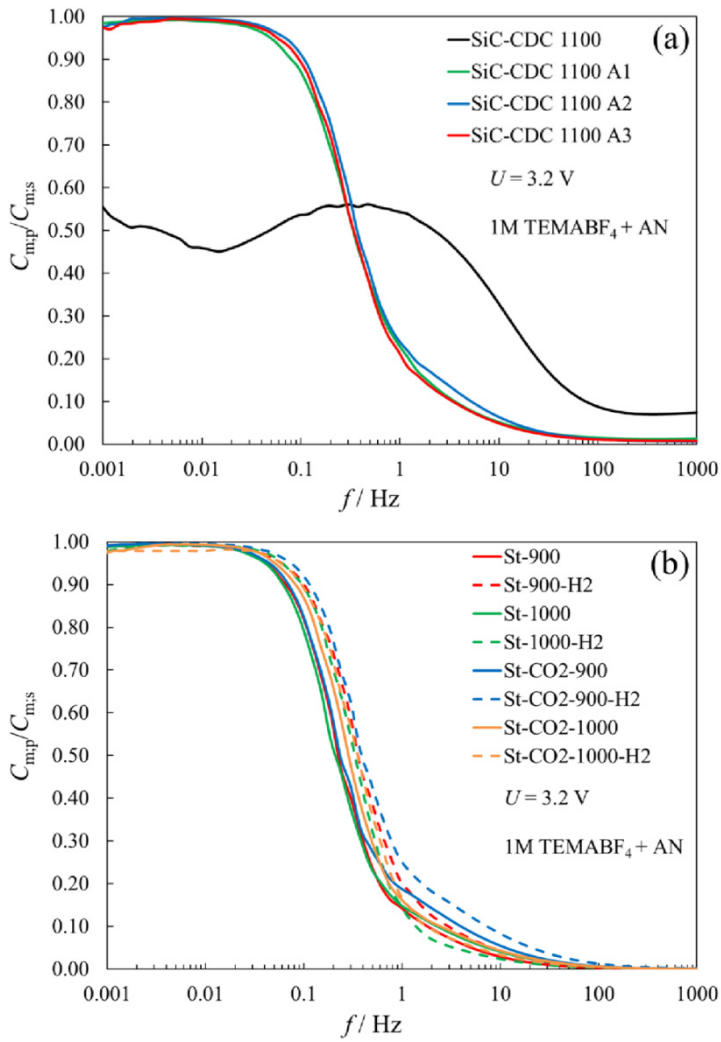

Figure 21. $C_{m;p}/C_{m;s}$ vs. *ac* frequency dependencies for CO_2 activated materials (a) and steam activated materials (b).

Table 6. Time constants at $U = 3.6$ V.

Abbreviation	1M $TEMABF_4$ + AN	$EMImBF_4$
SiC-CDC 1100 A1	0.59	26.6
SiC-CDC 1100 A2	0.53	10.6
SiC-CDC 1100 A3	0.55	13.3
St-900	0.51	2.66
St-900-H2	0.42	1.33
St-1000	0.53	3.35
St-1000-H2	0.42	1.05
St-CO2-900	0.55	8.41
St-CO2-900-H2	0.37	1.67
St-CO2-1000	0.44	1.68
St-CO2-1000-H2	0.41	1.69

6.3.3.2. EIS data for EDLCs in $EMImBF_4$

Nyquist plots have also been measured for EDLCs based on $EMImBF_4$ and all the studied activated materials. The initial SiC-CDC 1100 is not shown in this paragraph due to its nearly zero capacitance in $EMImBF_4$ based EDLC. The measurements were carried out in a *a*c frequency range from 1 mHz to 300 kHz at fixed cell potentials from 0 to 3.6 V or sometimes from 0 to 3.8 V. Figures 22a and 23a show how the shape of the Nyquist plot depends on the cell potential applied. The dependence is naturally somewhat influenced on the used materials characteristics, but the overall tendency is similar for all SiC-CDC materials, showing the Nyquist plot shape to be independent of the applied cell potential if $U \leq 3.2$ V. When higher U values are applied, the Nyquist plot shape slowly deviates from the ideal –90° slope at $f \rightarrow 0$. For steam activated materials the drift is overall somewhat smaller if compared with the CO_2 activated materials. Figures 22b and 23b show the Nyquist plots for all the studied materials. The similarities with previously described Nyquist plots for 1M $TEMABF_4$+AN based EDLCs are clear and same characteristic regions can be observed in the plots. For the CO_2 activated materials there are again the three regions: 1) small distorted semicircle can be seen, which depends on the adsorption kinetics and series resistance of electrolyte in meso/macropores; 2) the "porous" region with a –45° slope, characteristic of the mass transfer limited process within meso/micropores; 3) double-layer capacitance region, which in this case at $U = 3.6$ V is with a slope in within –70° to –80°.

For the steam activated materials, only two regions are observed and the first small semicircle region is not present. It can be explained by fact (BET data) that these materials have more bigger micropores and mesopores than the CO_2 activated materials. Also, it is observed that for the H_2-treated materials slightly lower resistance is obtained, which confirms the positive effect of the surface finishing by H_2-treatment.

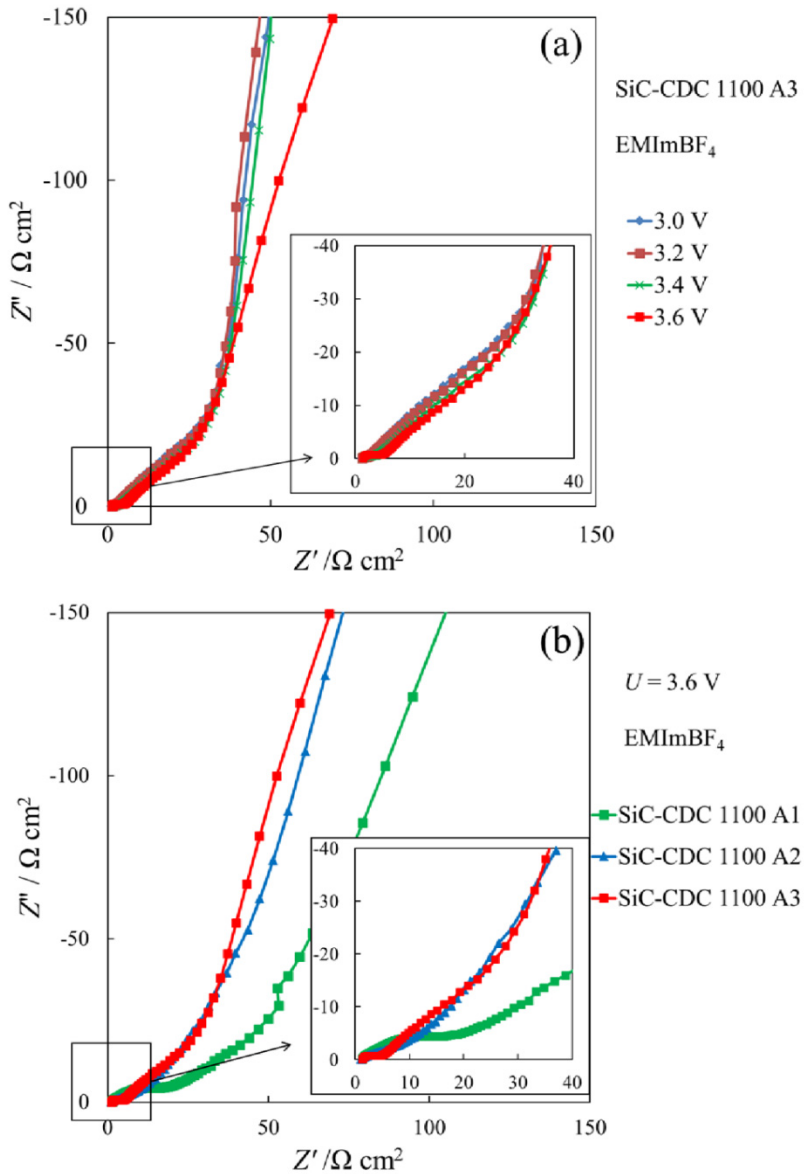

Figure 22. Nyquist plots of SiC-CDC 1100 A3 material at different cell potentials (a) and for the steam activated materials at $U = 3.6$ V (b).

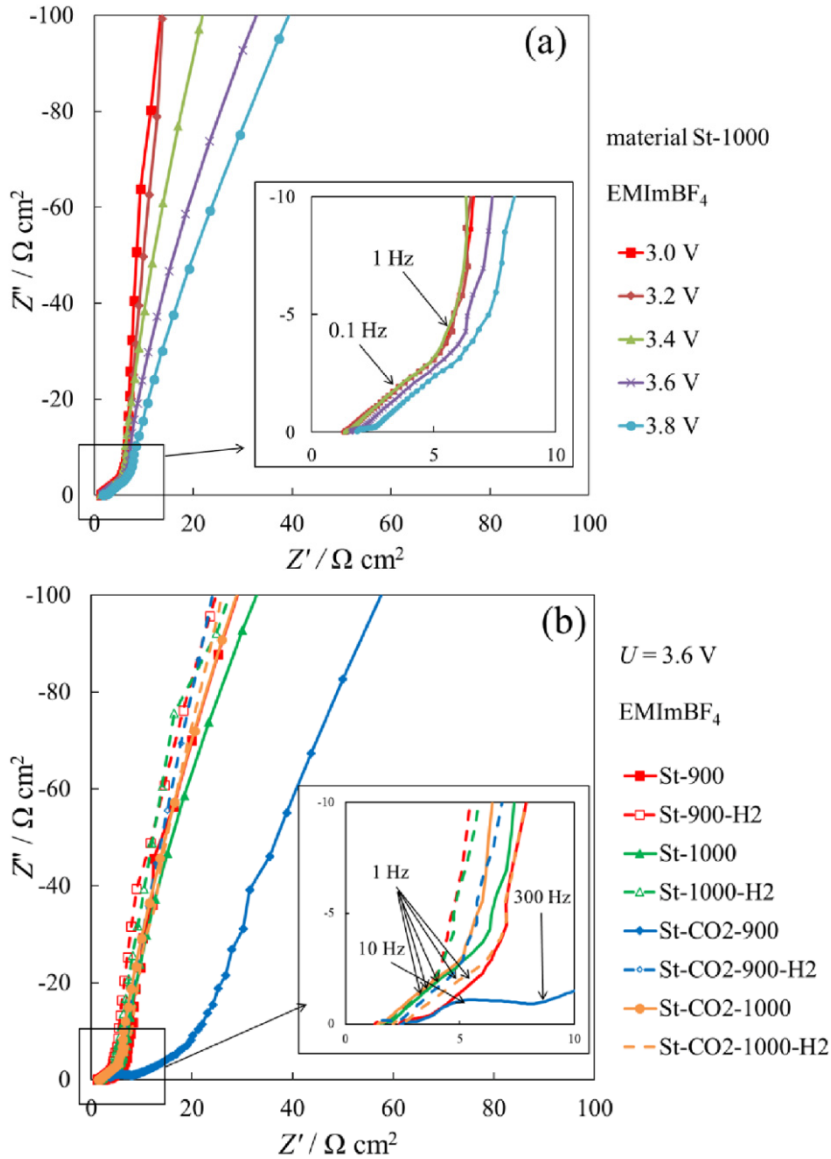

Figure 23. Nyquist plots of St-1000 material at different cell potentials (a) and for the steam activated materials at $U = 3.6$ V (b).

The specific series capacitance values C_m have been calculated from the EIS data and are shown in Table 5. The C_m values are in the range from 136 to 170 F g^{-1} for CO_2 activated materials and from 142 to 165 F g^{-1} for steam activated materials. Nevertheless, it has to be taken into account that sometimes the EIS method can overestimate the capacitance values, due to enhanced contribution of parasitic reactions to the electrochemical response in porous carbons.

The phase angle vs. *ac* frequency dependencies show that φ values are in the range of –60° to –70° for the CO_2 activated materials (Fig. 24a), whereas for the steam activated materials φ values are from –83° to –86°. At very low frequencies there are small plateaus in the φ vs. f plots. Three of the steam activated materials indicate similarities with the CO_2 activated materials results. Also, again the H_2 treated steam activated materials show higher φ values.

As already noted previously, in an ideally polarizable system the ratio of $C_{m;p}/C_{m;s}$ should be 1. In this case the CO_2 activated materials (Fig. 25a) do not show a plateau in the $C_{m;p}/C_{m;s}$ vs. f plots and the $C_{m;p}/C_{m;s}$ ratios are between 0.87 to 0.96. The steam activated materials all show a clear plateau in $C_{m;p}/C_{m;s}$ vs. f plots (except St-CO2-900, which has been brought out previously) and the ratios are very near to 1. Therefore, ideal capacitance values have been established for steam activated based EDLCs.

The characteristic time constant τ_R values (Table 6) very clearly indicate the difference between the differently activated materials. As for CO_2 activated materials based EDLCs, the obtained τ_R values are from 13.3 to 26.6 s, but for the steam activated materials the τ_R values vary from 1.05 to 8.41 s. Therefore, the steam activated materials based EDLCs allow to release the stored energy about 10 times faster than CO_2 activated materials based EDLCs.

Taking into account the results discussed, it can be concluded, that steam activated materials have better capacitive behavior when using a RTIL as electrolyte and thus in this case these materials should certainly be preferred for EDLC applications [94, 96].

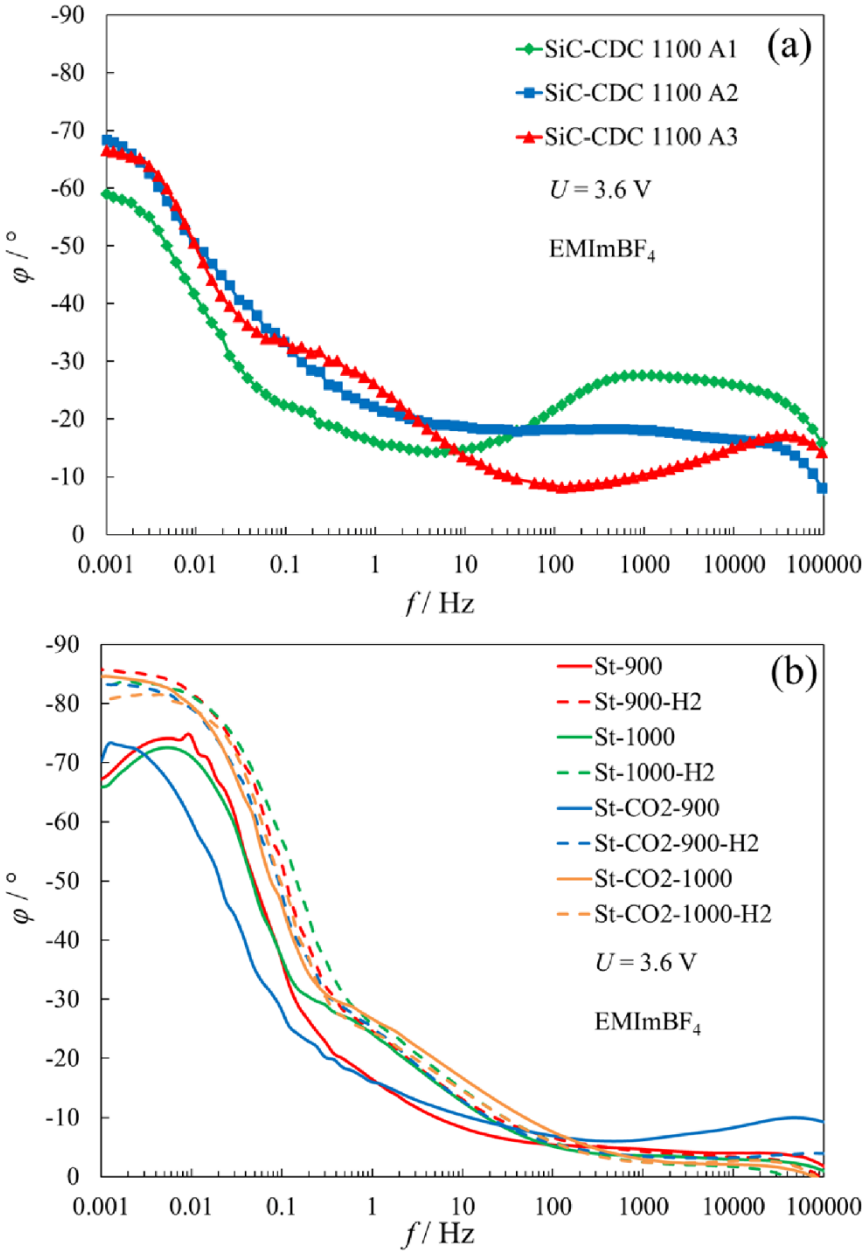

Figure 24. Phase angle vs. *ac* frequency dependencies for CO_2 activated material (a) and steam activated materials (b).

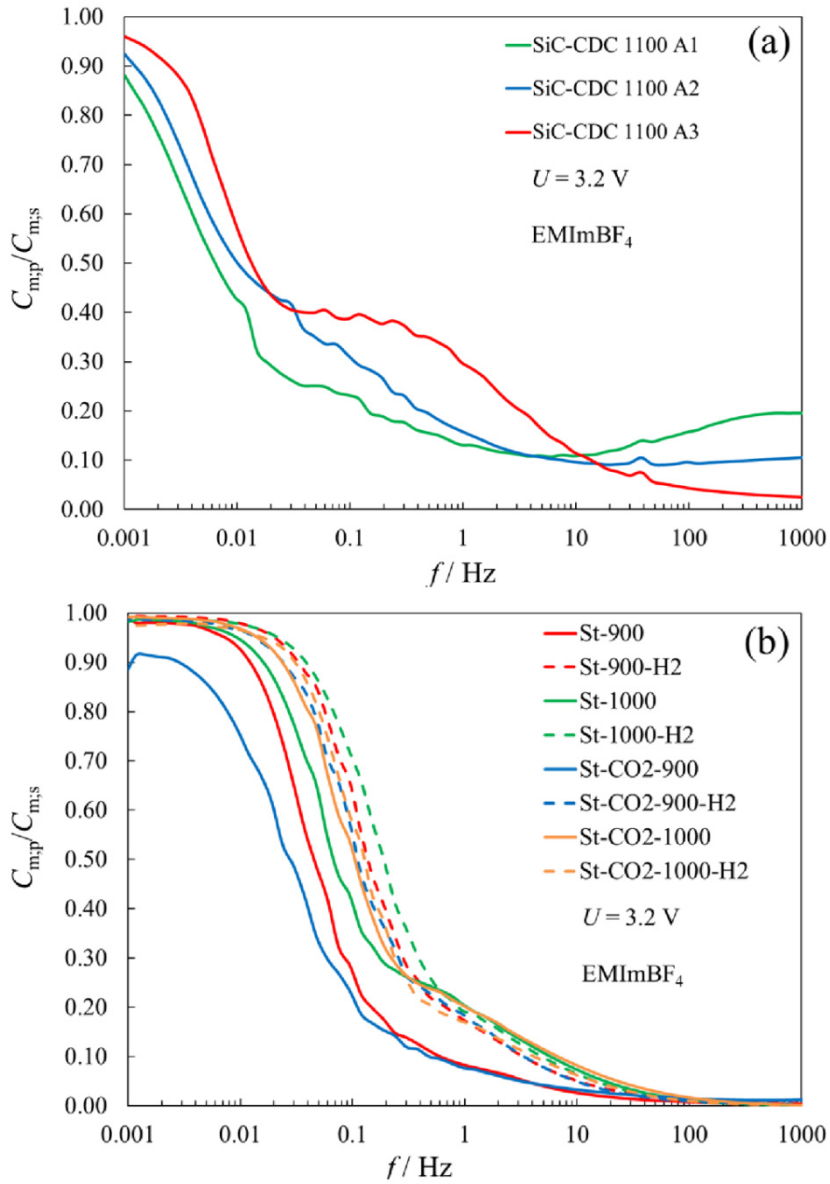

Figure 25. $C_{m;p}/C_{m;s}$ vs. *ac* frequency dependencies for CO_2 activated materials (a) and steam activated materials (b).

6.3.4. Constant power measurements data

Ragone plots (energy density E vs. power density P dependencies) are calculated from constant power tests in the cell potential range from 3.0 V to 1.5 V. The gravimetric Ragone plots for all the SiC-CDC activated materials and 1M $TEMABF_4$+AN based EDLCs are shown in Figure 26 and for $EMImBF_4$ based EDLCs in Figure 27. The corresponding volumetric Ragone plots are shown in Figure 28 and 29. The data is calculated to the total material weight, including active carbon electrode materials, the PTFE binder and Al current collectors. The active carbon makes up 90% of the total electrode weight.

The Ragone plots again confirm the benefits of the activation processes for SiC-CDC materials for energy storage applications. The CO_2 activated materials show increased energy densities up to $E \sim 27$ Wh kg^{-1} at $P = 1$ kW kg^{-1} ($E \sim 16$ Wh dm^{-3} at $P = 1$ kW dm^{-3}, Fig. 28a) and $E \sim 23$ Wh kg^{-1} at $P = 10$ kW kg^{-1} ($E \sim 12$ Wh dm^{-3} at $P = 10$ kW dm^{-3}, Fig. 28a), whereas the initial SiC-CDC 1100 shows very low values ~10 Wh kg^{-1} (~ 7 Wh dm^{-3}, Fig. 28a) and ~ 2 Wh kg^{-1} (~ 1 Wh dm^{-3}, Fig. 28a), correspondingly (Fig. 26a). The steam activated materials show very similar E values and differ only a little from each other, having E values from 30 to 35 Wh kg^{-1} at $P = 1$ kW kg^{-1} (E up to 18 Wh dm^{-3} at $P = 1$ kW dm^{-3}, Fig. 28b) and from 20 to 27 Wh kg^{-1} at $P = 10$ kW kg^{-1} (Fig. 26b) (E up to 13 Wh dm^{-3} at $P = 10$ kW dm^{-3}, Fig. 28b).

In case of RTIL based EDLC, the CO_2 activated materials (Fig. 27a) have E values from 13 to 25 Wh kg^{-1} at $P = 1$ kW kg^{-1} (~ 15 Wh dm^{-3}, respectively, Fig. 29a) and only from 0.3 to 3.5 Wh kg^{-1} at $P = 10$ kW kg^{-1} (~ 2 Wh dm^{-3}, respectively, Fig. 29a). At the same time the steam activated materials (Fig. 27b) demonstrated E values from 24 to 37 Wh kg^{-1} at $P = 1$ kW kg^{-1} (~ 26Wh dm^{-3}, respectively, Fig. 29b) and from 5 to 15.7 Wh kg^{-1} at $P = 10$ kW kg^{-1} (~ 11 Wh dm^{-3}, respectively, Fig. 29b). Therefore, steam activated materials based EDLCs show in case of both electrolytes higher energy and power densities, but there is only a slight difference between steam and steam-CO_2 co-activated materials.

Some increase of power densities depending on the increase of activation extent can be explained by the creation of larger pores during the activation process, which in turn reduces the mass-transfer resistance. Due to wide micro-mesopores, the ions can move faster in the porous electrode matrix and thus the energy stored in the system can be released more quickly, generating higher power [93–96].

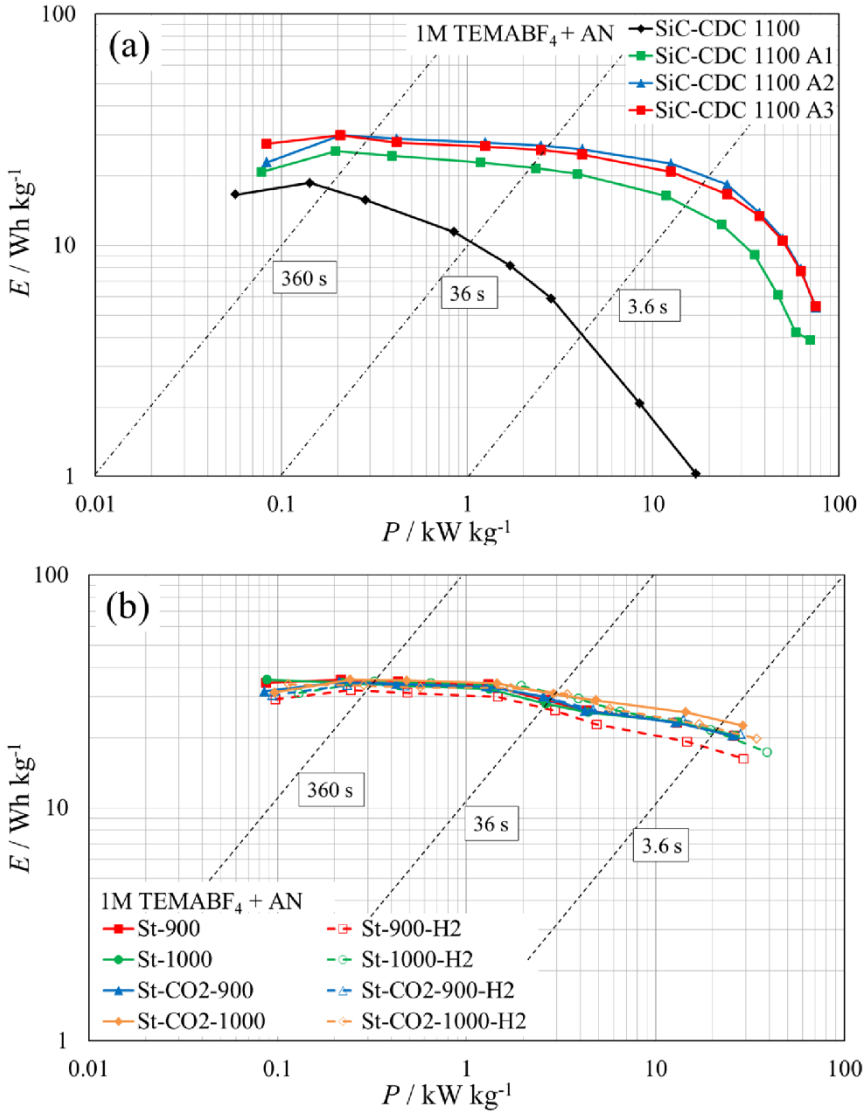

Figure 26. Gravimetric Ragone plots for CO_2 activated materials (a) and steam activated materials (b) based EDLCs in 1M $TEMABF_4$+AN.

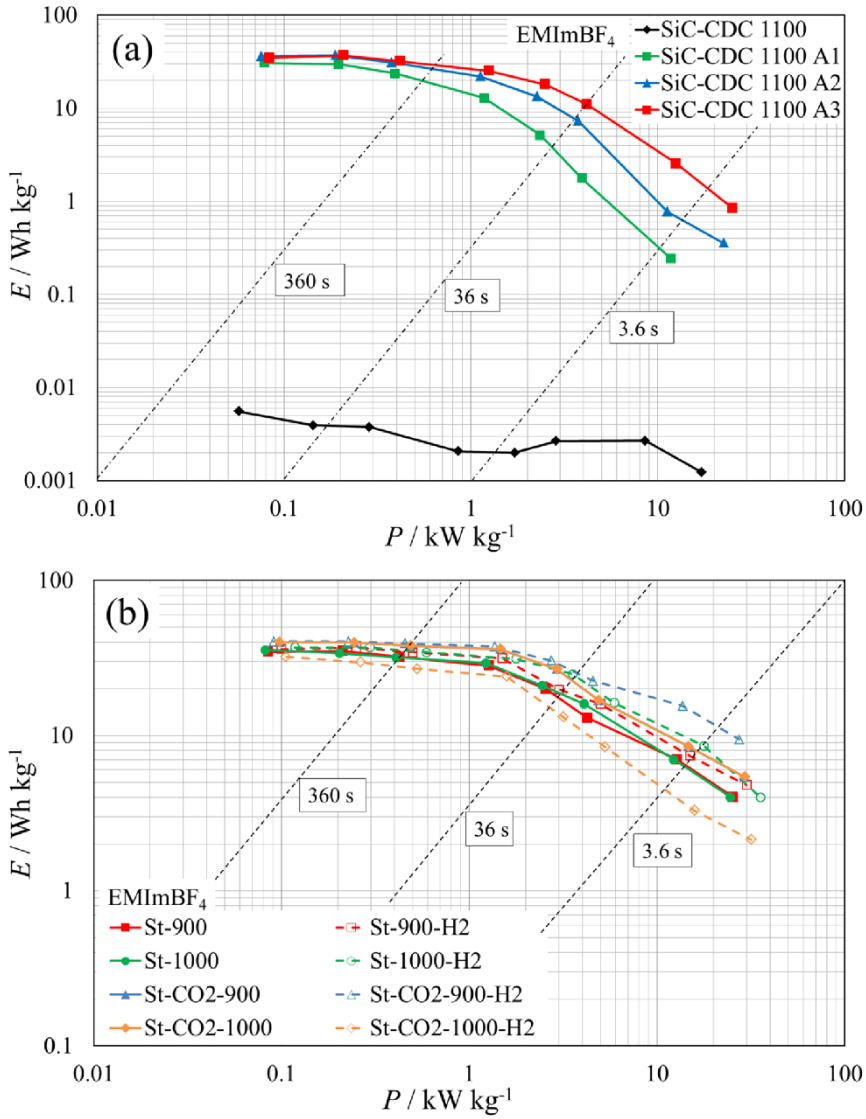

Figure 27. Gravimetric Ragone plots for CO_2 activated materials (a) and steam activated materials (b) based EDLCs in $EMImBF_4$.

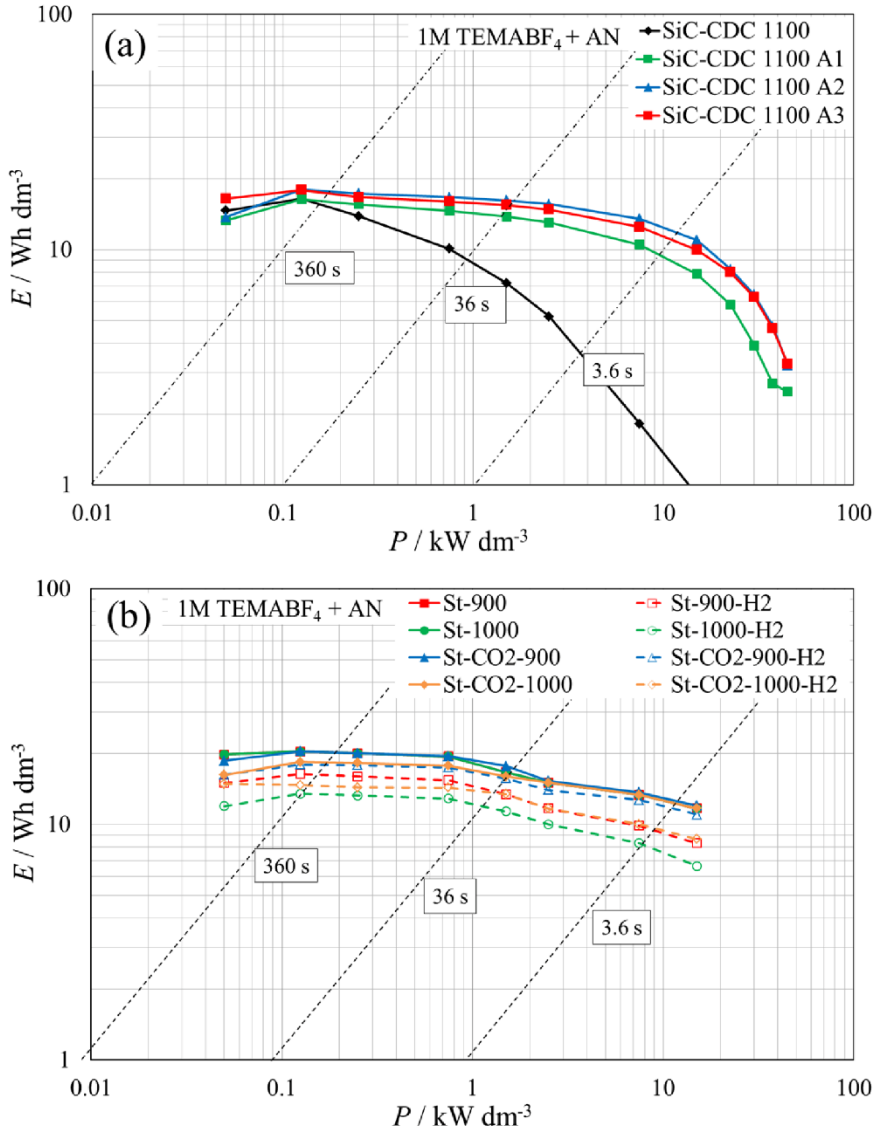

Figure 28. Volumetric Ragone plots for CO_2 activated materials (a) and steam activated materials (b) based EDLCs in 1M $TEMABF_4$+AN.

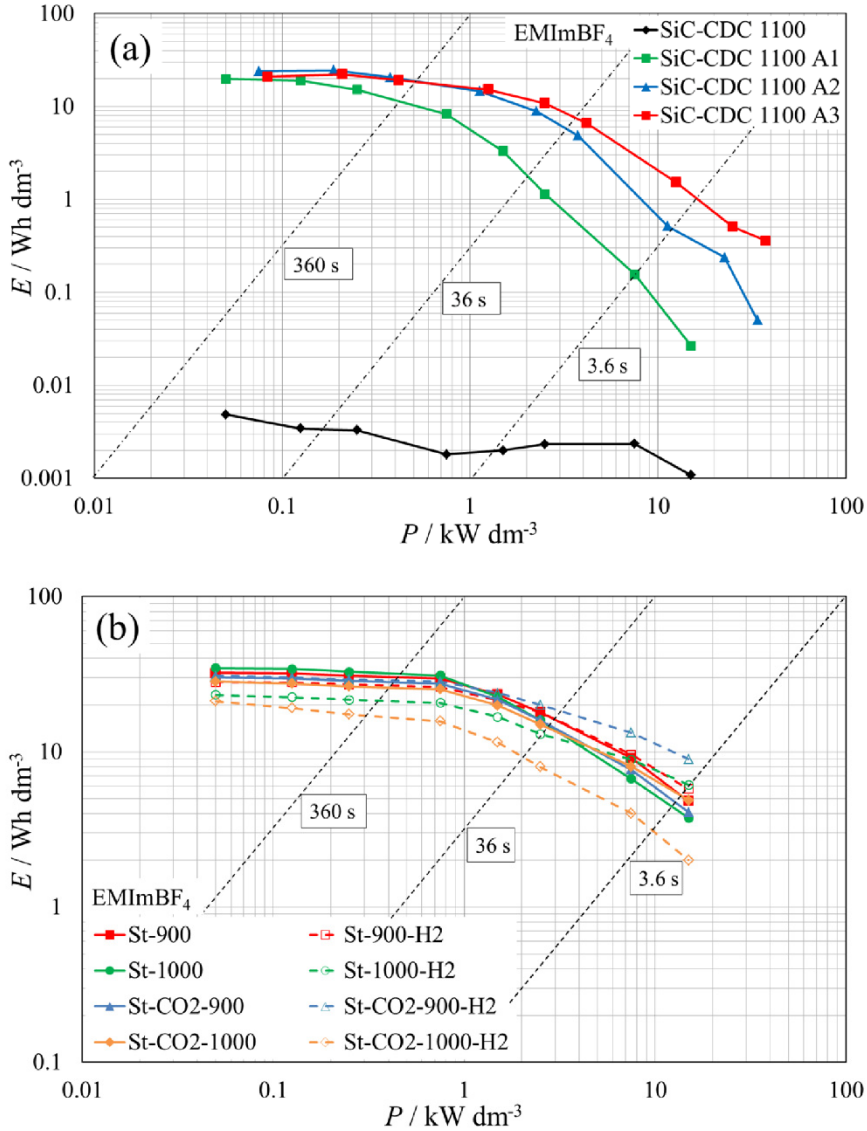

Figure 29. Volumetric Ragone plots for CO_2 activated materials (a) and steam activated materials (b) based EDLCs in $EMImBF_4$.

6.3.5. Lifetime test results

Lifetime test was carried out for St-CO2-1000 material and $EMImBF_4$ electrolyte based EDLC. The test was done by CC/CD method for 5000 cycles at constant current density j = 1 A g^{-1} between cell potentials from 1.5 to 3.0 V (Fig. 30). The capacitance values decrease from 140 F g^{-1} to 107 F g^{-1} by the end of 5000th cycle. At the same time, the CC/CD curves (Fig. 30, inset) still show practically linear shape even after the 5000 cycles. The IR-drop was nearly constant up to 2000th cycle, after which it started to increase very slowly. After 5000 cycles the energy efficiencies dropped only from 96% to 94%, whereas the coulombic efficiencies remained in the range of 97–99% during the all cycling period. Therefore, the lifetime test confirmed the previously discussed results, which suggest that steam activated SiC-CDC materials are suitable for various high energy storage applications [96].

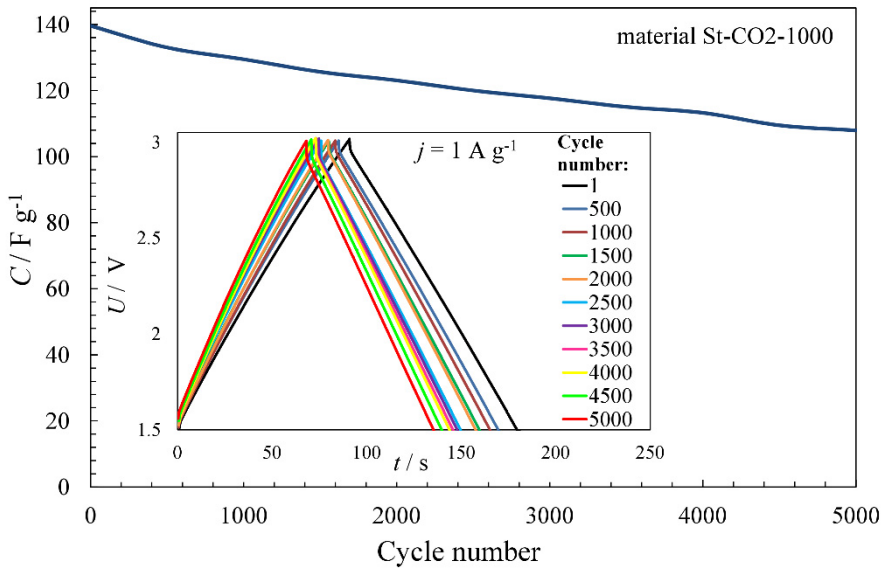

Figure 30. Capacitance vs. cycle number dependency and lifetime test charge/discharge cycles.

SUMMARY

The main aim of this study was to analyze the influence of the synthesis and activation parameters on the SiC-CDC materials physical and electrochemical characteristics and therefore find the optimal combination of carbon powder treatment parameters.

The SiC-CDC materials were synthesized via chlorination from SiC and thereafter activated at different temperatures and activation times with CO_2, steam or steam and CO_2 mixture. For detailed characterization of the materials synthesized, different methods were used: X-ray diffraction, Raman spectroscopy, transmission electron microscopy, low-temperature N_2 (for some materials also Ar and CO_2) sorption and different electrochemical measurement methods.

It was found that the synthesis and activation temperature influenced the carbon oxidation reaction rate and there is a clear correlation between the extent of the burn-off during activation and the porosity parameters of the materials prepared. This in turn has significant influence on the electrochemical properties. The physical characterization tests confirmed that the materials are mainly amorphous, with a small content of graphitic layers. During the activation processes the porous carbon structure did not change significantly. Sorption measurements data showed that with the increase of the burn-off of amorphous carbon areas, the mesoporosity increased and microporosity somewhat decreased. Also, the total pore volume and average pore width of micro-mesoporous carbon pores increased. Therefore, based on the physical characterization it can be concluded that the burn-off during the activation takes place preferably from the carbon materials amorphous parts.

The SiC-CDC activated materials based EDLCs showed in 1M $TEMABF_4$ + AN nearly ideal capacitive behavior and excellent coulombic efficiency of 98–99%. The achieved capacitance values were more than two-times higher than for the initial non-activated SiC-CDC 1100. Also, energy and power densities increased more than 40% as a result of the activation step. For $EMImBF_4$ based EDLCs the steam activated materials had somewhat better capacitive behavior and higher negative phase angle values. This is due to their higher mesoporosity and increased content of the bigger micropores, compared to the CO_2 activated materials. With RTIL electrolyte the initial SiC-CDC 1100 material based EDLC had almost no capacitive behavior.

However, for both activation methods applied the results of this study show minimal change in the macrostructure of carbon materials, but significant increase in specific surface area, pore volume and pore widths, thus in meso- and micropores scale. These changes in turn have a strong impact on the SiC-CDC electrochemical characteristics. Due to that, with simple and cheap activation methods (CO_2, H_2O and combined CO_2+H_2O methods) it is possible to synthesize micro-mesoporous hierarchical SiC-CDC materials, demonstrating comparable electrochemical characteristics to other carbide derived carbons, but

being greatly cheaper. Steam activation is somewhat more efficient, less time consuming and results in materials with more expressed capacitive behavior in different electrolytes ($TEMABF_4$ + AN, $EMImBF_4$). Therefore, the H_2O as the activation agent should be preferred to the CO_2 activation for synthesis of electrode materials for high power and energy density non-aqueous electrolyte based EDLCs.

REFERENCES

1. J. Pallarés, A. González-Cencerrado, I. Arauzo, Biomass Bioenergy 115 (2018) 64–73.
2. H. Marsh, F. Rodriguez-Reinoso, Activated Carbon, Elsevier, Oxford, 2006.
3. R. Härmas, R. Palm, M. Härmas, M. Pohl, H. Kurig, I. Tallo, E. Tee, I. Vaas, R. Väli, T. Romann, O. Oll, R. Kanarbik, K. Liivand, J. Eskusson, J. Kruusma, T. Thomberg, A. Jänes, P. Miidla, E. Lust, Electrochim. Acta 283 (2018) 931–948.
4. T. Zhang, W. P. Walawender, L. T. Fan, M. Fan, D. Daugaard, R. C. Brown, Chem. Eng. J. 105 (2004) 53–59.
5. W. Su, L. Zhou, Y. Zhou, Chinese J. Chem. Eng. 14 (2) (2006) 266–269.
6. J. F. Gonzalez, S. Roman, J. M. Encinar, G. Martinez, J. Anal. Appl. Pyrol. 85 (2009) 134–141.
7. P. Guo, Y, Gu, Z. Lei, Y. Cui, X. S. Zhao, Micropor. Mesopor. Mat. 156 (2012) 176–180.
8. Y. Gao, Q. Yue, B. Gao, Y. Sun, W. Wang, Q. Li, Y. Wang, Chem. Eng. J. 217 (2013) 345–353.
9. Y-J, Zhang, Z-J, Xing, Z-K. Duan, M. Li, Y. Wang, Appl. Surf. Sci. 315 (2014) 279–286.
10. I. Tallo, T. Thomberg, K. Kontturi, A. Jänes, E. Lust, Carbon 49 (13) (2011) 4427–4433.
11. I. Tallo, T. Thomberg, H. Kurig, K. Kontturi, A. Jänes, E. Lust, Carbon 67 (2014) 607–616.
12. E. Lust, K. Vaarmets, J. Nerut, I. Tallo, P. Valk, S. Sepp, E. Härk, Electrochim. Acta 140 (2014) 294–303.
13. T. Tooming, T. Thomberg, H. Kurig, A. Jänes, E. Lust, J. Power Sources 280 (2015) 667–677.
14. T. Thomberg, A. Jänes, E. Lust, J. Electroanal. Chem. 630 (2009) 55–62.
15. T. Thomberg, A. Jänes, E. Lust, Electrochim. Acta 55 (2010) 3138–3143.
16. E. Lust, A. Jänes, M. Arulepp, J. Electroanal. Chem. 562 (2004) 33–42.
17. A. Jänes, H. Kurig, E. Lust, Carbon 45 (2007) 1226–1233.
18. J. Eskusson, A. Jänes, A. Kikas, L. Matisen, E. Lust, J. Power Sources 196 (2011) 4109–4116.
19. K. Tõnurist, A. Jänes, T. Thomberg, H. Kurig, E. Lust, J. Electrochem. Soc. 156 (4) (2009) A334–A342.
20. K. Tõnurist, T. Thomberg, A. Jänes, T. Romann, V. Sammelselg, E. Lust, J. Electroanal. Chem. 689 (2013) 8–20.
21. A. Laheäär, A. Jänes, E. Lust, Electrochim. Acta 56 (2011) 9048–9055.
22. H. Kurig, A. Jänes, E. Lust, J. Electrochem. Soc. 157 (3) (2010) A272–A279.
23. H. Kurig, T. Romann, A. Jänes, E. Lust, ECS Trans. 25 (23) (2010) 15–23.
24. H. Kurig, M. Vestli, K. Tõnurist, A. Jänes, E. Lust, J. Electrochem. Soc. 159 (7) (2012) A944–A951.
25. M. T. Kartel, N. V. Sych, M. M. Tsyba, V. V. Strelko, Carbon 44 (2006) 1013–1024.
26. T. J. Bandosz, Activated Carbon Surfaces in Environmental Remediation, Elsevier, Oxford, 2006.
27. R. K. Dash, G. Yushin, Y. Gogotsi, Micropor. Mesopor. Mat. 86 (2005) 50–57.
28. T. Morishita, Y. Soneda, T. Tsumura, M. Inagaki, Carbon 44 (2006) 2360–2367.

29. Y. Zhao, W. Wang, D. B. Xiong, G. Shao, W. Xia, S. Yu, F. Gao, Int. J. Hydrogen. Energ. 37 (24) (2012) 19395–19400.
30. H. Jin, R. Zhang, Q. Liu, Mater. Lett. 64 (2010) 1019–1021.
31. G. N. Yushin, E. N. Hoffman, A. Nikitin, H. Ye, M. W. Barsoum, Y. Gogotsi, Carbon 43 (2005) 2075–2082.
32. C. Vix-Guterl, E. Franckowiak, K. Jurewicz, M. Friebe, J. Parmentier, F. Beguin, Carbon 43 (2005) 1293–1302.
33. B. Lobato, L. Suárez. L. Guardia, T.A. Centeno, Carbon 122 (2017) 434–445.
34. Y. Gogotsi, Nanomaterials Handbook, CRC Taylor & Francis, Boca Raton, 2009.
35. V. Presser, M. Heon, Y. Gogotsi, Adv. Funct. Mater. 21 (2011) 810–833.
36. A. Nikitin, Y. Gogotsi, Encyclopedia of Nanoscience and Nanotechnology 7 (2004) 553–574.
37. S. Osswald, C. Portet, Y, Gogotsi, G. Laudisio, J. P. Singer, J. E. Fischer, V. V. Sokolov, J. A. Kukushkina, A. E. Kravchik, J. Solid State Chem. 182 (2009) 1733–1741.
38. E. Frackowiak, Q. Abbas, F. Beguin, J. Energy. Chem. 22 (2013) 226–240.
39. X. Zhang, H. Zhang, C. Li, K. Wang, X. Sun, Y. Ma, RSC Adv. 4 (2014) 45862–45884.
40. S. Faraji, F. N. Ani, Renew. Sust. Energ. Rev. 42 (2015) 823–834.
41. R. Kötz, M. Carlen, Electrochim. Acta 45 (2000) 2483–2498.
42. F. Beguin, E. Frackowiak, Supercapacitors: Materials, Systems and Applications, Wiley, Singapore, 2013.
43. A. G. Pandolfo, A. F. Hollenkamp, J. Power Sources 157 (2006) 11–27.
44. L. Wei, G. Yushin, J. Power Sources 196 (2011) 4072–4079.
45. B. E. Conway, Electrochemical Supercapacitors: Scientific Fundamentals and Technological Applications, Kluwer Academic/Plenum, New York, 1999.
46. F. Beguin, V. Presser, A. Balducci, E. Frackowiak, Adv. Mater. 26 (2014) 2219–2251.
47. Z-Y. Li, M.S. Akhtar, D-H. Kwak, O-B. Yang, Appl. Surf. Sci. 404 (2017) 88–93.
48. V.S. Bagotsky, Fundamentals of Electrochemistry, Wiley, New Jersey, 2006.
49. Y. Zhang, H. Feng, X. Wu, L. Wang, A. Zhang, T. Xia, H. Dong, X. Li, L. Zhang, Int. J. Hydrogen. Energ. 34 (2009) 4889–4899.
50. A. Burke, J. Power Sources 91 (2000) 37–50.
51. A. Burke,. Electrochim. Acta 53 (2007) 1083–1091.
52. A. Lewandowski, M. Galinski, J. Power Sources 173 (2007) 822–828.
53. E. Frackowiak, F. Beguin, Carbon 39 (2001) 937–950.
54. C. M. A. Brett, A. M. O. Brett, Electrochemistry: Principles, Methods and Applications, Oxford University Press, Oxford, 1993.
55. J. Wang, Analytical Electrochemistry, VCH Publishers, New York, 1994.
56. M. Kormann, N. Popovska, Micropor. Mesopor. Mat. 130 (2010) 167–173.
57. S. Welz, M. J. McNallan, Y. Gogotsi, J. Mater. Process. Tech. 179 (2006) 11–12.
58. B. Rufino, S. Mazerat, M. Couvrat, C. Lorrette, H. Maskrot, R. Pailler, Carbon 49 (2011) 3073–3083.
59. B. Basavalingu, J. M. Calderon Moreno, K. Byrappa, Y. G. Gogotsi, M. Yoshimura, Carbon 39 (2001) 1763–1767.
60. C. F. Chang, C. Y. Chang, W. T. Tsai, J. Colloid Interf. Sci. 232 (2000) 45–49.
61. Z. Hu, M. P. Srinivasan, Micropor. Mesopor. Mat. 27 (1999) 11–18.
62. M. J. Bleda-Martinez, J. A. Macia-Agullo, D. Lozano-Castello, E. Morallon, D. Cazorla-Amoros, A. Linares-Solano, Carbon 43 (2005) 2677–2684.

63. K. Okada, N. Yamamoto, Y. Kameshima, A. Yasumori, J. Colloid Interf. Sci. 262 (2003) 179–193.
64. M. Molina-Sabio, M.T. González, F. Rodriguez-Reinoso, A. Sepúlveda-Escribano, Carbon 34 (1996) 505–509.
65. J. A. Macia-Agullo, B. C. Moore, D. Cazorla-Amoros, A. Linares-Solano, Carbon 42 (2004) 1367–1370.
66. S. Lowell, J. E. Shields, M. A. Thomas, M. Thommes, Characterization of Porous Solids and Powders: Surface Area, Pore Size and Density, Springer, Dordrecht, 2006.
67. J. B. Condon, Surface Area and Porosity Determinations by Physisorption, Elsevier, Oxford, 2006.
68. P. A. Webb, C. Orr, Analytical Methods in Fine Particle Technology. Micromeritics Instrument Corporation, Norcross, 1997.
69. J. Jagiello, Langmuir 10 (1994) 2778–2785.
70. J. Jagiello, J. P. Olivier, Adsorption 19 (2013) 777–783.
71. NLDFT Analysis by SAIEUS program http://www.nldft.com/ (accessed 30.05.19)
72. H. P. Klug, L. E. Alexander, X-Ray Diffraction Procedures: For Polycrystalline and Amorphous Materials. Wiley, New York, 1974.
73. G. A. Zickler, B. Smarsly, N. Gierlinger, H. Peterlik, O. Paris, Carbon 44 (2006) 3239–3246.
74. A. Sharma, T. Kyotani, A. Tomita, Carbon 38 (2000) 1977–1984.
75. M. Inagaki, New Carbons – Control of Structure and Functions, Elsevier, Amsterdam, 2000.
76. D. Roy, M. Chhowalla, H. Wang, N. Sano, I. Alexandrou, T. W. Clyne, G. A. J. Amaratunga, Chem. Phys. Lett. 373 (2003) 52–56.
77. S. Urbonaite, L. Hälldahl, G. Svensson, Carbon 46 (2008) 1942–1947.
78. A. C. Ferrari, J. Robertson, Phys. Rev. B 61 (2000) 14095–14107.
79. A. Cuesta, P. Dhamelincourt, J. Laureyns, A. Martinez-Alonso, J. M. D. Tascon, Carbon 32 (1994) 1523–1532.
80. A. C. Ferrari, B. Kleinsorge, G. Adamopoulos, J. Robertson, W. I. Milne, V. Stolojan, L. M. Brown, A. LiBassi, B. K. Tanner, J. Non-Cryst. Solids 266-269 (2000) 765–768.
81. P. Delhaes, M. Couzi, M. Trinquecoste, J. Dentzer, H. Hamidou, C. Vix-Guterl, Carbon 44 (2006) 3005–3013.
82. S. J. Yoo, C.-Y. Kim, J. W. Shin, S.-G. Lee, J.-M. Jeong, Y.-J. Kim, S.-H. Lee, J.-G. Kim, Characterization of an Amorphous Carbon Film Covering a Mo Grid During in Situ Heating TEM Study. Mater. Charact. 78 (2013) 31–36.
83. H. Schultrich, B. Schultrich, Ultramicroscopy 88 (2011) 111–125.
84. R. F. Egerton, Physical Principles of Electron Microscopy. Springer, New York, 2007.
85. B. Fultz, J. M. Howe, Transmission Electron Microscopy and Diffractometry of Materials. Springer, Berlin Heidelberg, 2008.
86. P. E. J. Flewitt, R. K. Wild, Physical Methods for Materials Characterisation. IOP Publishing Ltd, London, 2003.
87. A. Laheäär, P. Przygocki, Q. Abbas, F. Béguin, Electrochem. Commun. 60 (2015) 21–25.
88. P. I. Taberna, P. Simon, J. F. Fauvarque, J. Electrochem. Soc. 150 (2003) A292–A300.

89. H. H. Girault, Analytical and Physical Electrochemistry. EPFL Press, Lausanne, 2004.
90. E. Barsoukov, J. R. Macdonald, Impedance Spectroscopy Theory, Experiment and Applications, Wiley, New Jersey, 2005.
91. T. Thomberg, T. Tooming, T. Romann, R. Palm, A. Jänes, E. Lust, J. Electrochem. Soc. 160 (2013) A1834–A1841.
92. L. Wei, G. Yushin, Carbon 49 (2011) 4830–4838.
93. E. Tee, I. Tallo, H. Kurig, T. Thomberg, A. Jänes, E. Lust, Electrochim. Acta 161 (2015) 364–370.
94. E. Tee, I. Tallo, T. Thomberg, A. Jänes, E. Lust, J. Electrochem. Soc. 163 (7) (2016) A1317–A1325.
95. E. Tee, I. Tallo, T. Thomberg, A. Jänes, E. Lust, J. Electrochem. Soc. 165 (10) (2018) A2357–A2364.
96. E. Tee, I. Tallo, T. Thomberg, A. Jänes, E. Lust, J. Electrochem. Soc. 166 (8) (2019) A1558–A1567.

SUMMARY IN ESTONIAN

„Mikro- ja mesopoorsete hierarhilise struktuuriga süsinike sünteesimeetodite arendamine ja materjalide karakteriseerimine“

Antud uurimustöö põhieesmärgiks oli analüüsida sünteesi ja aktveerimise protsesside parameetrite mõju SiC-CDC materjalide füüsikalistele ja elektrokeemilistele omadustele ning leida optimaalsed materjalide töötlemisparameetrid.

SiC-CDC materjalid sünteesiti kloreerimise teel ränikarbiidist ja seejärel aktiveeriti erinevatel temperatuuridel CO_2, veeauru või veeauru ja CO_2 koosaktiveerimise meetoditega. Sünteesitud materjalide detailseks karakteriseerimiseks kasutati erinevaid meetodeid: röntgendifraktsioon, Raman spektroskoopia, läbivkiirguse elektronmikroskoopiat, madaltemperatuurse lämmastiku (osade materjalide puhul ka argoon ning süsinikdioksiid) sorptsiooni mõõtmisi ning erinevaid elektrokeemilisi mõõtmismeetodeid.

Tulemustest selgub, et sünteesi ja aktiveerimistemperatuur mõjutasid reaktsiooni kulgemise kiirust ning on selge seos toimuva massikao ja materjalide poorsuse karakteristikute vahel. See omakorda mõjutab oluliselt elektrokeemilisi omadusi. Füüsikaline karakteriseerimine kinnitas, et materjalid on peamiselt amorfsed, sisaldades väikeseid grafiitseid alasid. Aktiveerimisprotsesside käigus ei muutunud materjalide struktuur märkimisväärselt. Sorptsioonanalüüsi tulemused näitasid, et massikao suurenedes kasvab mesopoorsuse osakaal ning mõnevõrra vähenes mikropoorsus. Samuti suureneb kogu pooride ruumala ja keskmine pooride laius. Seega saab füüsikaliste karakteriseerimise tulemustest järeldada, et aktiveerimise käigus aset leidev massikadu toimub eelistatult süsinikmaterjalide amorfsetest osadest.

Aktiveeritud SiC-CDC materjalidel ja 1M $TEMABF_4$+AN elektrolüüdil põhinevad superkondensaatorid näitasid peaaegu ideaalset mahtuvuslikku käitumist ja suurepärast elektrilist efektiivsust 98–99%. Saavutatud mahtuvuse väärtused olid enam kui kaks korda suuremad võrreldes esialgse aktiveerimata SiC-CDC materjaliga. Samuti suurenesid energia- ja võimsustihedused üle 40%. $EMImBF_4$ elektrolüüdiga superkondensaatorite korral saavutasid veeauruga aktiveeritud materjalid mõnevõrra parema mahtuvusliku käitumise ning kõrgemad absoluutse faasinurga väärtused. See on tingitud nende poorsuse karakteristikutest – suurenenud mesopoorsus ning ka suurem laiemate mikropooride osakaal, võrreldes CO_2-ga aktiveeritud materjalidega. Esialgse SiC-CDC materjali mahtuvus ioonset vedelikku sisaldavas superkondensaatoris oli nulli lähedane.

Mõlema aktiveerimismeetodi puhul näitavad teostatud analüüsid, et materjalide makrostruktuur muutub ainult minimaalselt, kuid poorsuse karakteristikud (eripind, pooride koguruumala, pooride laius) muutuvad väga märkimisväärselt. Need muutused omakorda mõjutavad oluliselt SiC-CDC materjalide elektrokeemilisi omadusi. Seeläbi on lihtsa ja odava aktiveerimismeetodiga

(CO_2, veeaur või veeaur+CO_2) võimalik sünteesida SiC-CDC materjale, mis näitavad teiste karbiidest päritolu süsinikega võrreldavaid tulemusi, kuid samas on oluliselt odavamad materjalid. Veeauruga aktiveerimise protsess on mõnevõrra tõhusam, vähem aeganõudev ning saadavad materjalid näitavad erinevat tüüpi elektrolüütides väga head mahtuvuslikku käitumist. Seetõttu peaks veeauruga aktiveerimist eelistama CO_2-ga aktiveerimise meetodile.

ACKNOWLEDGEMENTS

I would like to express my greatest gratitude to my supervisors, Prof. Enn Lust, Ph.D Thomas Thomberg and Ph.D Indrek Tallo, who have supported and guided my work throughout the years. Also I am thankful to all my colleagues for the interesting discussions, useful advice, technical support and help with carrying out different measurements.

This research was supported by the Estonian Centre of Excellence in Science Project 3.2.0101.11-0030, by the EU through the European Regional Development Fund (TK141 „Advanced materials and high-technology devices for energy recuperation systems“), Estonian institutional research project IUT20–13, personal research grant PUT1107.

PUBLICATIONS

CURRICULUM VITAE

Name: Ester Tee
Date of birth: May 5, 1991
Citizenship: Estonian
Address: Institute of Chemistry, University of Tartu
Ravila 14a, 50411 Tartu, Estonia
Telephone: +372 5191 1525
E-mail: ester.tee@ut.ee

Education:

2015– …	University of Tartu, Institute of Chemistry, PhD student
2013–2015	University of Tartu – Master's degree in material science
2010–2013	University of Tartu – Bachelor's degree in material science
2007–2010	Pärnu Ühisgümnaasium – secondary education

Professional career:

2016– …	G.W.Berg OÜ, Sales manager for laboratory equipment
2012–2017	University of Tartu, Institute of Chemistry, Chemist

List of publications:

1. **E. Tee**, I. Tallo, T. Thomberg, A. Jänes, E. Lust, Electrical Double Layer Capacitor Characteristics Based on Steam and CO_2-Steam Co-Activated Carbon Electrodes and Ionic Liquid Electrolyte, J. Electrochem. Soc. 166 (8) (2019) A1558–A1567.
2. R. Härmas, R. Palm, M. Härmas, M. Pohl, H. Kurig, I. Tallo, **E. Tee**, I. Vaas, R. Väli, T. Romann, O. Oll, R. Kanarbik, K. Liivand, J. Eskusson, J. Kruusma, T. Thomberg, A. Jänes, P. Miidla, E. Lust, Influence of porosity parameters and electrolyte chemical composition on the power densities of non-aqueous and ionic liquid based supercapacitors, Electrochim. Acta 283 (2018) 931–948.
3. **E. Tee**, I. Tallo, T. Thomberg, A. Jänes, E. Lust, Steam and Carbon Dioxide Co-Activated Silicon Carbide-Derived Carbons for High Power Density Electrical Double Layer Capacitors, J. Electrochem. Soc. 165 (10) (2018) A2357–A2364.
4. S. Sepp, K. Vaarmets, J. Nerut, I. Tallo, **E. Tee**, H. Kurig, J. Aruväli, R. Kanarbik, E. Lust, Enhanced stability of symmetrical polymer electrolyte membrane fuel cell single cells based on novel hierarchical microporous-mesoporous carbon supports, J. Solid State Electrochem. 21 (4) (2017) 1035–1043.
5. S. Sepp, K. Vaarmets, J. Nerut, I. Tallo, **E. Tee**, H. Kurig, J. Aruväli, R. Kanarbik, E. Lust, Performance of Polymer Electrolyte Membrane Fuel Cell Single Cells Prepared Using Hierarchical Microporous-Mesoporous Carbon

Supported Pt Nanoparticles Activated Catalysts, Electrochem. Acta, 203 (2016) 221–229.

6. P. Valk, J. Nerut, I. Tallo, **E. Tee**, K. Vaarmets, T. Romann, H. Kurig, R. Palm, E. Lust, Structure and stability of partially chlorinated molybdenum carbide composite materials synthesised via high temperature chlorination, Electrochem. Acta, 191 (2016) 337–345.
7. **E. Tee**, I. Tallo, T. Thomberg, A. Jänes, E. Lust, Supercapacitors Based on Activated Silicon Carbide-Derived Carbon Materials and Ionic Liquid, J. Electrochem. Soc. 163 (7) (2016) A1317–A1325.
8. **E. Tee**, I. Tallo, H. Kurig, T. Thomberg, A. Jänes, E. Lust, Huge enhancement of energy storage capacity and power density of supercapacitors based on the carbon dioxide activated microporous SiC-CDC, Electrochimica Acta 161 (2015) 364–370.
9. A. Jänes, **E. Tee**, I. Tallo, T. Thomberg, E. Lust, Carbon Dioxide Activated SiC-CDC: Attractive Material for Supercapacitor Electrodes, ECS Trans. 69 (24) (2015) 1–10.

Industrial property:

E. Lust, K. Liivand, I. Vaas, T. Thomberg, I. Tallo, H. Kurig, T. Romann, R. Kanarbik, T. Tooming, **E. Tee**, A. Jänes, Separators, electrodes, half-cells and cells of electrical energy storage device, US 14/986,451, 2017.

Participation in International conferences:

1. **E. Tee**, I. Tallo, T. Thomberg, A. Jänes, E. Lust, Supercapacitors Based on Activated Silicon Carbide-Derived Carbon Materials and Different Electrolytes. 69th Annual Meeting of the International Society of Electrochemistry, Bologna, Italy, 2–7. August 2018 (poster presentation).
2. **E. Tee**, I. Tallo, T. Thomberg, A. Jänes, E. Lust, Activated Silicon Carbide-Derived Carbon Electrodes in Supercapacitors with Different Electrolytes. 7th Baltic Electrochemistry Conference, Tartu, Estonia, 4–7. November 2018 (poster presentation).

ELULOOKIRJELDUS

Nimi: Ester Tee
Sünniaeg: 5. mai 1991
Kodakondsus: Eesti
Aadress: Keemia instituut, Tartu Ülikool
Ravila 14a, Tartu 50411, Eesti
Telefon: +372 5191 1525
E-post: ester.tee@ut.ee

Haridus:

2015 –	Tartu Ülikooli keemia instituut, doktorant
2013–2015	Tartu Ülikool – magistrikraad materjaliteaduses
2010–2013	Tartu Ülikool – bakalaureusekraad materjaliteaduses
2007–2010	Pärnu Ühisgümnaasium

Teenistuskäik:

2016– …	G.W.Berg OÜ, Müügijuht (laboriseadmed)
2012–2017	Tartu Ülikooli keemia instituut, keemik

Publikatsioonid:

1. **E. Tee**, I. Tallo, T. Thomberg, A. Jänes, E. Lust, Electrical Double Layer Capacitor Characteristics Based on Steam and CO_2-Steam Co-Activated Carbon Electrodes and Ionic Liquid Electrolyte, J. Electrochem. Soc. 166 (8) (2019) A1558–A1567.
2. R. Härmas, R. Palm, M. Härmas, M. Pohl, H. Kurig, I. Tallo, **E. Tee**, I. Vaas, R. Väli, T. Romann, O. Oll, R. Kanarbik, K. Liivand, J. Eskusson, J. Kruusma, T. Thomberg, A. Jänes, P. Miidla, E. Lust, Influence of porosity parameters and electrolyte chemical composition on the power densities of non-aqueous and ionic liquid based supercapacitors, Electrochim. Acta 283 (2018) 931–948.
3. **E. Tee**, I. Tallo, T. Thomberg, A. Jänes, E. Lust, Steam and Carbon Dioxide Co-Activated Silicon Carbide-Derived Carbons for High Power Density Electrical Double Layer Capacitors, J. Electrochem. Soc. 165 (10) (2018) A2357–A2364.
4. S. Sepp, K. Vaarmets, J. Nerut, I. Tallo, **E. Tee**, H. Kurig, J. Aruväli, R. Kanarbik, E. Lust, Enhanced stability of symmetrical polymer electrolyte membrane fuel cell single cells based on novel hierarchical microporous-mesoporous carbon supports, J. Solid State Electrochem. 21 (4) (2017) 1035–1043.
5. S. Sepp, K. Vaarmets, J. Nerut, I. Tallo, **E. Tee**, H. Kurig, J. Aruväli, R. Kanarbik, E. Lust, Performance of Polymer Electrolyte Membrane Fuel Cell Single Cells Prepared Using Hierarchical Microporous-Mesoporous Carbon

Supported Pt Nanoparticles Activated Catalysts, Electrochem. Acta, 203 (2016) 221–229.

6. P. Valk, J. Nerut, I. Tallo, **E. Tee**, K. Vaarmets, T. Romann, H. Kurig, R. Palm, E. Lust, Structure and stability of partially chlorinated molybdenum carbide composite materials synthesised via high temperature chlorination, Electrochem. Acta, 191 (2016) 337–345.
7. **E. Tee**, I. Tallo, T. Thomberg, A. Jänes, E. Lust, Supercapacitors Based on Activated Silicon Carbide-Derived Carbon Materials and Ionic Liquid, J. Electrochem. Soc. 163 (7) (2016) A1317–A1325.
8. **E. Tee**, I. Tallo, H. Kurig, T. Thomberg, A. Jänes, E. Lust, Huge enhancement of energy storage capacity and power density of supercapacitors based on the carbon dioxide activated microporous SiC-CDC, Electrochimica Acta 161 (2015) 364–370.
9. A. Jänes, **E. Tee**, I. Tallo, T. Thomberg, E. Lust, Carbon Dioxide Activated SiC-CDC: Attractive Material for Supercapacitor Electrodes, ECS Trans. 69 (24) (2015) 1–10.

Tööstusomand:

E. Lust, K. Liivand, I. Vaas, T. Thomberg, I. Tallo, H. Kurig, T. Romann, R. Kanarbik, T. Tooming, **E. Tee**, A. Jänes, Separators, electrodes, half-cells and cells of electrical energy storage device, US 14/986,451, 2017.

Rahvusvahelistel konverentsidel osalemine:

1. **E. Tee**, I. Tallo, T. Thomberg, A. Jänes, E. Lust, Supercapacitors Based on Activated Silicon Carbide-Derived Carbon Materials and Different Electrolytes. 69th Annual Meeting of the International Society of Electrochemistry, Bologna, Italy, 2–7. August 2018 (poster ettekanne).
2. **E. Tee**, I. Tallo, T. Thomberg, A. Jänes, E. Lust, Activated Silicon Carbide-Derived Carbon Electrodes in Supercapacitors with Different Electrolytes. 7th Baltic Electrochemistry Conference, Tartu, Estonia, 4–7. November 2018 (poster ettekanne).

DISSERTATIONES CHIMICAE UNIVERSITATIS TARTUENSIS

1. **Toomas Tamm.** Quantum-chemical simulation of solvent effects. Tartu, 1993, 110 p.
2. **Peeter Burk.** Theoretical study of gas-phase acid-base equilibria. Tartu, 1994, 96 p.
3. **Victor Lobanov.** Quantitative structure-property relationships in large descriptor spaces. Tartu, 1995, 135 p.
4. **Vahur Mäemets.** The ^{17}O and ^{1}H nuclear magnetic resonance study of H_2O in individual solvents and its charged clusters in aqueous solutions of electrolytes. Tartu, 1997, 140 p.
5. **Andrus Metsala.** Microcanonical rate constant in nonequilibrium distribution of vibrational energy and in restricted intramolecular vibrational energy redistribution on the basis of slater's theory of unimolecular reactions. Tartu, 1997, 150 p.
6. **Uko Maran.** Quantum-mechanical study of potential energy surfaces in different environments. Tartu, 1997, 137 p.
7. **Alar Jänes.** Adsorption of organic compounds on antimony, bismuth and cadmium electrodes. Tartu, 1998, 219 p.
8. **Kaido Tammeveski.** Oxygen electroreduction on thin platinum films and the electrochemical detection of superoxide anion. Tartu, 1998, 139 p.
9. **Ivo Leito.** Studies of Brønsted acid-base equilibria in water and non-aqueous media. Tartu, 1998, 101 p.
10. **Jaan Leis.** Conformational dynamics and equilibria in amides. Tartu, 1998, 131 p.
11. **Toonika Rinken.** The modelling of amperometric biosensors based on oxidoreductases. Tartu, 2000, 108 p.
12. **Dmitri Panov.** Partially solvated Grignard reagents. Tartu, 2000, 64 p.
13. **Kaja Orupõld.** Treatment and analysis of phenolic wastewater with microorganisms. Tartu, 2000, 123 p.
14. **Jüri Ivask.** Ion Chromatographic determination of major anions and cations in polar ice core. Tartu, 2000, 85 p.
15. **Lauri Vares.** Stereoselective Synthesis of Tetrahydrofuran and Tetrahydropyran Derivatives by Use of Asymmetric Horner-Wadsworth-Emmons and Ring Closure Reactions. Tartu, 2000, 184 p.
16. **Martin Lepiku.** Kinetic aspects of dopamine D_2 receptor interactions with specific ligands. Tartu, 2000, 81 p.
17. **Katrin Sak.** Some aspects of ligand specificity of P2Y receptors. Tartu, 2000, 106 p.
18. **Vello Pällin.** The role of solvation in the formation of iotsitch complexes. Tartu, 2001, 95 p.
19. **Katrin Kollist.** Interactions between polycyclic aromatic compounds and humic substances. Tartu, 2001, 93 p.

20. **Ivar Koppel.** Quantum chemical study of acidity of strong and superstrong Brønsted acids. Tartu, 2001, 104 p.
21. **Viljar Pihl.** The study of the substituent and solvent effects on the acidity of OH and CH acids. Tartu, 2001, 132 p.
22. **Natalia Palm.** Specification of the minimum, sufficient and significant set of descriptors for general description of solvent effects. Tartu, 2001, 134 p.
23. **Sulev Sild.** QSPR/QSAR approaches for complex molecular systems. Tartu, 2001, 134 p.
24. **Ruslan Petrukhin.** Industrial applications of the quantitative structure-property relationships. Tartu, 2001, 162 p.
25. **Boris V. Rogovoy.** Synthesis of (benzotriazolyl)carboximidamides and their application in relations with *N*- and *S*-nucleophyles. Tartu, 2002, 84 p.
26. **Koit Herodes.** Solvent effects on UV-vis absorption spectra of some solvatochromic substances in binary solvent mixtures: the preferential solvation model. Tartu, 2002, 102 p.
27. **Anti Perkson.** Synthesis and characterisation of nanostructured carbon. Tartu, 2002, 152 p.
28. **Ivari Kaljurand.** Self-consistent acidity scales of neutral and cationic Brønsted acids in acetonitrile and tetrahydrofuran. Tartu, 2003, 108 p.
29. **Karmen Lust.** Adsorption of anions on bismuth single crystal electrodes. Tartu, 2003, 128 p.
30. **Mare Piirsalu.** Substituent, temperature and solvent effects on the alkaline hydrolysis of substituted phenyl and alkyl esters of benzoic acid. Tartu, 2003, 156 p.
31. **Meeri Sassian.** Reactions of partially solvated Grignard reagents. Tartu, 2003, 78 p.
32. **Tarmo Tamm.** Quantum chemical modelling of polypyrrole. Tartu, 2003. 100 p.
33. **Erik Teinemaa.** The environmental fate of the particulate matter and organic pollutants from an oil shale power plant. Tartu, 2003. 102 p.
34. **Jaana Tammiku-Taul.** Quantum chemical study of the properties of Grignard reagents. Tartu, 2003. 120 p.
35. **Andre Lomaka.** Biomedical applications of predictive computational chemistry. Tartu, 2003. 132 p.
36. **Kostyantyn Kirichenko.** Benzotriazole – Mediated Carbon–Carbon Bond Formation. Tartu, 2003. 132 p.
37. **Gunnar Nurk.** Adsorption kinetics of some organic compounds on bismuth single crystal electrodes. Tartu, 2003, 170 p.
38. **Mati Arulepp.** Electrochemical characteristics of porous carbon materials and electrical double layer capacitors. Tartu, 2003, 196 p.
39. **Dan Cornel Fara.** QSPR modeling of complexation and distribution of organic compounds. Tartu, 2004, 126 p.
40. **Riina Mahlapuu.** Signalling of galanin and amyloid precursor protein through adenylate cyclase. Tartu, 2004, 124 p.

41. **Mihkel Kerikmäe.** Some luminescent materials for dosimetric applications and physical research. Tartu, 2004, 143 p.
42. **Jaanus Kruusma.** Determination of some important trace metal ions in human blood. Tartu, 2004, 115 p.
43. **Urmas Johanson.** Investigations of the electrochemical properties of polypyrrole modified electrodes. Tartu, 2004, 91 p.
44. **Kaido Sillar.** Computational study of the acid sites in zeolite ZSM-5. Tartu, 2004, 80 p.
45. **Aldo Oras.** Kinetic aspects of dATPαS interaction with $P2Y_1$ receptor. Tartu, 2004, 75 p.
46. **Erik Mölder.** Measurement of the oxygen mass transfer through the air-water interface. Tartu, 2005, 73 p.
47. **Thomas Thomberg.** The kinetics of electroreduction of peroxodisulfate anion on cadmium (0001) single crystal electrode. Tartu, 2005, 95 p.
48. **Olavi Loog.** Aspects of condensations of carbonyl compounds and their imine analogues. Tartu, 2005, 83 p.
49. **Siim Salmar.** Effect of ultrasound on ester hydrolysis in aqueous ethanol. Tartu, 2006, 73 p.
50. **Ain Uustare.** Modulation of signal transduction of heptahelical receptors by other receptors and G proteins. Tartu, 2006, 121 p.
51. **Sergei Yurchenko.** Determination of some carcinogenic contaminants in food. Tartu, 2006, 143 p.
52. **Kaido Tämm.** QSPR modeling of some properties of organic compounds. Tartu, 2006, 67 p.
53. **Olga Tšubrik.** New methods in the synthesis of multisubstituted hydrazines. Tartu. 2006, 183 p.
54. **Lilli Sooväli.** Spectrophotometric measurements and their uncertainty in chemical analysis and dissociation constant measurements. Tartu, 2006, 125 p.
55. **Eve Koort.** Uncertainty estimation of potentiometrically measured ph and pK_a values. Tartu, 2006, 139 p.
56. **Sergei Kopanchuk.** Regulation of ligand binding to melanocortin receptor subtypes. Tartu, 2006, 119 p.
57. **Silvar Kallip.** Surface structure of some bismuth and antimony single crystal electrodes. Tartu, 2006, 107 p.
58. **Kristjan Saal.** Surface silanization and its application in biomolecule coupling. Tartu, 2006, 77 p.
59. **Tanel Tätte.** High viscosity $Sn(OBu)_4$ oligomeric concentrates and their applications in technology. Tartu, 2006, 91 p.
60. **Dimitar Atanasov Dobchev**. Robust QSAR methods for the prediction of properties from molecular structure. Tartu, 2006, 118 p.
61. **Hannes Hagu**. Impact of ultrasound on hydrophobic interactions in solutions. Tartu, 2007, 81 p.
62. **Rutha Jäger.** Electroreduction of peroxodisulfate anion on bismuth electrodes. Tartu, 2007, 142 p.

63. **Kaido Viht.** Immobilizable bisubstrate-analogue inhibitors of basophilic protein kinases: development and application in biosensors. Tartu, 2007, 88 p.
64. **Eva-Ingrid Rõõm.** Acid-base equilibria in nonpolar media. Tartu, 2007, 156 p.
65. **Sven Tamp.** DFT study of the cesium cation containing complexes relevant to the cesium cation binding by the humic acids. Tartu, 2007, 102 p.
66. **Jaak Nerut.** Electroreduction of hexacyanoferrate(III) anion on Cadmium (0001) single crystal electrode. Tartu, 2007, 180 p.
67. **Lauri Jalukse.** Measurement uncertainty estimation in amperometric dissolved oxygen concentration measurement. Tartu, 2007, 112 p.
68. **Aime Lust.** Charge state of dopants and ordered clusters formation in CaF_2:Mn and CaF_2:Eu luminophors. Tartu, 2007, 100 p.
69. **Iiris Kahn**. Quantitative Structure-Activity Relationships of environmentally relevant properties. Tartu, 2007, 98 p.
70. **Mari Reinik.** Nitrates, nitrites, N-nitrosamines and polycyclic aromatic hydrocarbons in food: analytical methods, occurrence and dietary intake. Tartu, 2007, 172 p.
71. **Heili Kasuk.** Thermodynamic parameters and adsorption kinetics of organic compounds forming the compact adsorption layer at Bi single crystal electrodes. Tartu, 2007, 212 p.
72. **Erki Enkvist.** Synthesis of adenosine-peptide conjugates for biological applications. Tartu, 2007, 114 p.
73. **Svetoslav Hristov Slavov**. Biomedical applications of the QSAR approach. Tartu, 2007, 146 p.
74. **Eneli Härk.** Electroreduction of complex cations on electrochemically polished Bi(*hkl*) single crystal electrodes. Tartu, 2008, 158 p.
75. **Priit Möller.** Electrochemical characteristics of some cathodes for medium temperature solid oxide fuel cells, synthesized by solid state reaction technique. Tartu, 2008, 90 p.
76. **Signe Viggor.** Impact of biochemical parameters of genetically different pseudomonads at the degradation of phenolic compounds. Tartu, 2008, 122 p.
77. **Ave Sarapuu.** Electrochemical reduction of oxygen on quinone-modified carbon electrodes and on thin films of platinum and gold. Tartu, 2008, 134 p.
78. **Agnes Kütt.** Studies of acid-base equilibria in non-aqueous media. Tartu, 2008, 198 p.
79. **Rouvim Kadis.** Evaluation of measurement uncertainty in analytical chemistry: related concepts and some points of misinterpretation. Tartu, 2008, 118 p.
80. **Valter Reedo.** Elaboration of IVB group metal oxide structures and their possible applications. Tartu, 2008, 98 p.
81. **Aleksei Kuznetsov.** Allosteric effects in reactions catalyzed by the cAMP-dependent protein kinase catalytic subunit. Tartu, 2009, 133 p.

82. **Aleksei Bredihhin.** Use of mono- and polyanions in the synthesis of multisubstituted hydrazine derivatives. Tartu, 2009, 105 p.
83. **Anu Ploom.** Quantitative structure-reactivity analysis in organosilicon chemistry. Tartu, 2009, 99 p.
84. **Argo Vonk.** Determination of adenosine A_{2A}- and dopamine D_1 receptor-specific modulation of adenylate cyclase activity in rat striatum. Tartu, 2009, 129 p.
85. **Indrek Kivi.** Synthesis and electrochemical characterization of porous cathode materials for intermediate temperature solid oxide fuel cells. Tartu, 2009, 177 p.
86. **Jaanus Eskusson.** Synthesis and characterisation of diamond-like carbon thin films prepared by pulsed laser deposition method. Tartu, 2009, 117 p.
87. **Marko Lätt.** Carbide derived microporous carbon and electrical double layer capacitors. Tartu, 2009, 107 p.
88. **Vladimir Stepanov.** Slow conformational changes in dopamine transporter interaction with its ligands. Tartu, 2009, 103 p.
89. **Aleksander Trummal.** Computational Study of Structural and Solvent Effects on Acidities of Some Brønsted Acids. Tartu, 2009, 103 p.
90. **Eerold Vellemäe.** Applications of mischmetal in organic synthesis. Tartu, 2009, 93 p.
91. **Sven Parkel.** Ligand binding to 5-HT_{1A} receptors and its regulation by Mg^{2+} and Mn^{2+}. Tartu, 2010, 99 p.
92. **Signe Vahur.** Expanding the possibilities of ATR-FT-IR spectroscopy in determination of inorganic pigments. Tartu, 2010, 184 p.
93. **Tavo Romann**. Preparation and surface modification of bismuth thin film, porous, and microelectrodes. Tartu, 2010, 155 p.
94. **Nadežda Aleksejeva.** Electrocatalytic reduction of oxygen on carbon nanotube-based nanocomposite materials. Tartu, 2010, 147 p.
95. **Marko Kullapere.** Electrochemical properties of glassy carbon, nickel and gold electrodes modified with aryl groups. Tartu, 2010, 233 p.
96. **Liis Siinor.** Adsorption kinetics of ions at Bi single crystal planes from aqueous electrolyte solutions and room-temperature ionic liquids. Tartu, 2010, 101 p.
97. **Angela Vaasa.** Development of fluorescence-based kinetic and binding assays for characterization of protein kinases and their inhibitors. Tartu 2010, 101 p.
98. **Indrek Tulp.** Multivariate analysis of chemical and biological properties. Tartu 2010, 105 p.
99. **Aare Selberg.** Evaluation of environmental quality in Northern Estonia by the analysis of leachate. Tartu 2010, 117 p.
100. **Darja Lavõgina.** Development of protein kinase inhibitors based on adenosine analogue-oligoarginine conjugates. Tartu 2010, 248 p.
101. **Laura Herm.** Biochemistry of dopamine D_2 receptors and its association with motivated behaviour. Tartu 2010, 156 p.

102. **Terje Raudsepp.** Influence of dopant anions on the electrochemical properties of polypyrrole films. Tartu 2010, 112 p.
103. **Margus Marandi.** Electroformation of Polypyrrole Films: *In-situ* AFM and STM Study. Tartu 2011, 116 p.
104. **Kairi Kivirand.** Diamine oxidase-based biosensors: construction and working principles. Tartu, 2011, 140 p.
105. **Anneli Kruve.** Matrix effects in liquid-chromatography electrospray mass-spectrometry. Tartu, 2011, 156 p.
106. **Gary Urb.** Assessment of environmental impact of oil shale fly ash from PF and CFB combustion. Tartu, 2011, 108 p.
107. **Nikita Oskolkov.** A novel strategy for peptide-mediated cellular delivery and induction of endosomal escape. Tartu, 2011, 106 p.
108. **Dana Martin.** The QSPR/QSAR approach for the prediction of properties of fullerene derivatives. Tartu, 2011, 98 p.
109. **Säde Viirlaid.** Novel glutathione analogues and their antioxidant activity. Tartu, 2011, 106 p.
110. **Ülis Sõukand.** Simultaneous adsorption of Cd^{2+}, Ni^{2+}, and Pb^{2+} on peat. Tartu, 2011, 124 p.
111. **Lauri Lipping.** The acidity of strong and superstrong Brønsted acids, an outreach for the "limits of growth": a quantum chemical study. Tartu, 2011, 124 p.
112. **Heisi Kurig.** Electrical double-layer capacitors based on ionic liquids as electrolytes. Tartu, 2011, 146 p.
113. **Marje Kasari.** Bisubstrate luminescent probes, optical sensors and affinity adsorbents for measurement of active protein kinases in biological samples. Tartu, 2012, 126 p.
114. **Kalev Takkis.** Virtual screening of chemical databases for bioactive molecules. Tartu, 2012, 122 p.
115. **Ksenija Kisseljova**. Synthesis of aza-β^3-amino acid containing peptides and kinetic study of their phosphorylation by protein kinase A. Tartu, 2012, 104 p.
116. **Riin Rebane.** Advanced method development strategy for derivatization LC/ESI/MS. Tartu, 2012, 184 p.
117. **Vladislav Ivaništšev.** Double layer structure and adsorption kinetics of ions at metal electrodes in room temperature ionic liquids. Tartu, 2012, 128 p.
118. **Irja Helm.** High accuracy gravimetric Winkler method for determination of dissolved oxygen. Tartu, 2012, 139 p.
119. **Karin Kipper.** Fluoroalcohols as Components of LC-ESI-MS Eluents: Usage and Applications. Tartu, 2012, 164 p.
120. **Arno Ratas.** Energy storage and transfer in dosimetric luminescent materials. Tartu, 2012, 163 p.
121. **Reet Reinart-Okugbeni**. Assay systems for characterisation of subtype-selective binding and functional activity of ligands on dopamine receptors. Tartu, 2012, 159 p.

122. **Lauri Sikk.** Computational study of the Sonogashira cross-coupling reaction. Tartu, 2012, 81 p.
123. **Karita Raudkivi.** Neurochemical studies on inter-individual differences in affect-related behaviour of the laboratory rat. Tartu, 2012, 161 p.
124. **Indrek Saar.** Design of GalR2 subtype specific ligands: their role in depression-like behavior and feeding regulation. Tartu, 2013, 126 p.
125. **Ann Laheäär.** Electrochemical characterization of alkali metal salt based non-aqueous electrolytes for supercapacitors. Tartu, 2013, 127 p.
126. **Kerli Tõnurist.** Influence of electrospun separator materials properties on electrochemical performance of electrical double-layer capacitors. Tartu, 2013, 147 p.
127. **Kaija Põhako-Esko.** Novel organic and inorganic ionogels: preparation and characterization. Tartu, 2013, 124 p.
128. **Ivar Kruusenberg.** Electroreduction of oxygen on carbon nanomaterial-based catalysts. Tartu, 2013, 191 p.
129. **Sander Piiskop.** Kinetic effects of ultrasound in aqueous acetonitrile solutions. Tartu, 2013, 95 p.
130. **Ilona Faustova**. Regulatory role of L-type pyruvate kinase N-terminal domain. Tartu, 2013, 109 p.
131. **Kadi Tamm.** Synthesis and characterization of the micro-mesoporous anode materials and testing of the medium temperature solid oxide fuel cell single cells. Tartu, 2013, 138 p.
132. **Iva Bozhidarova Stoyanova-Slavova.** Validation of QSAR/QSPR for regulatory purposes. Tartu, 2013, 109 p.
133. **Vitali Grozovski**. Adsorption of organic molecules at single crystal electrodes studied by *in situ* STM method. Tartu, 2014, 146 p.
134. **Santa Veikšina**. Development of assay systems for characterisation of ligand binding properties to melanocortin 4 receptors. Tartu, 2014, 151 p.
135. **Jüri Liiv.** PVDF (polyvinylidene difluoride) as material for active element of twisting-ball displays. Tartu, 2014, 111 p.
136. **Kersti Vaarmets.** Electrochemical and physical characterization of pristine and activated molybdenum carbide-derived carbon electrodes for the oxygen electroreduction reaction. Tartu, 2014, 131 p.
137. **Lauri Tõntson**. Regulation of G-protein subtypes by receptors, guanine nucleotides and Mn^{2+}. Tartu, 2014, 105 p.
138. **Aiko Adamson.** Properties of amine-boranes and phosphorus analogues in the gas phase. Tartu, 2014, 78 p.
139. **Elo Kibena**. Electrochemical grafting of glassy carbon, gold, highly oriented pyrolytic graphite and chemical vapour deposition-grown graphene electrodes by diazonium reduction method. Tartu, 2014, 184 p.
140. **Teemu Näykki.** Novel Tools for Water Quality Monitoring – From Field to Laboratory. Tartu, 2014, 202 p.
141. **Karl Kaupmees.** Acidity and basicity in non-aqueous media: importance of solvent properties and purity. Tartu, 2014, 128 p.

142. **Oleg Lebedev**. Hydrazine polyanions: different strategies in the synthesis of heterocycles. Tartu, 2015, 118 p.
143. **Geven Piir.** Environmental risk assessment of chemicals using QSAR methods. Tartu, 2015, 123 p.
144. **Olga Mazina.** Development and application of the biosensor assay for measurements of cyclic adenosine monophosphate in studies of G protein-coupled receptor signalinga. Tartu, 2015, 116 p.
145. **Sandip Ashokrao Kadam.** Anion receptors: synthesis and accurate binding measurements. Tartu, 2015, 116 p.
146. **Indrek Tallo.** Synthesis and characterization of new micro-mesoporous carbide derived carbon materials for high energy and power density electrical double layer capacitors. Tartu, 2015, 148 p.
147. **Heiki Erikson.** Electrochemical reduction of oxygen on nanostructured palladium and gold catalysts. Tartu, 2015, 204 p.
148. **Erik Anderson.** *In situ* Scanning Tunnelling Microscopy studies of the interfacial structure between Bi(111) electrode and a room temperature ionic liquid. Tartu, 2015, 118 p.
149. **Girinath G. Pillai.** Computational Modelling of Diverse Chemical, Biochemical and Biomedical Properties. Tartu, 2015, 140 p.
150. **Piret Pikma.** Interfacial structure and adsorption of organic compounds at Cd(0001) and Sb(111) electrodes from ionic liquid and aqueous electrolytes: an *in situ* STM study. Tartu, 2015, 126 p.
151. **Ganesh babu Manoharan.** Combining chemical and genetic approaches for photoluminescence assays of protein kinases. Tartu, 2016, 126 p.
152. **Carolin Siimenson**. Electrochemical characterization of halide ion adsorption from liquid mixtures at Bi(111) and pyrolytic graphite electrode surface. Tartu, 2016, 110 p.
153. **Asko Laaniste.** Comparison and optimisation of novel mass spectrometry ionisation sources. Tartu, 2016, 156 p.
154. **Hanno Evard.** Estimating limit of detection for mass spectrometric analysis methods. Tartu, 2016, 224 p.
155. **Kadri Ligi.** Characterization and application of protein kinase-responsive organic probes with triplet-singlet energy transfer. Tartu, 2016, 122 p.
156. **Margarita Kagan.** Biosensing penicillins' residues in milk flows. Tartu, 2016, 130 p.
157. **Marie Kriisa.** Development of protein kinase-responsive photoluminescent probes and cellular regulators of protein phosphorylation. Tartu, 2016, 106 p.
158. **Mihkel Vestli.** Ultrasonic spray pyrolysis deposited electrolyte layers for intermediate temperature solid oxide fuel cells. Tartu, 2016, 156 p.
159. **Silver Sepp**. Influence of porosity of the carbide-derived carbon on the properties of the composite electrocatalysts and characteristics of polymer electrolyte fuel cells. Tartu, 2016, 137 p.
160. **Kristjan Haav**. Quantitative relative equilibrium constant measurements in supramolecular chemistry. Tartu, 2017, 158 p.

161. **Anu Teearu**. Development of MALDI-FT-ICR-MS methodology for the analysis of resinous materials. Tartu, 2017, 205 p.
162. **Taavi Ivan**. Bifunctional inhibitors and photoluminescent probes for studies on protein complexes. Tartu, 2017, 140 p.
163. **Maarja-Liisa Oldekop**. Characterization of amino acid derivatization reagents for LC-MS analysis. Tartu, 2017, 147 p.
164. **Kristel Jukk**. Electrochemical reduction of oxygen on platinum- and palladium-based nanocatalysts. Tartu, 2017, 250 p.
165. **Siim Kukk**. Kinetic aspects of interaction between dopamine transporter and *N*-substituted nortropane derivatives. Tartu, 2017, 107 p.
166. **Birgit Viira**. Design and modelling in early drug development in targeting HIV-1 reverse transcriptase and Malaria. Tartu, 2017, 172 p.
167. **Rait Kivi**. Allostery in cAMP dependent protein kinase catalytic subunit. Tartu, 2017, 115 p.
168. **Agnes Heering**. Experimental realization and applications of the unified acidity scale. Tartu, 2017, 123 p.
169. **Delia Juronen**. Biosensing system for the rapid multiplex detection of mastitis-causing pathogens in milk. Tartu, 2018, 85 p.
170. **Hedi Rahnel.** ARC-inhibitors: from reliable biochemical assays to regulators of physiology of cells. Tartu, 2018, 176 p.
171. **Anton Ruzanov.** Computational investigation of the electrical double layer at metal–aqueous solution and metal–ionic liquid interfaces. Tartu, 2018, 129 p.
172. **Katrin Kestav.** Crystal Structure-Guided Development of Bisubstrate-Analogue Inhibitors of Mitotic Protein Kinase Haspin. Tartu, 2018, 166 p.
173. **Mihkel Ilisson.** Synthesis of novel heterocyclic hydrazine derivatives and their conjugates. Tartu, 2018, 101 p.
174. **Anni Allikalt.** Development of assay systems for studying ligand binding to dopamine receptors. Tartu, 2018, 160 p.
175. **Ove Oll.** Electrical double layer structure and energy storage characteristics of ionic liquid based capacitors. Tartu, 2018, 187 p.
176. **Rasmus Palm.** Carbon materials for energy storage applications. Tartu, 2018, 114 p.
177. **Jörgen Metsik.** Preparation and stability of poly(3,4-ethylenedioxythiophene) thin films for transparent electrode applications. Tartu, 2018, 111 p.
178. **Sofja Tšepelevitš.** Experimental studies and modeling of solute-solvent interactions. Tartu, 2018, 109 p.
179. **Märt Lõkov.** Basicity of some nitrogen, phosphorus and carbon bases in acetonitrile. Tartu, 2018, 104 p.
180. **Anton Mastitski**. Preparation of α-aza-amino acid precursors and related compounds by novel methods of reductive one-pot alkylation and direct alkylation. Tartu, 2018, 155 p.
181. **Jürgen Vahter**. Development of bisubstrate inhibitors for protein kinase CK2. Tartu, 2019, 186 p.

182. **Piia Liigand.** Expanding and improving methodology and applications of ionization efficiency measurements. Tartu, 2019, 189 p.
183. **Sigrid Selberg.** Synthesis and properties of lipophilic phosphazene-based indicator molecules. Tartu, 2019, 74 p.
184. **Jaanus Liigand.** Standard substance free quantification for LC/ESI/MS analysis based on the predicted ionization efficiencies. Tartu, 2019, 254 p.
185. **Marek Mooste.** Surface and electrochemical characterisation of aryl film and nanocomposite material modified carbon and metal-based electrodes. Tartu, 2019, 304 p.
186. **Mare Oja.** Experimental investigation and modelling of pH profiles for effective membrane permeability of drug substances. Tartu, 2019, 306 p.
187. **Sajid Hussain.** Electrochemical reduction of oxygen on supported Pt catalysts. Tartu, 2019, 220 p.
188. **Ronald Väli.** Glucose-derived hard carbon electrode materials for sodium-ion batteries. Tartu, 2019, 180 p.